1-1-2007

A numerical study on liquid water behaviours in PEM fuel cell cathode.

Kui Jiao
University of Windsor

A Numerical Study on Liquid Water Behaviours in PEM Fuel Cell Cathode

by

Kui Jiao

A Thesis
Submitted to the Faculty of Graduate Studies
through Mechanical Engineering
in Partial Fulfillment of the Requirements for
the Degree of Master of Applied Science at the
University of Windsor

Windsor, Ontario, Canada

2007

Your file Votre référence
ISBN: 978-0-494-35052-2
Our file Notre référence
ISBN: 978-0-494-35052-2

ABSTRACT

A numerical study investigating different air-water flows in both fuel cell stacks and Gas Diffusion Layers (GDL) in Proton Exchange Membrane (PEM) fuel cell cathode was performed by use of the commercial Computational Fluid Dynamics (CFD) software package FLUENT. Both the parallel-serpentine and parallel-straight PEM fuel cell stacks were studied, different designs of micro-structures of the GDL were also studied to indicate the best GDL, then the best GDL is studied with different wettabilities to test the effects of the material properties on liquid water transport. Different air-water flow behaviours were investigated and described. Some water management problems related to PEM fuel cells were identified and recommendations were given through investigating the flow patterns.

DEDICATION

To my Father and Mother.

ACKNOWLEDGEMENTS

I would like to thank my supervisor, Dr. Biao Zhou, for his great ideas, guidance, encouragement and allowing me the opportunity to work with one of the finest professors I have ever come to know. Sincere thanks to Dr. Andrzej Sobiesiak, Dr. Jonathan Wu and Dr. Nader Zamani for their time and assistance in the development of this thesis.

Additional thanks to Peng Quan, Jixin Chen and Haibo Yu for their contributions and assistance.

I am also grateful for the support of this work by the Auto21^{TM} Networks of Centres of Excellence (Grant D07-DFC), the Natural Sciences and Engineering Research Council of Canada (NSERC), the Canada Foundation for Innovation (CFI), the Ontario Innovation Trust (OIT), and the Graduate School at the University of Windsor.

Finally, special thanks to my parents Xuejun Jiao and Aimei Yang, my girl friend Man Li. Thank you for putting up with my difficult times and for supporting me while I complete one of my dreams.

TABLE OF CONTENTS

LIST OF TABLES

LIST OF FIGURES

CHAPTER 1

INTRODUCTION

1.1 Fuel cell technology

A fuel cell is an energy conversion device that converts the chemical energy stored in fuels into electricity through electrochemical reactions [1]. Fuel cells have been recognized as an ideal power source for a variety of applications such as automotives and substitute batteries due to their significant advantages, i.e. high efficiency, low emission, silence and simplicity. It is widely accepted that fuel cells will finally replace the traditional internal combustion engines to be used in vehicular applications. Over past decades fuel cell technology has achieved significant improvements in terms of performance, durability, stability and cost. However, it is still not a mature technology mainly because fuel cell itself must achieve higher power density, higher durability and lower cost before successful commercialization.

1.2 Proton Exchange Membrane (PEM) fuel cell

Low operating temperature, high power density and zero/low emission have made Proton Exchange Membrane (PEM) fuel cells become the most promising fuel cell type for the future in vehicle and portable applications [2]. PEM fuel cell is also the most popular one under research and development compared with other types of fuel cell, i.e., Alkaline Fuel Cell (AFC), Phosphoric Acid Fuel Cell (PAFC), Molten Carbonate Fuel Cell (MCFC) and Solid Oxide Fuel Cell (SOFC). PEM fuel cell appears to offer the best prospect for further improvement until the successful commercialization, which may become true within two decades.

1.3 Effects of liquid water on PEM fuel cell

Even PEM fuel cell is recognized as the most promising power source for the future in vehicle and portable applications. However, to achieve commercialization, the performance of PEM fuel cells needs to be improved by proper engineering design and optimization. Due to the complex electrochemistry, PEM fuel cell itself is an unsteady system, which is very sensitive to several operating parameters such as water management, reactants supply, system pressure and stack temperature. The output of fuel cell may vary significantly even one of those parameters changes, and water management is one the most important issues that affects on PEM fuel cell performance.

Due to the special chemical structure of the PEM, the membrane must be well hydrated to ensure that a sufficient amount of hydrogen ions could cross. On the other hand, due to the low operating temperature of PEM fuel cells (30 to 100°C) [2], excessive humidification could result in water vapour condensation that could subsequently block the reaction sites resulting in a lower air flow rate on the cathode side, thus decreasing fuel cell performance. Water content is also an important factor that affects the ohmic resistance in the membrane [3]. Therefore, keeping an appropriate amount of water content in the fuel cell to avoid both membrane dehydration and water vapour condensation has been a critical issue in improving fuel cell performance. In reality, however, it is almost impossible to manage water on both the anode and cathode sides without dehydration and condensation, this is simply because water vapour condensation in practical fuel cell applications is unavoidable [3]. Therefore, water management, to

which many engineers and scientists have recently paid particular attention, has been a critical challenge for a high-performance fuel cell design and optimization.

1.4 Research summary

This project will focus on different numerical investigations of air-water flow in both fuel cell stacks and Gas Diffusion Layers (GDL) in PEM fuel cell cathode by use of the commercial Computational Fluid Dynamics (CFD) software package FLUENT. Both parallel-serpentine and parallel-straight PEM fuel cell stacks are studied, different designs of micro-structures of GDL are also studied to indicate the best micro-structure of the GDL, then the best GDL is studied with different wettabilities to test the effects of the material properties on liquid water transport. Different air-water flow behaviours will be discussed. Gas flow problems will be identified and recommendations will be given through investigating the flow patterns.

CHAPTER 2

REVIEW OF LITERATURE

2.1 PEM fuel cell fundamentals

PEM fuel cell is an electrochemical energy conversion device that produces electrical energy by utilizing the chemical energy stored fuels (on the anode side) and oxidants (on the cathode side) from external supplies. Reactions at both sides are as follows:

Anode: $H_2 \rightarrow 2H^+ + 2e^-$ (1)

Cathode: $1/2O_2 + H_2 + 2e^- \rightarrow H_2O$ (2)

As shown in Fig. 1, typically a PEM fuel cell consists of both anode and cathode, and a membrane in between. At the anode, hydrogen flows into the gas flow channels, flows through the GDL onto the catalyst layer. On the catalyst layer of the anode, hydrogen splits into protons (hydrogen ions) and electrons, the protons pass through the membrane and travel into the cathode. The electrons cannot pass through the membrane, but travel through an external circuit to the cathode, thus generating electricity. At the same time, at the cathode, air or oxygen flows into the gas flow channels, flows through the GDL onto the catalyst layer. On the catalyst layer of the cathode, oxygen reacts with the protons (hydrogen ions) and electrons from the anode, producing water and heat. Due to pressure, water concentration difference between the anode and cathode, and the proton transport across the membrane, water can travel through the membrane in both directions.

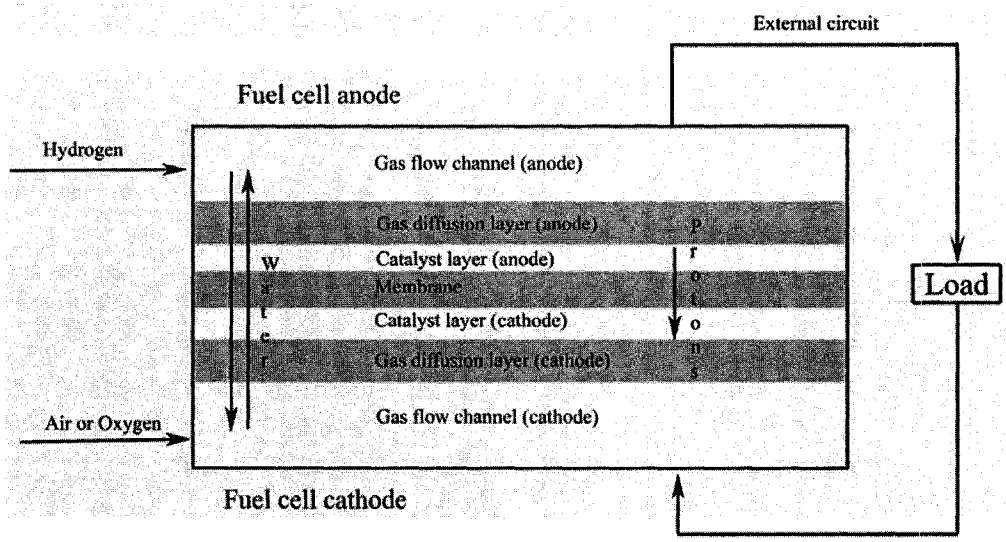

Fig. 1. Schematic of PEM fuel cell operation.

On both sides of the membrane, the catalyst layers form in terms of carbon supported platinum as the catalyst. PEM fuel cell usually works at less than 100 ^{0}C and normal pressure, which means presence of catalyst, is significant to facilitate the electrochemical reaction. Platinum is the best catalyst for both anode and cathode, although some substitutes such as Pt alloyed compound are currently under active research.

As the physical support of the membrane and catalyst layer, GDL is attached to the outside of the catalyst layer and the whole structure (membrane, catalyst layer and GDL) is compressed to form the Membrane Electrode Assembly (MEA). Carbon paper or carbon cloth is widely used as the GDL because of its high porosity that facilitates the reactant transportation towards the catalyst sites. Also the very low electrical resistance of carbon paper/cloth makes the ohmic loss within an acceptable range.

The Open Circuit Voltage (OCV) of a single cell is very small with a theoretical value of 1.18 V, it should be noted that this is the reversible open circuit voltage that does not taken into account any loss or irreversibility. The operating voltage is even smaller, about 0.7 V when drawing a useful current. Therefore, many cells have to be connected in series to form a fuel cell stack to produce a useful voltage, as Fig. 2 shows the structure of a PEM fuel cell stack. To this end, "bipolar plate" is made, as it is the interconnection between the anode of one cell and the cathode of the neighbouring cell. There are channels cut in both sides of the bipolar plate so that the reactant gas can flow over the face of electrode. In the meantime, it makes a good electrical contact with the surface of electrode, which is achieved by 1) the material has very low electrical resistant; 2) the whole stack is compressed evenly during assembling. The material for bipolar plate is usually stainless steel or graphite.

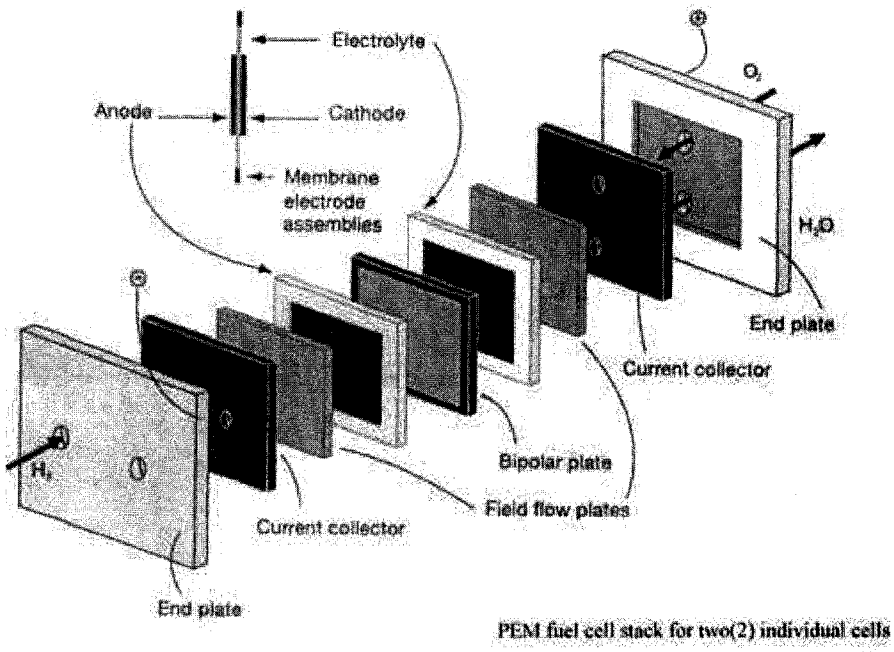

Fig. 2. PEM fuel cell structure [4].

2.2 PEM fuel cell performance

Fig. 3 shows a typical current-voltage (I-V) graph of a PEM fuel cell, the performance can be usually summarized in this figure. This figure shows the voltage output of the fuel cell at a given current output. The current has been normalized by the area of the fuel cell in terms of a standard unit of current density (in amperes per square centimetre). Larger fuel cells can obviously produce more electricity than smaller ones; therefore a normalized current unit makes fuel cell performance comparable.

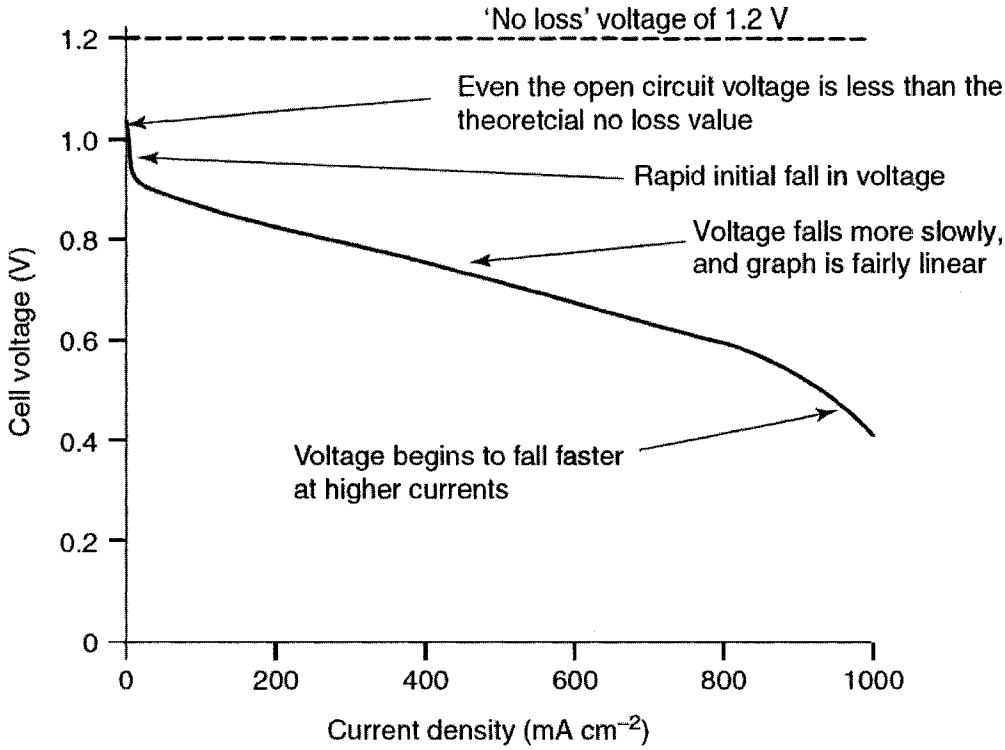

Fig. 3. Typical performance curve of PEM fuel cell [2].

Theoretically, a fuel cell would supply any amount of current under the condition of sufficient fuel supply, while maintaining a constant voltage determined by thermodynamics. In practice, however, the actual voltage output of a fuel cell is less than the ideal thermodynamically predicted value. Furthermore, the more current that is drawn from a real fuel cell, the lower the voltage output of the cell, limiting the total power that can be delivered.

It is difficult to maintain the cell voltage at a high level under current load, as shown in Fig. 3. The voltage output of a fuel cell in operation is less than thermodynamically

predicted value due to irreversible losses. Total loss increases with the increasing current drawn from the stack. There are four major types of fuel cell losses:

1) Activation loss. Such loss is caused by the slowness of the reactions taking place on the surface of the electrodes. A proportion of the voltage generated is lost in driving the chemical reaction that transfers the electrons to or from the electrode. Electron does not participate the reaction as soon as it releases, enough amount of electrons accumulate to such a level that the reaction can take place continuously given the sufficient gas supplies. This level can be imagined, or is equivalent to, the activation loss. In Fig. 3, it is represented by the initial sharp drop of the cell voltage.

2) Ohmic loss. It is the straightforward resistance to the flow of electrons through the material of the electrodes and the various interconnections, as well as the resistance to the flow of ions through the electrolyte. This voltage drop is essentially proportional to current density, represented by the linear fall in the middle of the performance curve in Fig. 3.

3) Mass transport or concentration loss. Such loss results from the change in concentration of the reactants at the surface of the electrodes as they are consumed along the gas channel from the inlet to the outlet. Concentration affects voltage via the change of differential pressure of reactant. That is why this type of irreversibility is called concentration loss. On the other hand, since the reduction in concentration is the result of a failure to transport sufficient reactant to the electrode surface or catalyst sites, this type

of irreversibility is also called mass transport loss. In Fig. 3, such loss can be observed at high current density range as an unlinear drop, because sufficient reactant supply is the controlling factor to obtain large amount of current.

4) Fuel crossover and internal currents. Such loss results from the waste of fuel passing through the electrolyte, and, to a lesser extent, from electron conduction through the electrolyte. The electrolyte should only transport ions through the electrodes, however very small amount of fuel diffusion and electron flow will always be possible. It does have a marked influence on the OCV of low-temperature fuel cell, which explains why the OCV is always smaller than the theoretical no loss value.

Combining all the irreversibilities, the operating voltage of a fuel cell at a current density i can be modeled by the following equation [2]:

$$V = E - \Delta V_{ohm} - \Delta V_{act} - \Delta V_{trans} \quad (3)$$

2.3 Modelling and experimental studies

In the last decade, water management related studies were performed numerically and experimentally for different purposes and in several ways. A CFD modeling of PEM fuel cells which simultaneously considered the electrochemical kinetics, current distributions, hydrodynamics, and multi-component transport was conducted by S. Um *et al.* [5]. A three-dimensional (3-D) numerical simulation of a straight gas flow channel in a PEM fuel cell was performed by Dutta *et al.* [6] using a commercial CFD software FLUENT.

Hontanon *et al.* [7] also employed FLUENT to implement their 3-D, stationary gas flow model. A study exploring the steady-state gas transport phenomena in micro-scale parallel flow channels was conducted by Cha *et al.* [8] in which oxygen concentration along a single gas flow channel and other flow patterns that may affect fuel cell performance were discussed. Similarly, gas concentration of a steady-state flow along fuel cell flow channels was obtained numerically by Kulikovsky [9]. However, in all the studies mentioned above, the effects of liquid water were neglected. Yi *et al.* [3] pointed out that water vapour condensation was inevitable on both the anode and cathode sides of a PEM fuel cell, and they discussed a liquid water removal technique that used a water transport plate to lead excess liquid water to the coolant flow channels by a pressure difference. Wang *el al.* [10] conducted a two-phase model on PEM fuel cell cathode to address the liquid water concentrations. You and Liu [11] also considered liquid water concentration in a straight channel on the cathode side. Both the references [10, 11] showed the importance for considering liquid water in numerical modeling of PEM fuel cells. In recent years, more two phase models have been published [12-14], these simulations predicted water flooding inside PEM fuel cells, and the liquid water effects on PEM fuel cell performances. Large-scale simulations for complex flow field were also performed with experimental validations [15-18], these simulations provided more realistic results rather than considering one single cell. A comprehensive review of water management in fuel cells was also made by Wang [19] to address this important issue.

On the cathode side of fuel cells, most of the water, which is mainly produced by the electrochemical reaction, flows through the GDL to the gas flow channels. Therefore,

liquid water flow across the GDL to the gas flow channels, and formation of water droplets during this process are both unavoidable and important for practical operations of PEM fuel cells. As the authors reviewed, experimental studies to probe detailed liquid water transport from the GDL into the gas flow channels have been performed by Yang el al. [20] and Zhang et al. [21]. In these studies, the observations of liquid water distributions on the GDL surfaces were made in a transparent PEM fuel cell, and liquid water droplet formation and emerging of liquid water were discussed. Numerical models that considered the GDL were developed in several ways. Nam and Kaviany [22] developed a two dimensional, two-phase numerical model by considering random carbon fibre mats as the GDL. Single- and two- layer diffusion media were both considered to investigate the effective diffusivity and water saturation. A study on the interaction between the GDL and the flow field was performed by Dohle *et al.* [23] numerically and experimentally. Other models that considered the porous media also mainly focused on the porosity of the carbon fibre paper that could influence the performances of PEM fuel cells [24, 25]. However, the detailed flow patterns that liquid water exhibits across the porous media and the effects of the micro-structures of GDL were rarely discussed.

By far, to the author's knowledge, most of the two phase numerical models have not considered the interface tracking between liquid water and gas. The detailed behaviours of liquid water transport inside the PEM fuel cells were rarely discussed except for Quan *et al.* [26], which only dealt with part of serpentine channels - the single U-shaped channel. In this project, both the parallel-serpentine and parallel-straight PEM fuel cell stack cathodes consisting of several unit cells with inlet and outlet manifolds were

proposed to investigate the details of fluid flows and predict the distribution of liquid water among different cells [27, 28]. The pressure drop along different parts of the stack cathode was also presented graphically as it is significantly affected by the liquid water transport.

In addition, some very important facts have often not been paid serious attention: the conventional GDLs are not effective for water removal. This is because the micro-structure and the size of the pores of conventional GDLs are very arbitrary, and the sizes of the pores are very small (10 and 30 micrometers). Due to the physical features that the conventional GDLs, it is very frequent for liquid water to flood the GDL and catalyst layer in practical PEM fuel cells. The main reason causing frequent flooding is that the arbitrary structure of conventional GDLs does not allow a well-organized liquid water flow. Therefore, in this project, different kinds of innovative GDLs, with well-designed micro-flow-channels were also proposed to solve these problems. To investigate the details of the water removal characteristics of the proposed innovative GDLs and to predict the distribution of liquid water, a unit serpentine gas flow channel with three different kinds of micro-structures of innovative GDLs were studied [29]. Different flow patterns in different micro-structures were presented graphically. After the best micro-structure of the GDL is selected, the wettability of the best GDL was studied; different static contact angles (hydrophobic, hydrophilic) were assigned to the electrode (GDL and catalyst layer) to find the effects of the material properties of the electrode on liquid water transport.

Generally, this project consists of four major topics: 1. liquid water transport in parallel-serpentine PEM fuel cell stack cathode, 2. liquid water transport in parallel-straight PEM fuel cell stack cathode, 3. effects of innovative micro-structures of GDL on liquid water transport, 4. Effects of wettabilities of the electrode on liquid water transport. Most of the results in this project are already published [27-29]. In addition, the details of phase change and electro-chemical reaction were not considered in all the simulations. Based on the author's understanding, the effect of the electro-chemical reaction inside PEM fuel cell on liquid water behaviour is mainly to continuously supply water. Based on this premise, various operating conditions for a PEM fuel cell could be simulated without involving details of electro-chemical reactions. In this project, therefore, different initial liquid water distributions were employed to simplify the complex process of real PEM fuel cell operating condition.

CHAPTER 3

NUMERICAL MODEL SETUP

3,1 Computation domains and boundary conditions

Fig. 4 illustrates a schematic of the computation domain for Topic 1 showing the cathode side of the three-cell parallel-serpentine PEM fuel cell stack considered with the inlet and outlet flow manifolds at the top and bottom, respectively. Both manifolds were 12 mm long and had a cross section of 2 $\times$ 2 mm with three serpentine unit cells connected between them. Each unit cell had two symmetric serpentine gas flow channels with a cross section of 1 $\times$ 1 mm and the straight section of the gas flow channels was 10 mm long. A Velocity Inlet boundary condition (uniform air velocity distribution of 10 m/s with a direction normal to the inlet boundary) was applied at the air inlet of the inlet flow manifold. At the outlet, the boundary condition was assigned as Outlet Flow (the gradients of all flow properties are zero). Gravity was taken as being along the negative y-direction. The three single cells were numbered as Cell 1, Cell 2 and Cell 3, please refer to Fig. 4.

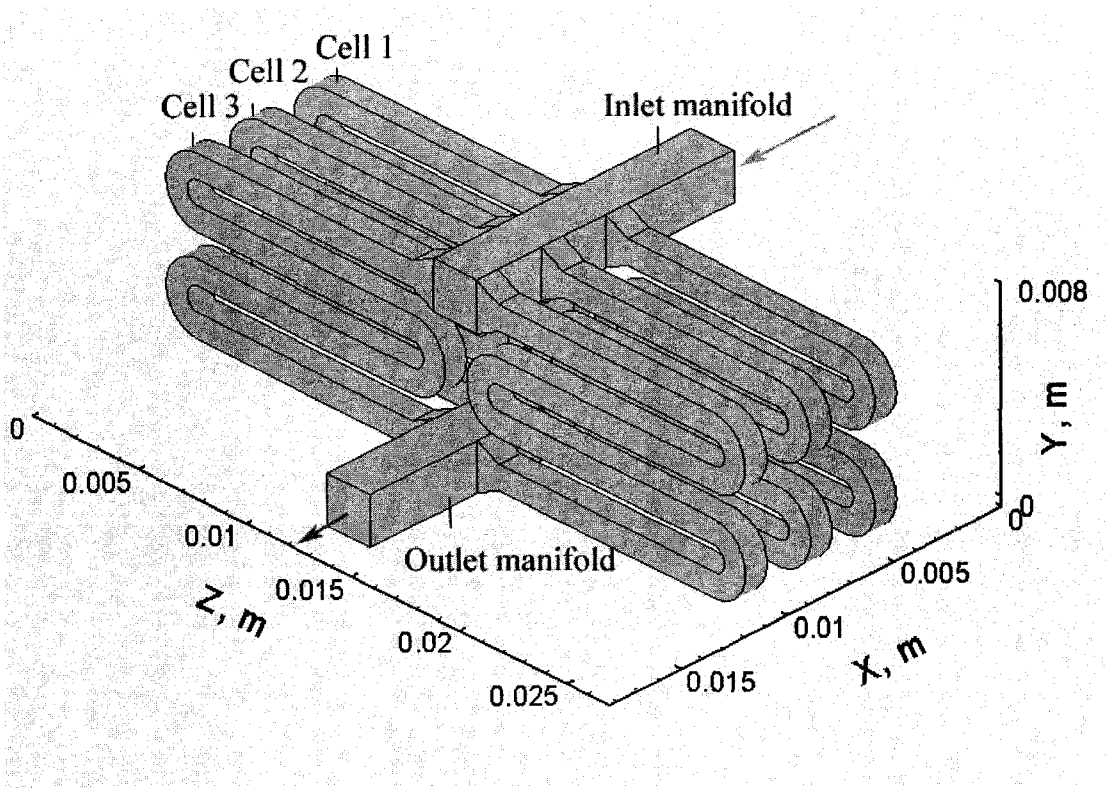

Fig. 4. Computation domain for parallel-serpentine PEM fuel cell stack cathode (Topic 1).

Fig. 5 illustrates a schematic of the computation domain for Topic 2 showing the cathode side of the five-cell PEM fuel cell stack considered with the inlet and outlet flow manifolds at the top and bottom, respectively. The direction of the outlet manifold was placed which is opposed from normal arrangements, this is because the author wants to find the problems that could happen in such arrangement. Both manifolds were 20 mm long and had a cross section of 5 × 5 mm with five unit cells connected between them. Each unit cell had three straight parallel gas flow channels 10 mm in height and a cross section of 1 × 1 mm. A Velocity Inlet boundary condition (uniform air velocity distribution of 5 m/s with a direction normal to the inlet boundary) was applied at the air

inlet of the inlet flow manifold. At the outlet, the boundary condition was assigned as Outlet Flow. Gravity was taken as being along the negative y-direction.

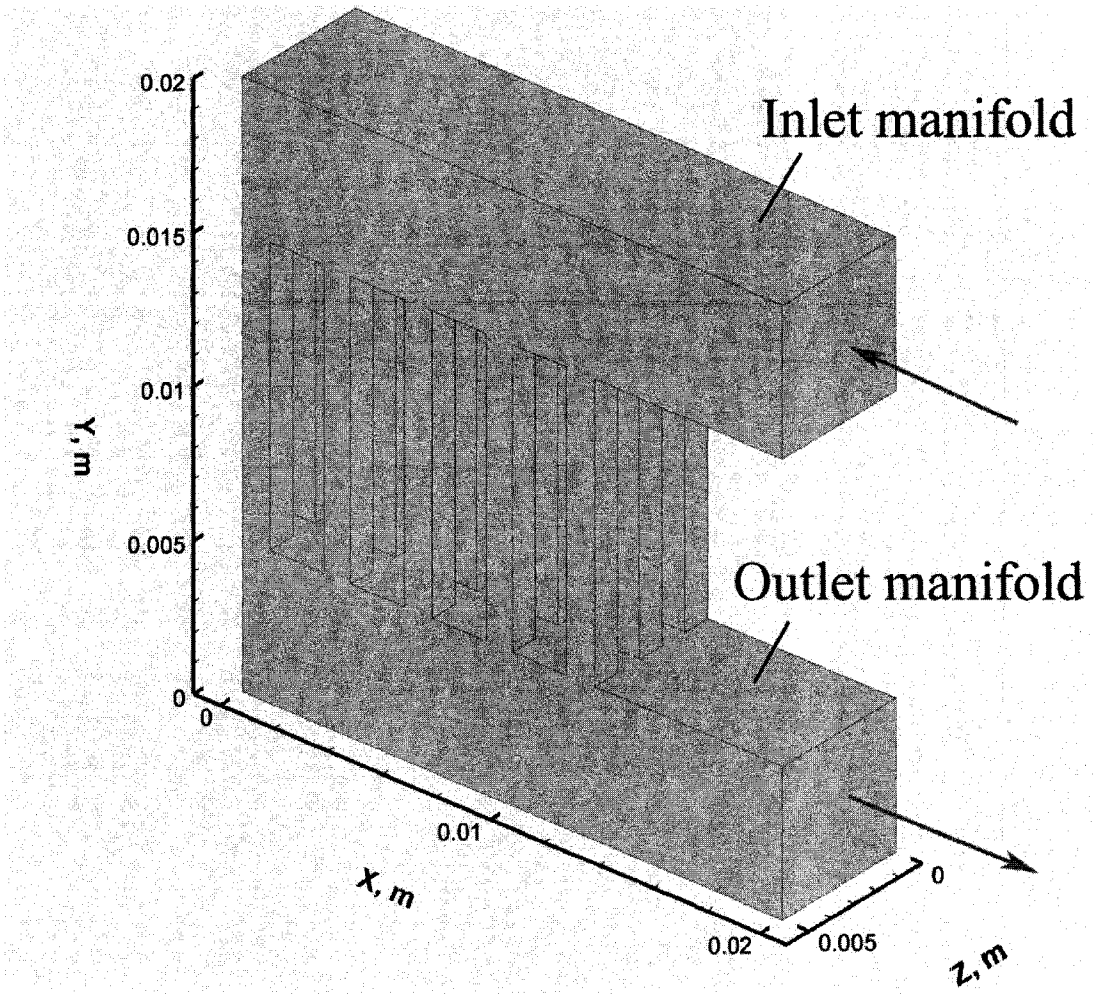

Fig. 5. Computation domain for parallel-straight PEM fuel cell stack cathode (Topic 2).

Fig. 6 illustrates the schematics of the computation domains for Topics 3 and 4 showing the three different domains that were investigated, at the top left side of Figs. 6b, 6c and 6d, the cross sections (the y-z planes) along the center-planes of the porous holes for each computation domain were shown. For Topic 3, all the three micro-structures of GDL

shown in Fig. 6 were studied, and it was found that the micro-structure of GDL shown in Fig. 6d features the best water removal ability. For Topic 4, only the best micro-structure of GDL (Fig. 6d) was considered with different wettabilities. The computation domains have the same U-shaped channel – the unit of a serpentine PEM fuel cell flow channel, with dissimilar GDL designs. The gas flow channel has a cross section of 1 × 1 mm along the y- and z-directions. Each straight section of the gas flow channel is 15 mm long. On the MEA side, small paths with different kinds of geometry are used to represent the holes on different GDLs: 0.1 × 0.1 × 0.1 mm cubes are used for the GDLs in computation domain 1; trapezoids with the height of 0.1 mm along the z-direction, and the minimum area (0.1 × 0.1 mm along the x- and y- directions) facing the catalyst layer are used for the GDLs in computation domain 2; the same trapezoids but with the minimum area facing the gas flow channel are used for the GDLs in computation domain 3. In order to keep the flow rate across the holes identical, the minimum cross sections are the same for all the computation domains (0.1 × 0.1 mm along the x- and y- directions). The location and amount of the holes are also identical for all the computation domains.

As mentioned in the introduction, the conventional GDL are not effective for water removal due to the random nature of its micro-structure and small pore size (10 to 30 micrometer). Therefore, three innovative micro-structures have been proposed in this project, as shown in Figs. 6b, 6c and 6d. Here all "pores" are well designed and structured, i.e., well-structured small holes (micro-flow-channels) connecting the gas flow channel and catalyst layer as shown in Figs. 6b, 6c and 6d. Furthermore all the computation domains have the same gap of 0.1 mm between the GDLs and the

membranes/catalyst layers. To simplify the numerical model, and because the purpose of this study is to investigate how the liquid water flows through different designs of GDLs into the gas flow channels, the gaps between the GDLs and the membranes/catalyst layers were set to be non-porous, this is corresponding to the extreme case for 100% water flooding inside the catalyst layer of a PEM fuel cell.

A Velocity Inlet boundary condition (uniform air velocity distribution of 10 m/s with a direction normal to the inlet boundary) was applied at the air inlet of the upper section of the U-shaped channel. At the outlet, the boundary condition was assigned as Outlet Flow (the gradients of all flow properties are zero). Gravity was taken as being along the negative y-direction.

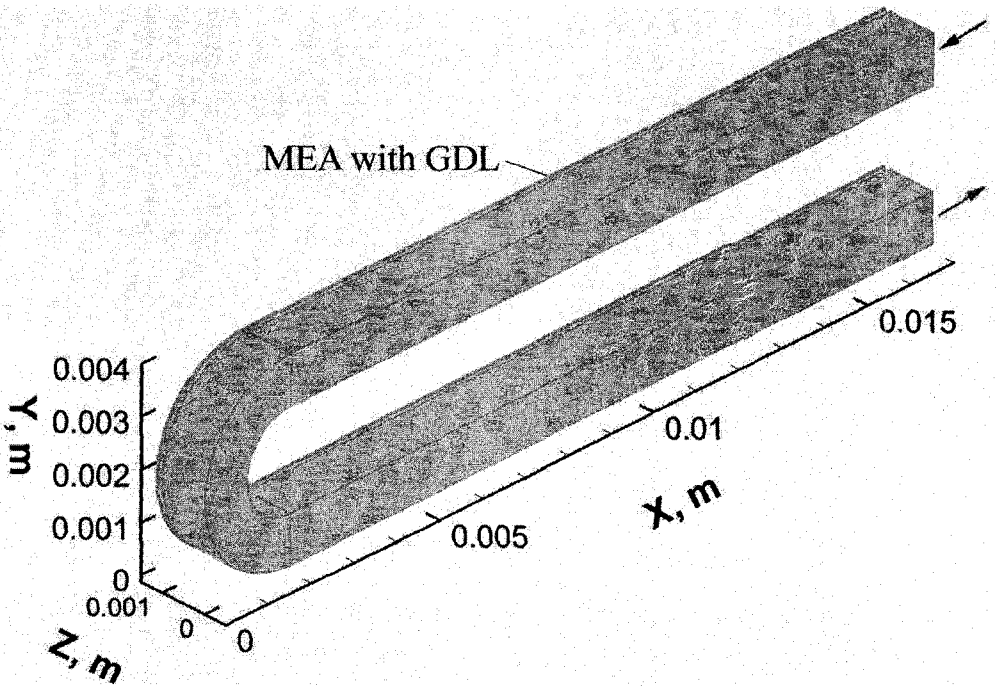

(a)

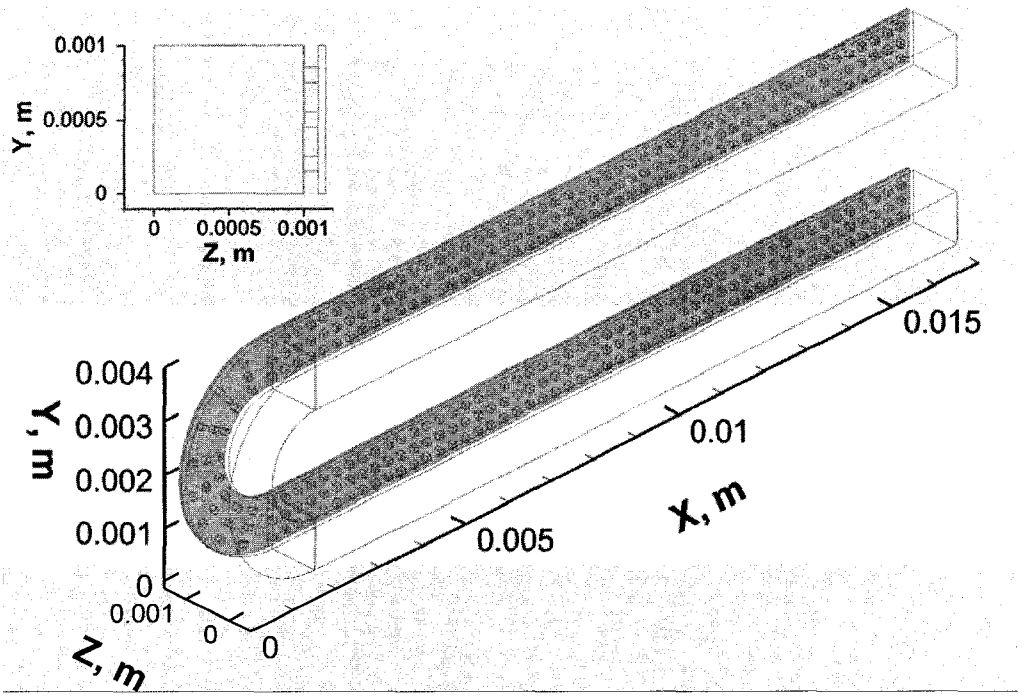

(b)

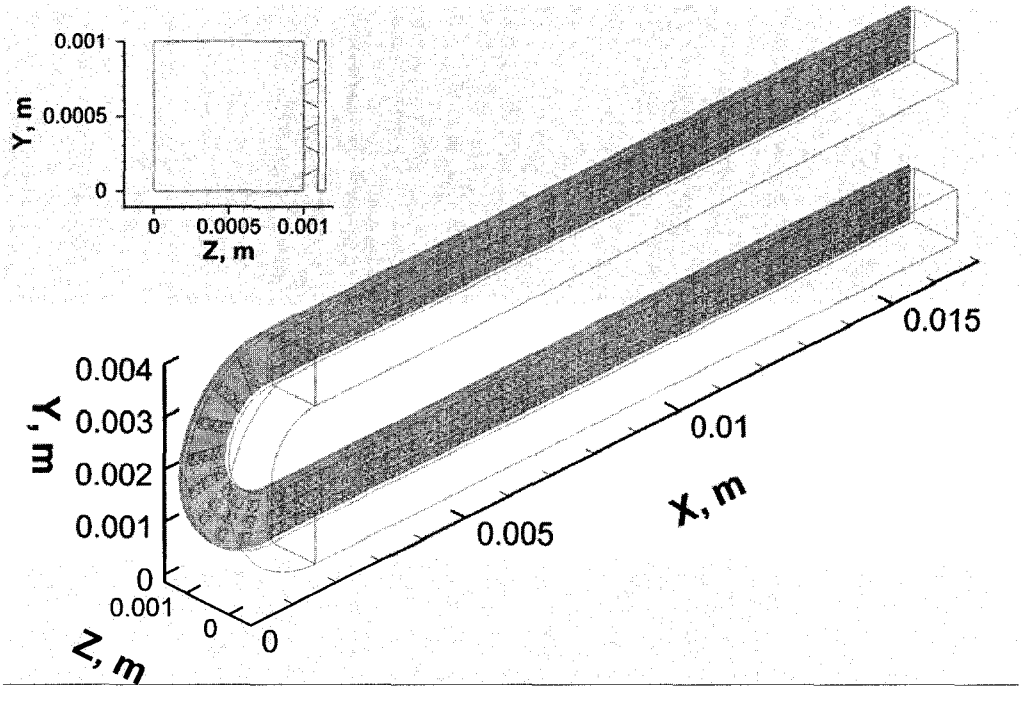

(c)

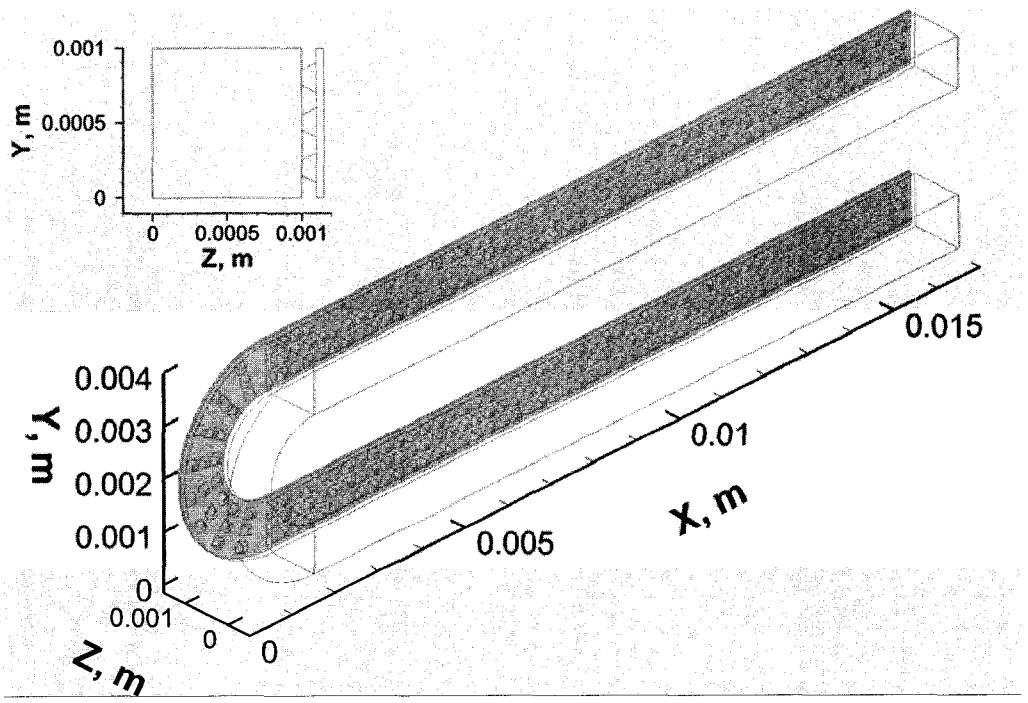

(d)

Fig. 6. Computation domains for different micro-structures of GDL with serpentine flow channel and catalyst layer (Topics 3 and 4).

(a: general view; b: computation domain 1; c: computation domain 2; d: computation domain 3)

For all the topics, the isothermal air-water transport processes inside the computation domains were modeled as 3-D two-phase viscous laminar flow. No-slip boundary conditions were applied to all the surrounding walls. To simulate water removal characteristics for all the computational domains, initial water distributions inside the computation domains were carefully set up and the details are given in later sections.

3.2 Computational methodology

The numerical simulations of the 3-D, unsteady, laminar, two-phase flow in the computation domains were performed using FLUENT [30]. An inspection of the numerical setup revealed that the Reynolds number in the models was always less than 1750, thereby verifying laminar flow assumption. No energy equations were considered thus the conservation of mass and momentum were the governing equations for the model. To track the air-water two-phase flow interface inside the computation domain, the Volume-Of-Fluid (VOF) [30] method implemented in FLUENT was used. The VOF model is designed for two or more immiscible fluids, where the position of the interface between fluids is of interest.

Then the conservation laws of mass and momentum governing unsteady, laminar flow could be written as [30]:

Continuity Equation: $\frac{\partial \rho}{\partial t} + \nabla \cdot (\rho \vec{v}) = 0$ (4)

Momentum Equation: $\frac{\partial (\rho \vec{v})}{\partial t} + \nabla \cdot (\rho \vec{v} \vec{v}) = -\nabla p + \nabla \cdot \left[\mu (\nabla \vec{v} + \nabla \vec{v}^T)\right] + \rho g + \vec{F}$ (5)

where p is the static pressure, $\vec{F}$ is the surface tension force.

Volume fraction of liquid water (α_2) could be solved by:

$\frac{\partial \alpha_2}{\partial t} + \vec{v} \cdot \nabla \alpha_2 = 0$ (6)

Then the volume fraction of air (α_1) could be calculated by using the relation:

$$\alpha_1 + \alpha_2 = 1 \quad (7)$$

All the other properties (e.g., viscosity) could be computed in a volume-fraction weighted-average manner as:

$$\mu = \alpha_2 \mu_2 + (1 - \alpha_2)\mu_1 \quad (8)$$

In the FLUENT simulation package, the surface tension is considered as a source term in the momentum equation. For two phase flow, it can be expressed as:

$$F_{vol} = \sigma_{12} \frac{\rho \kappa \nabla \alpha_1}{1/2(\rho_1 + \rho_2)} \quad (9)$$

where F_{vol} is the source term of the surface tension in momentum equation, σ_{12} is the surface tension coefficient, ρ is the volume-averaged density, and κ is the surface curvature at the interface between two phases. The surface curvature can be expressed as:

$$\kappa = \nabla \cdot \hat{n} = \nabla \cdot (\hat{n}_w \cos\theta_w + \hat{t}_w \sin\theta_w) \quad (10)$$

where $\hat{n}$ is the unit vector normal to the interface between two phases near the walls, $\hat{n}_w$ is the unit vector normal to the walls, $\hat{t}_w$ is the unit vector tangential to the walls, and θ_w is the static contact angle at the walls. As shown in Fig. 7, the contact angle is measured from the wall across liquid water. For different walls with different wettabilities, there will be different contact angles, and different contact angles will result in different surface tensions (F_{vol}), thus influencing on water transport.

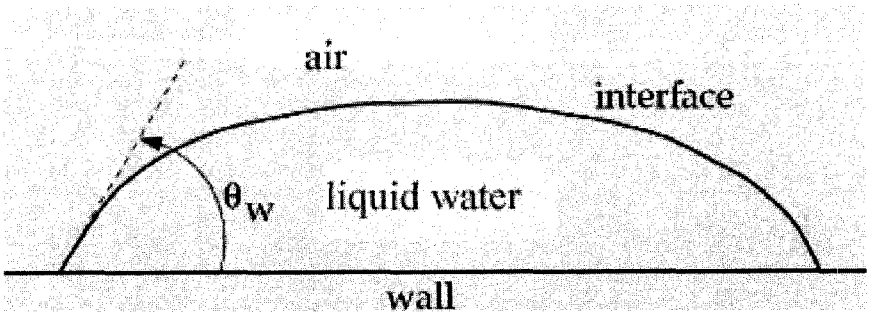

Fig. 7. Measuring the contact angle [30].

3.3 Validation of grid independency

For Topic 1, there were 198,144 cells meshed in the computation domain. Fig. 8 shows the mesh on the y-z plane. Each cell in the straight channel sections had the same size with dimensions $0.2 \times 0.2 \times 0.2$ mm (along x, y, and z directions respectively). Trapeziform cells were employed to generate the corners of the serpentine gas flow channels.

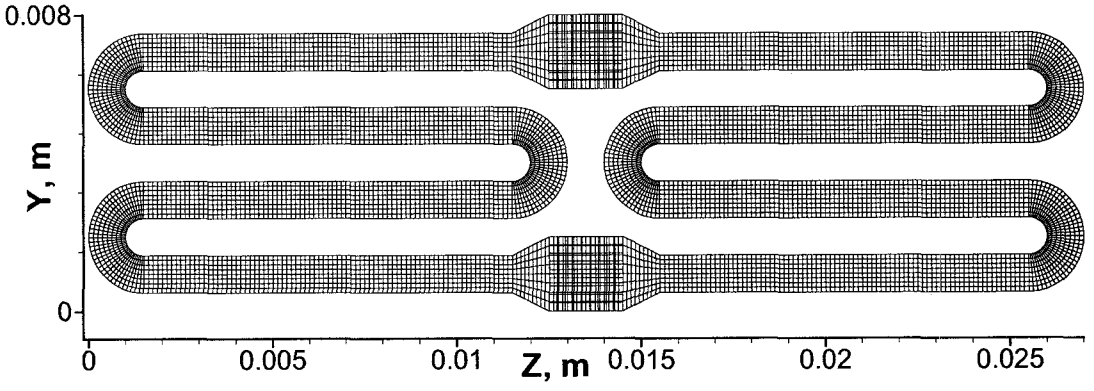

Fig. 8. Mesh on y-z plane for Topic 1.

For Topic 2, there were 65,000 cells meshed in the computation domain. Fig. 9 shows the mesh on the x-y plane. Each cell had the same size with dimensions $0.2 \times 0.5 \times 0.2$ mm (along x, y, and z directions respectively).

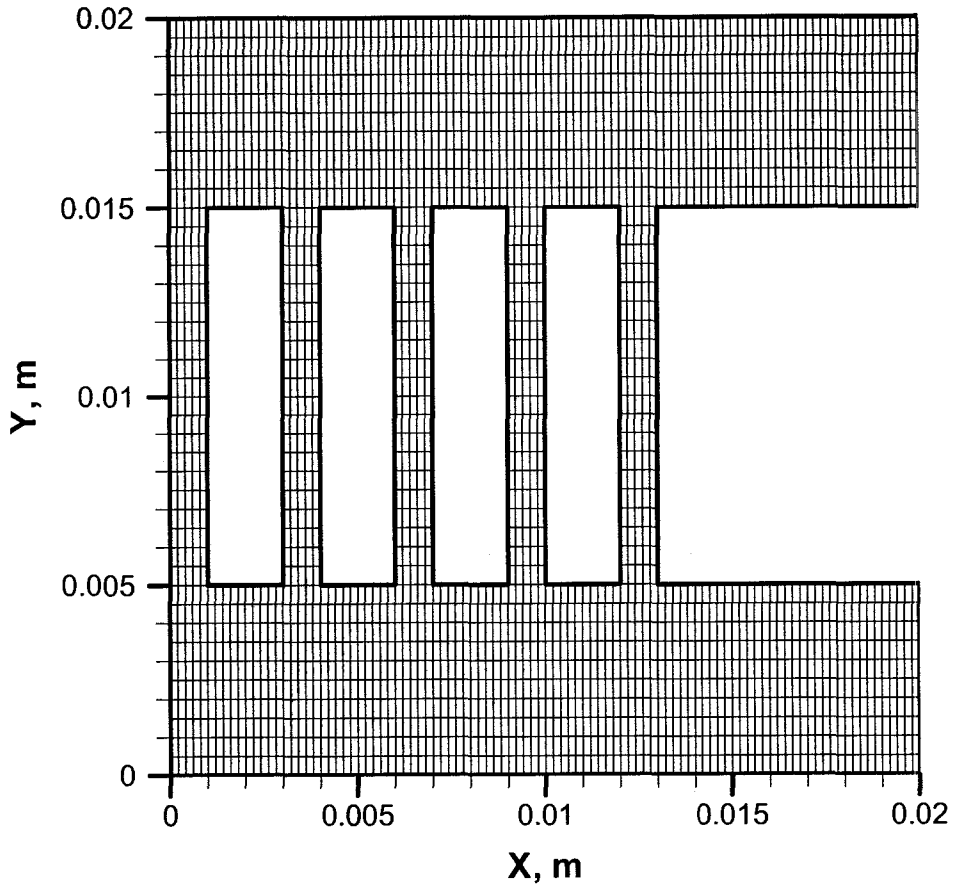

Fig. 9. Mesh on x-y plane for Topic 2.

For Topics 3 and 4, there were 821520, 423720, and 622620 cells meshed in computation domains 1, 2, and 3, respectively. Fig. 10 shows the meshes on y-z planes for the three computation domains. Each cell in the straight channel sections had the same size with

dimensions of 0.025 × 0.025 × 0.1 mm (along x, y, and z directions respectively) for computation domain 1, 0.05 × 0.05 × 0.1 mm for computation domain 2, and 0.025 × 0.025 × 0.1 mm for computation domain 3. Trapeziform cells were employed to generate the corners of the serpentine gas flow channels. In the porous sections, for all the computation domains, the holes were divided into four sections along the x- and y-directions, and five sections along the z-direction. The dimensions of the cells along the z-direction are 0.02 mm and 0.01 mm for the GDLs and the membranes/catalyst layers, respectively. This size was also identical for all the three computation domains.

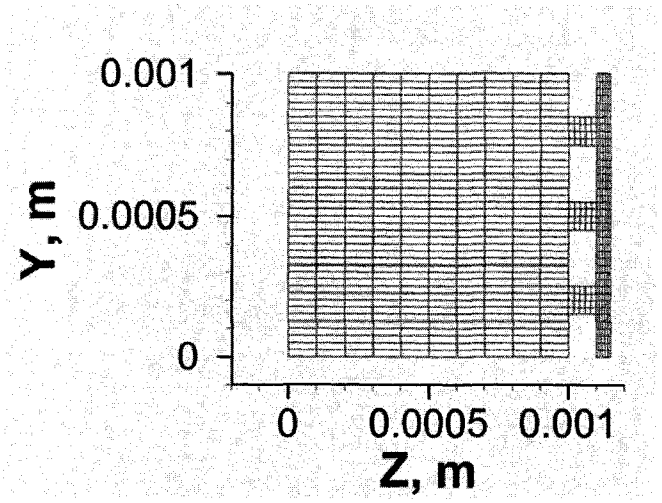

(a)

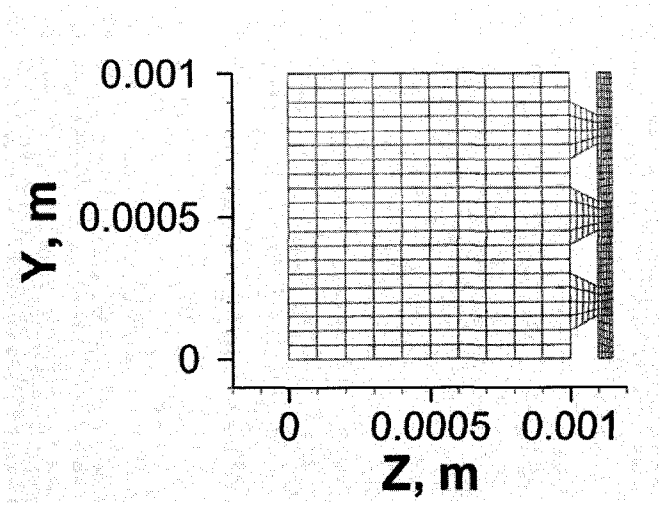

(b)

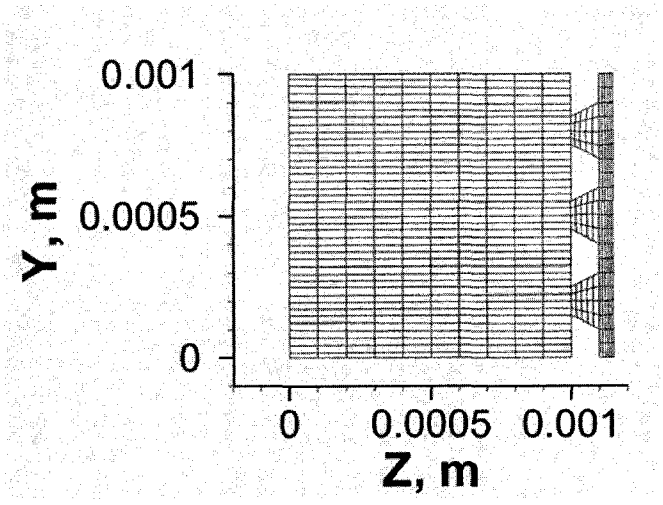

(c)

Fig. 10. Meshes on y-z planes for Topics 3 and 4.

(a: computation domain 1; b: computation domain 2; c: computation domain 3)

Grid independency was tested for all the topics. The flow phenomena of liquid water and the velocity field were almost the same. The difference in results for the different mesh systems was so small that it is negligible.

3.4 Initial water distributions

For Topic 1, in order to investigate two-phase flow behaviour inside the parallel-serpentine three-cell stack with manifolds, four different cases corresponding to four different PEM fuel cell stack operating conditions were simulated, as listed in Table 1 and shown in Fig. 11.

Table 1. Four cases in Topic 1 for different PEM fuel cell operating conditions.

Case No.	Inlet velocity (m/s)	Initial water (mm^3)	Initial water distribution	Corresponding PEM fuel cell stack operating condition
1	10	0.628	Five spherical droplets (r = 0.2 mm) freely suspended along the central line of the inlet manifold	Fundamental study of water droplet deformation inside gas flow channels; liquid water injection at the cathode inlet
2	10	6.875	Water films with a thickness of 0.2 mm attached to surrounding walls near the manifold inlet	Excessive liquid water condensed on manifold inlet surface
3	10	37.06	Water films with a thickness of 0.2 mm placed on the windward (left) side surface of each gas flow channel in the unit cells	Most of the liquid water generated on the windward side surface (MEA located here) of each unit cell gas flow channel
4	10	37.06	Water films with a thickness of 0.2 mm placed on the leeward (right) side surface of each gas flow channel in the unit cells	Most of the liquid water generated on the leeward side surface (MEA located here) of each unit cell gas flow channel

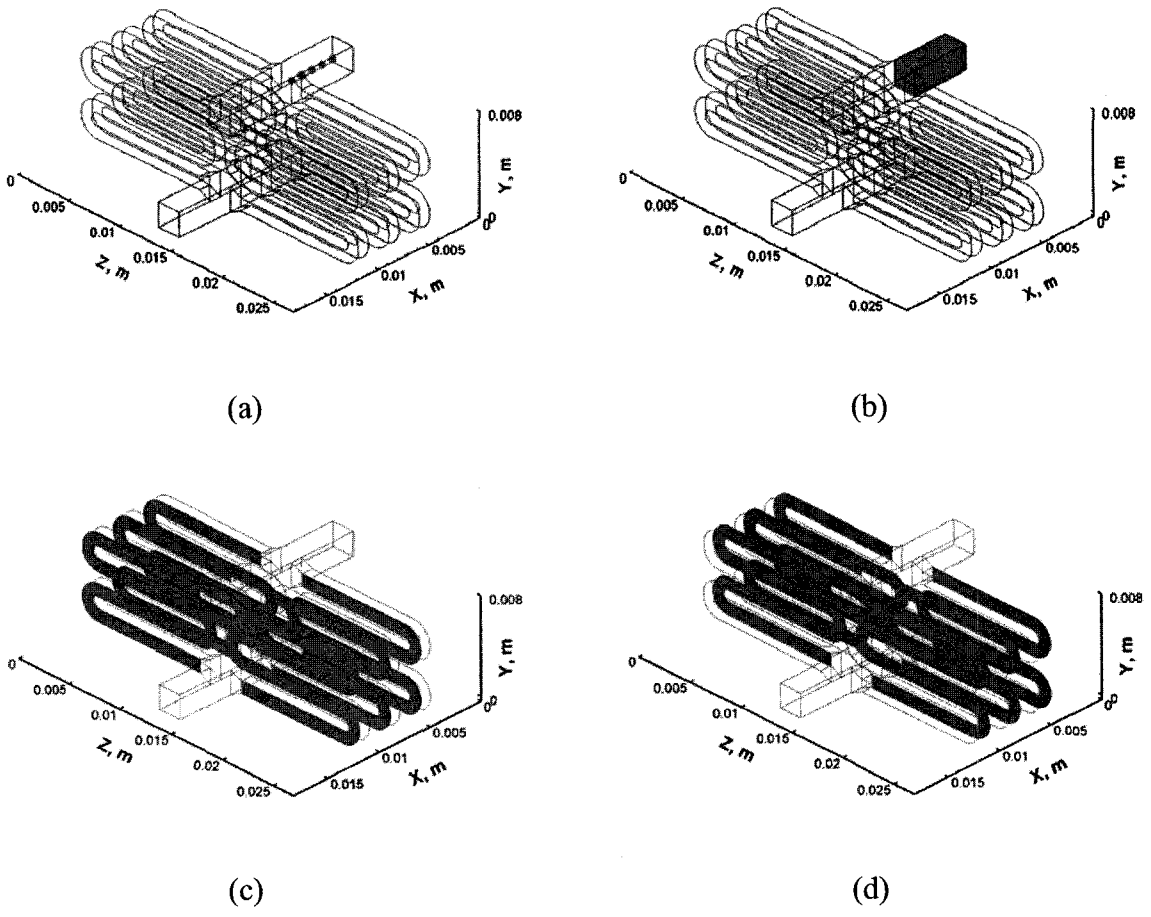

Fig. 11. Initial water distributions for the four cases in Topic 1.

(a: Case 1; b: Case 2; c: Case 3; d: Case 4)

For Topic 2, in order to investigate two-phase flow behaviour inside the parallel-straight five-cell stack with manifolds, two different cases corresponding to two different PEM fuel cell stack operating conditions were simulated, as listed in Table 2 and shown in Fig. 12.

Table 2. Two cases in Topic 2 for different PEM fuel cell operating conditions.

Case No.	Inlet velocity (m/s)	Initial water (mm^3)	Initial water distribution	Corresponding PEM fuel cell stack operating condition
1	5	30	Water films with a thickness of 0.2 mm placed on the leeward (right) side surface of each gas flow channel in the unit cells	Most of the liquid water generated on the leeward side surface of each unit cell gas flow channel
2	5	30	Water films with a thickness of 0.2 mm placed on the windward (left) side surface of each gas flow channel in the unit cells	Most of the liquid water generated on the windward side surface of each unit cell gas flow channel

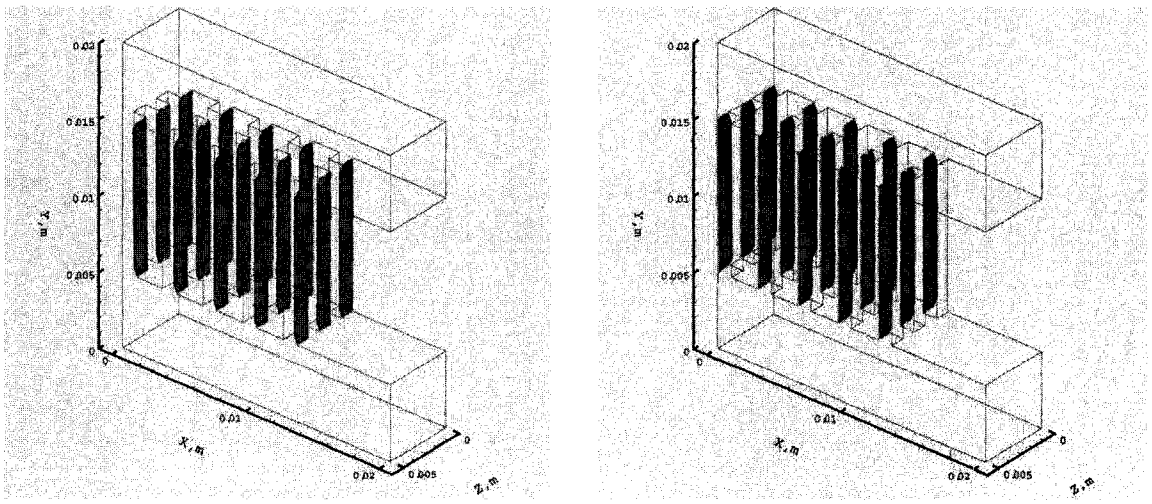

(a) (b)

Fig. 12. Initial water distributions for the two cases in Topic 2.

(a: Case 1; b: Case 2)

For Topic 3, in order to investigate two-phase flow behaviour across the GDLs, three different cases corresponding to different computation domains were simulated as listed

in Table 3. A liquid water film was initially placed on the membranes to investigate the water removal characteristics. Fig. 13 shows the arrangement of the initial water distribution.

Table 3. Three cases in Topic 3 with different GDLs.

Case No.	Computation domain No.	Inlet velocity (m/s)	Initial film thickness (mm)	Initial water (mm^3)	Corresponding PEM fuel cell operating condition
1	1	10	0.03	1.04	Water flooding for case with proposed GDL
2	2	10	0.03	1.04	Water flooding for case with proposed GDL
3	3	10	0.03	1.04	Water flooding for case with proposed GDL

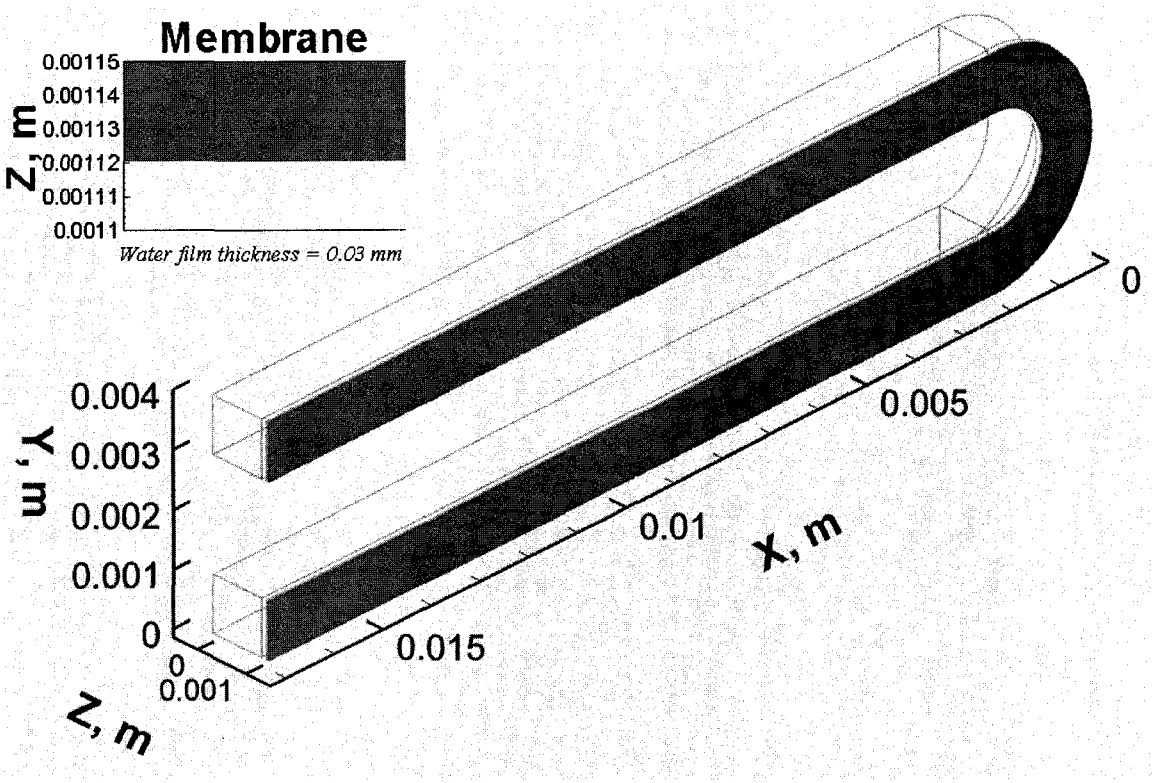

Fig. 13. Initial water distributions for Topics 3 and 4.

For Topic 4, in order to investigate two-phase flow behaviour across the GDL shown in Fig. 6d, three different cases corresponding to different static contact angles of GDL and catalyst layer were simulated as listed in Table 4. Case 1 considered the GDL (the surrounding surfaces of the small holes and the surfaces at both ends of the small holes) as hydrophilic (static contact angle of 45°), Case 2 considered the GDL as hydrophobic (static contact angle of 135°), Case 3 considered the cathode electrode (all the surfaces of the GDL and the catalyst layer) as hydrophobic (static contact angle of 135°). A liquid water film was initially placed on the membranes to investigate the water removal characteristics. Fig. 13 shows the arrangement of the initial water distribution.

Table 4. Three cases in Topic 4 with different GDLs and catalyst layers.

Case No.	Static contact angle	Inlet velocity (m/s)	Initial film thickness (mm)	Initial water amount (mm^3)	Corresponding PEM fuel cell operating condition
1	45° (hydrophilic) for GDL	10	0.03	1.04	Water flooding for case with proposed hydrophilic GDL
2	135° (hydrophobic) for GDL	10	0.03	1.04	Water flooding for case with proposed hydrophobic GDL
3	135° (hydrophobic) for GDL and catalyst layer	10	0.03	1.04	Water flooding for case with proposed hydrophobic GDL and hydrophobic catalyst layer

CHAPTER 4

ANALYSIS OF RESULTS – TOPIC 1

4.1 Case 1: Five spherical droplets freely suspended in the inlet manifold

The first case was simulated to consider small amount of water transport and distribution. As shown in Fig. 11a, five freely suspended water droplets with radius of 0.2 mm were placed along the centerline of the inlet manifold. The water distribution in different cells and manifolds, water transport in the serpentine unit cells, pressure drop along different volumes, and deformation of small water droplets were studied.

4.1.1 Water droplets deformation

Fig. 14 shows water droplet behaviour versus time as the droplets traveled through the inlet manifold on the vertical center-plane with z = 0.0135 m. At t = 0, five freely suspended droplets, with their original spherical shape, were placed in the inlet manifold. Subsequently, droplet deformation along the x-direction, attributable to effects of dragging force from the airflow, could be noticed. Since the size of the water droplets was very small, the effect of gravity was not significant. The droplet on the far right section (near the inlet) had the largest deformation along the x-direction. However, the droplet on the far left section had its original spherical shape and was only slightly elongated along the x-direction. Because airflow originated at the inlet, the interaction between airflow and the water droplets was significant for the droplet on the far right section (near the inlet). Furthermore, the droplet on the far right section blocked some of the airflow resulting in reduced airflow effects on the other droplets. In other words, shear stress on the droplets would keep decreasing along the main flow direction (to the

left in Fig. 14) and correspondingly, the droplets on the left side would maintain their original shapes rather than deforming. Therefore, it could be concluded that the droplets closest to the air inlet suffered the largest air dragging forces than the droplets far away from the air inlet.

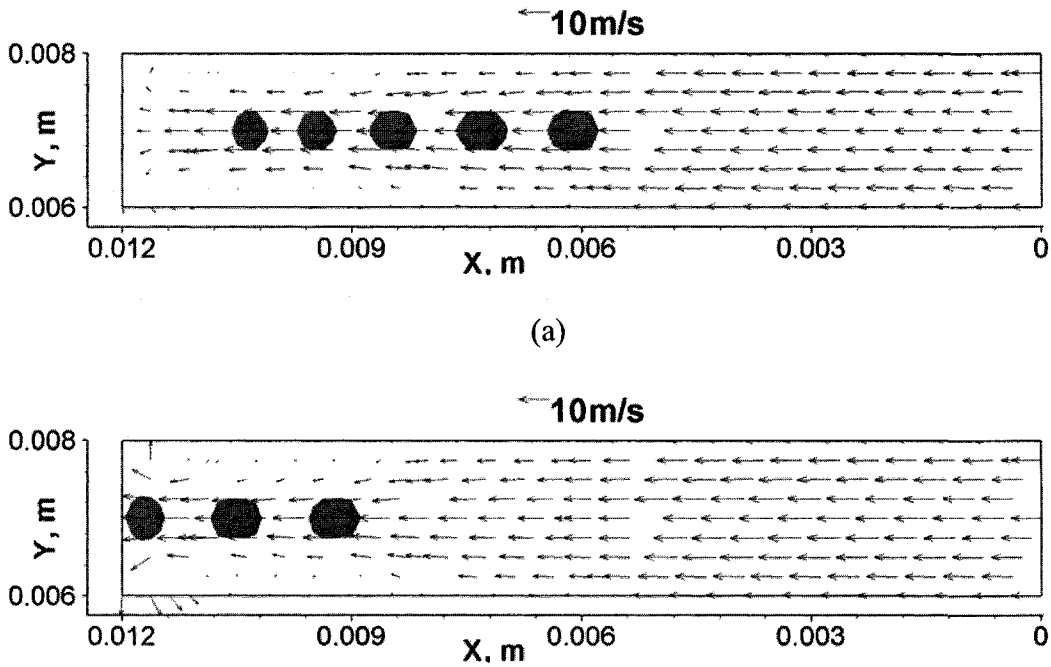

Fig. 14. Water distribution and velocity field on the vertical center-plane (z = 0.0135 m) in the inlet manifold for Case 1.

(a: t = 0.006 s; t = 0.009 s)

4.1.2 Water amount distribution and its effects on velocity fields

When the water droplets approached the end wall (at x = 0.012 m) of the inlet manifold, the velocity field at the near-wall surfaces would change with liquid water displacement.

Fig. 15 shows how the velocity field was affected by liquid water movement on the plane close to x = 0.012 m. The upper section of this figure shows the cross-section of the inlet manifold, it also shows that airflow was reflected at the near-wall surfaces. With water approaching the surface, the velocity increased due to the squeeze effect between the wall and the water droplets and hence forced all the liquid water to expand to both sides along the z-direction (Fig. 15b). Simultaneously, water would be divided into two parts to the both sides of the gas flow channels. The lower section in this figure shows the cross section of the outlet manifold. The two outgoing air streams flowing out of the gas flow channels squeezed each other. After water spread to the gas flow channels, as shown in Fig. 15c, there is still a small amount of water adhering to the wall, attributable to the effect of wall adhesion and the stagnant effect.

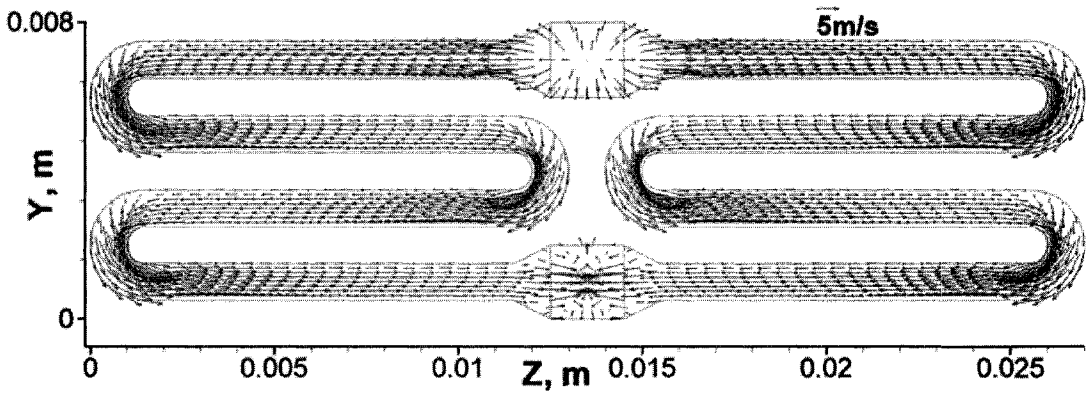

(a)

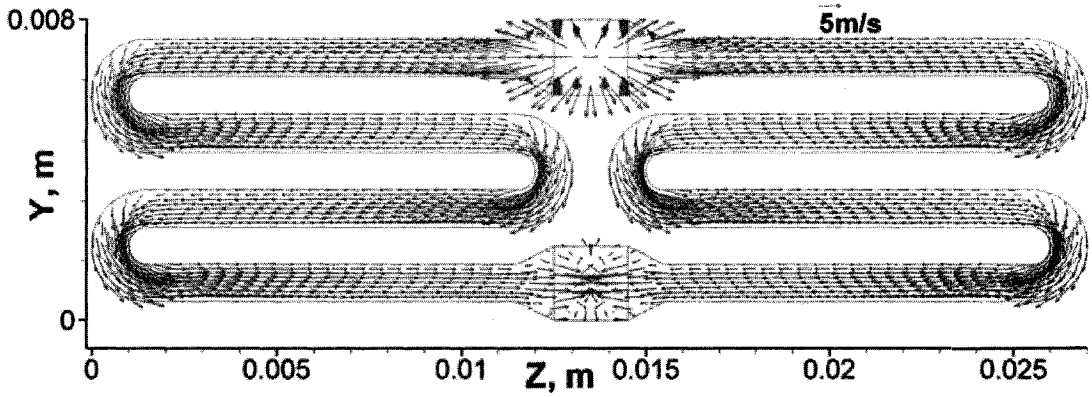

(b)

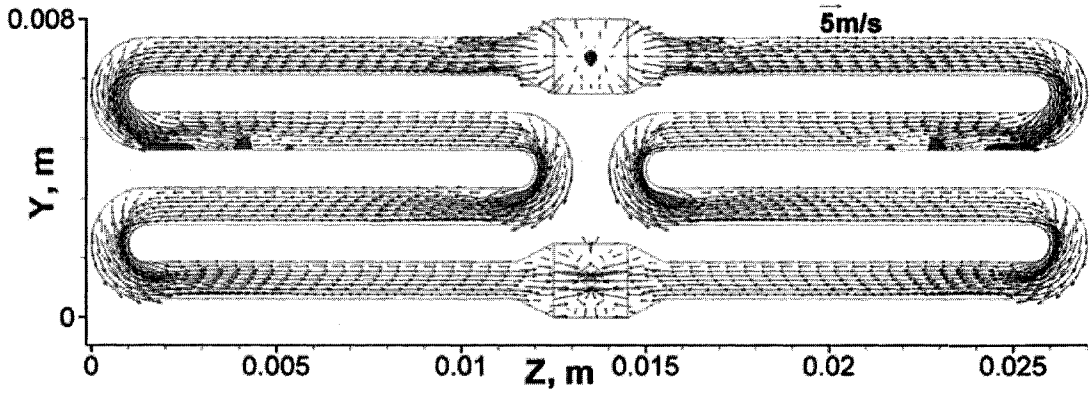

(c)

Fig. 15. Water movement on the plane close to the wall at x = 0.012 m for Case 1, the inlet manifold is at the top and the outlet manifold is at the bottom.

(a: t = 0.0003 s; b: t = 0.0009 s; c: t = 0.006 s)

Water distribution in 3-D view was shown in Fig. 16, it could be observed that there was almost no water traveling through the Cells 1 and 2. In other words, the water was not evenly distributed among all the cells. Fig. 17 describes the relative amount of water in different cells and manifolds, Cells 1 and 2 had zero variation of water amount. There was no water flowing into these two cells and the water amounts remained zero all the time. From Fig. 16, it was observed that all the five water droplets were flowing onto the

end wall (x = 0,012 m) facing the air inlet. Eventually, water started spreading on that wall and moved into Cell 3. Fig. 17 also shows the process from 0.0008 to 0.0015 s during which the amount of water in the inlet manifold decreased rapidly, while increased in Cell 3. Subsequently, the water amount in these two volumes remained constant for a while, while water was flowing through Cell 3. It could also be observed that there was about 4 % of water remained in the inlet manifold. Also in Cell 3, the relative water amount remained about 96 % for most of the time. As mentioned earlier, this was due to the wall adhesion, and some of the water hitting that wall would stick onto it, as shown in Figs. 15c and 16. Also Figs. 15 and 16 show that even the outgoing air streams were trying to squeeze each other in the outlet manifold, water still moved toward the outlet, which is good for water drainage. The overall water amount inside the cathode (stack) versus time is shown in Fig. 18, at t = 0.04 s, water started moving out from the stack indicated by the decrease of the curve. This curve decreased three times, this means water was collected and separated into three parts to flow out of the channel, this could also be observed from Fig. 16c. The "collecting-and-separating-effects" from the serpentine shape will be discussed further in the next three cases. Generally, it was found that it is difficult to attain an even water distribution for these kinds of parallel gas flow channels. And once most of the water has moved into one cell, the performance of the fuel cell would decrease due to either unstable operation or water flooding.

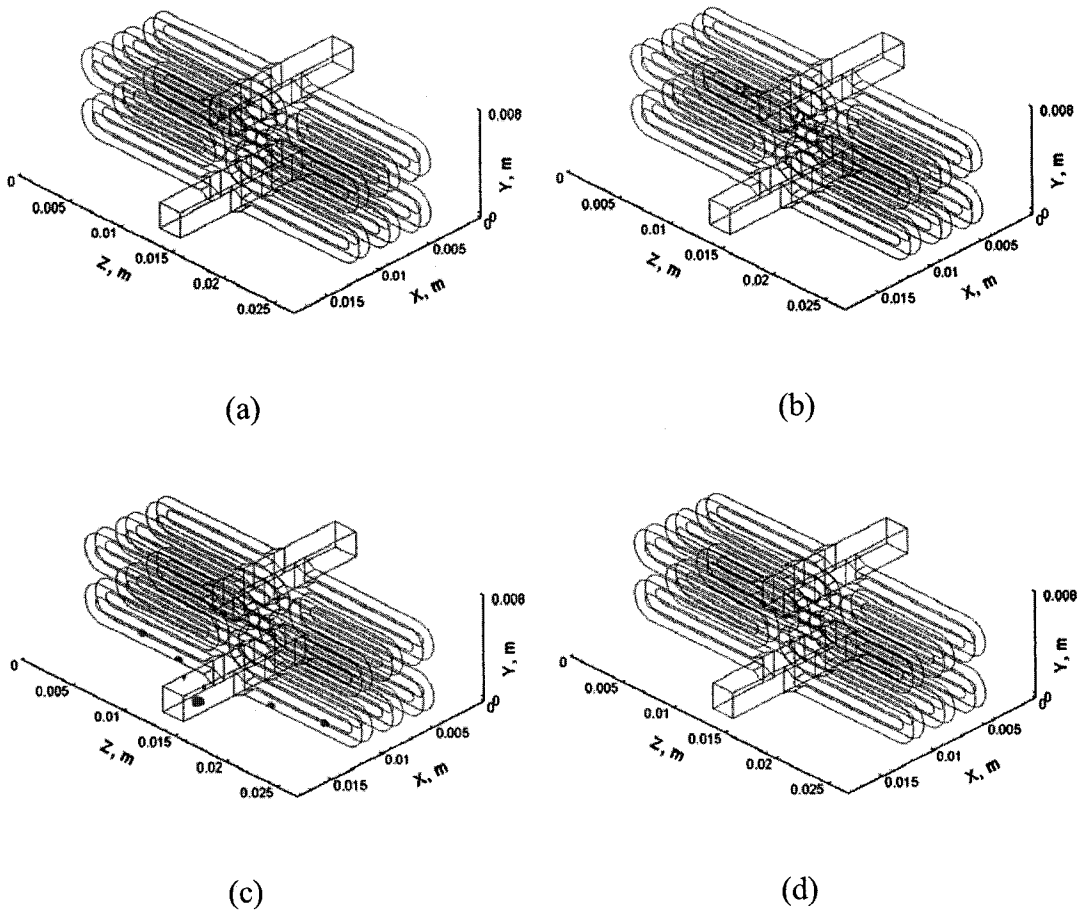

Fig. 16. Water movement in 3-D view for Case 1.

(a: t = 0.0009s; b: t = 0.0015 s; c: t = 0.045 s; d: t = 0.06 s)

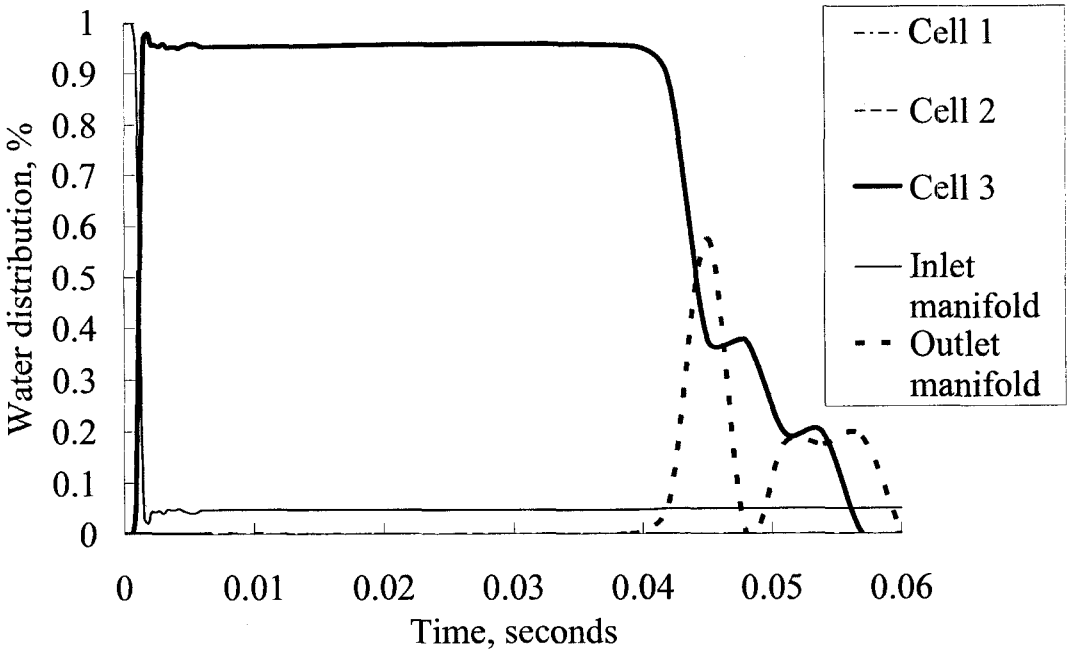

Fig. 17. Water amount variation in different cells and manifolds for Case 1.

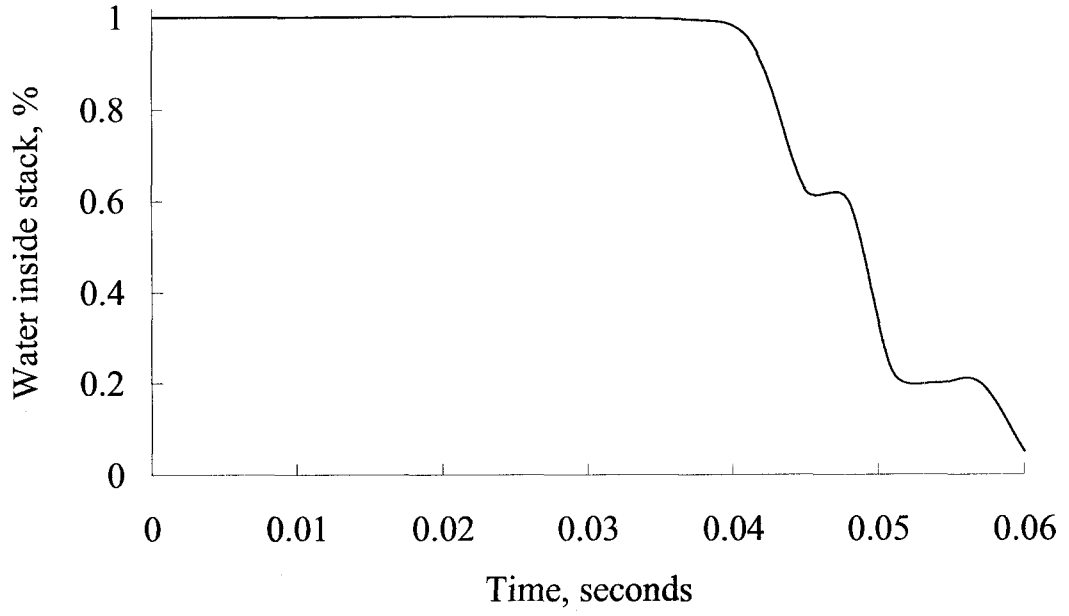

Fig. 18. Water amount inside stack versus time for Case 1.

4.1.3 Pressure drop change due to water movement inside the inlet manifold

Fig. 19 shows the pressure drop along different volumes for Case 1. It could be observed that the pressure drop along Cell 3 was always greater than that along Cells 1 and 2. Recalling the general calculation of pressure drop along a horizontal pipe without considering gravity force (gravity effect is minor factor for the present study due to the size of droplets and small amount of liquid water) [31], with equation:

$$\Delta p = f \frac{l}{D} \frac{\rho V^2}{2} \quad (11)$$

with f is the friction factor, l is the length, D is the hydraulic diameter, and V is the velocity. For all the three single cells, they have the same geometry, thus the main factor that affect the pressure drop is the water amount. Different water amount in the single cell would change the available cross-section area of the channel for gas to pass through and thus the gas flow velocity would be different. At t = 0, there was no water in the three single cells, the pressure drop in Cell 3 is still the highest, this means that Cell 3 always had a greater flow rate of air than the other two cells, and Cell 3 could be the easiest one to flow in. At about 0.001 s, while water hit the wall facing the air inlet, the pressure drop along Cell 3 increased significantly. This is because air was squeezed from the end wall (x = 0.012 m) by water hitting on it. As all that water moved into the cell, the pressure drop decreased. Cell 3 always has a greater pressure drop than that of the other two cells, it could be considered as the unit cell with the highest possibility of having most of the water flowing through (as in this case). This would also be demonstrated in the next three cases.

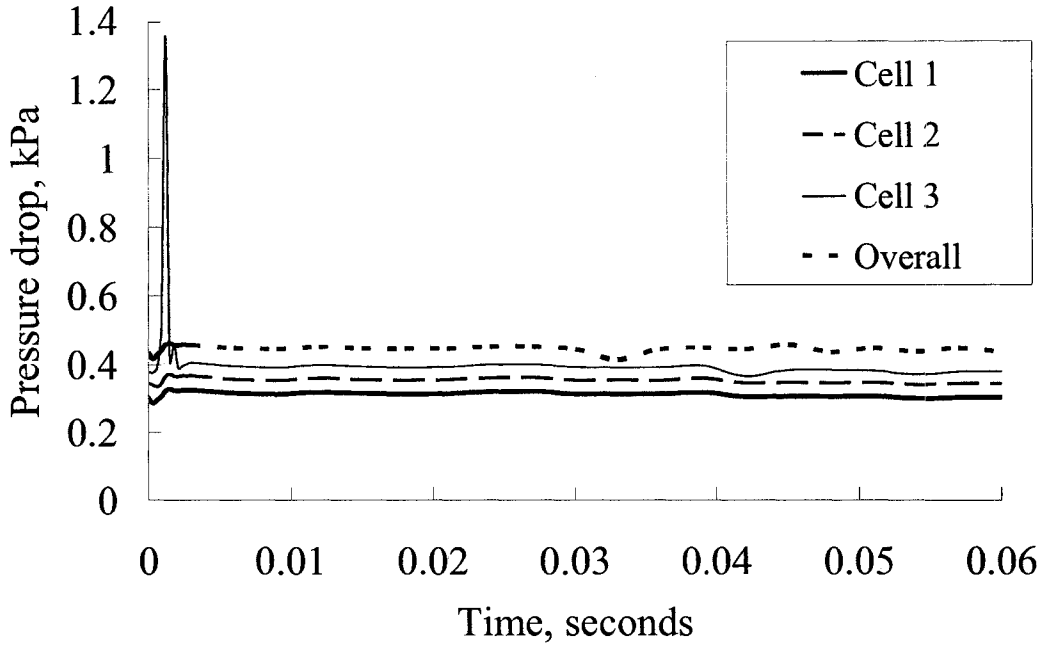

Fig. 19. Pressure drop along different volumes for Case 1.

4.2 Case 2: Water films with a thickness of 0.2 mm attached to the surrounding walls near the manifold inlet

Four water films with thickness of 0.2 mm were attached to the surrounding walls, as shown in Fig. 11b. All the water films were 5 mm long. Water was expected to move into all the three unit cells, the variations of water amount and pressure drop in each volume could perform more significantly.

4.2.1 Water "flowing backward"

Fig. 20 shows the water transport and velocity field on the vertical center plane with z = 0.0135 m of the inlet manifold. The gravity force acts in the negative Y-direction. At t = 0.0003 s, the water films were already flowing away from the air inlet. Part of water close to the air inlet was slightly lifted up by the air stream. The amount of water was small for

such an air stream to have gravity effects significantly shown in the figure. At a later time, water hit the end wall that faces the air inlet, and air was squeezed from the end wall at x = 0.012 m. There were two vortices formed at the top and bottom of the inlet manifold, as water approached the wall, as shown in Figs. 20a and 20b, the vortices were squeezed and the velocity vectors directed toward the air inlet became much stronger. Water started moving back to the air inlet as shown in Figs. 20c and 20d. At t = 0.009 s, some water already moved half way in the inlet manifold (Fig. 20d). Because air was continuously flowing from the air inlet, therefore, water was flowing downstream again to the end wall, as shown in Fig. 20e. During this time period, gravity effects gradually became important and could be noticed as shown in Figs. 20c through 20f. When this part of water moved back to the end wall at x = 0.012 m, it already moved down to the bottom surface of the inlet manifold and adhered to the surrounding walls as shown in Fig. 20f. The reason that some water flowed backwards after hitting the end wall of the inlet manifold is because water was reflected from this wall. While water started moving back, the air flow resistance was not significant, as shown in Fig. 20c, the velocity filed on the left side of the water is very small; this is because there are other channels that air could move into (Cells 1 and 2). Therefore, water could flow backward to the air inlet for such a long distance.

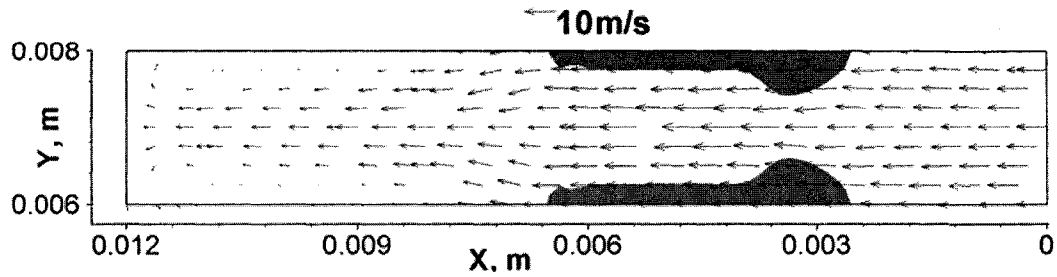

(a)

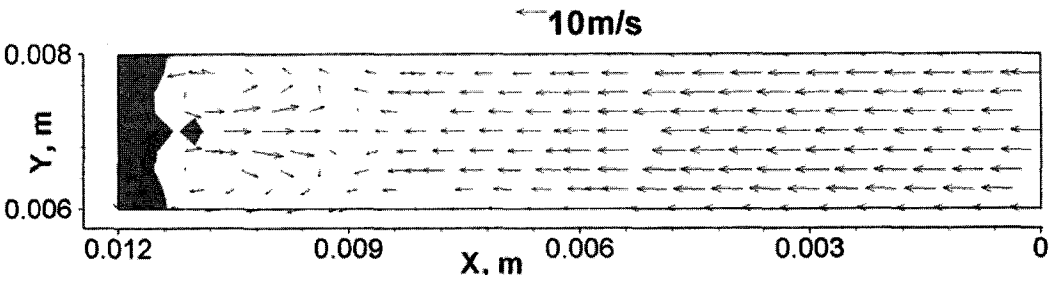

(b)

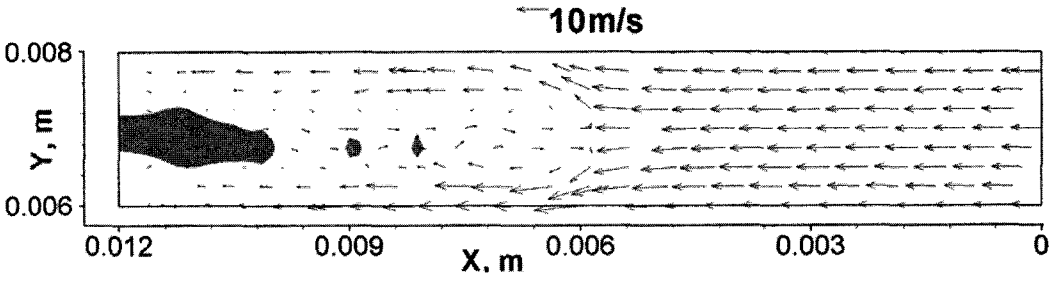

(c)

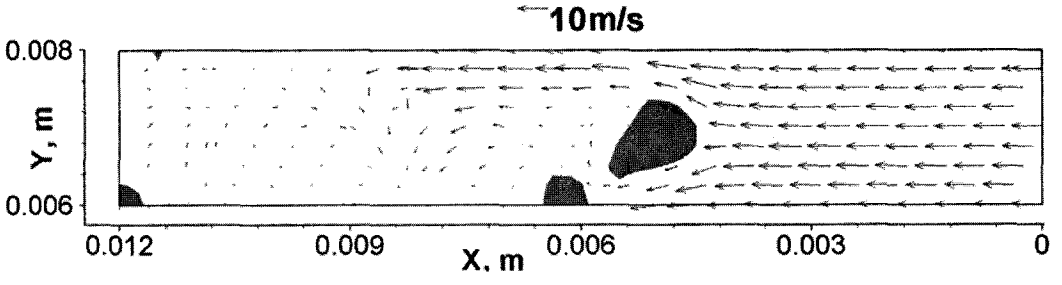

(d)

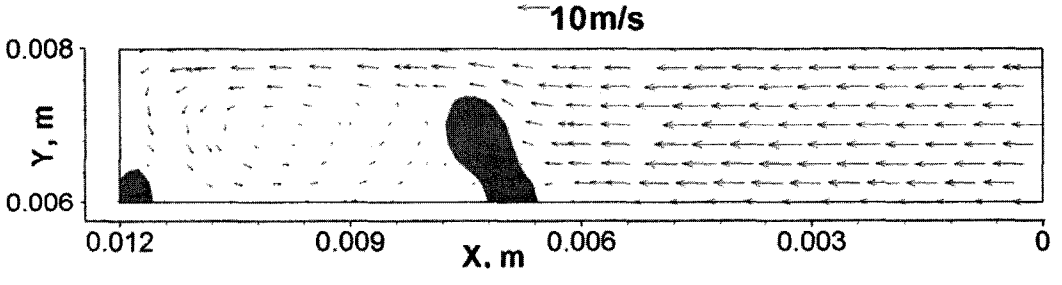

(e)

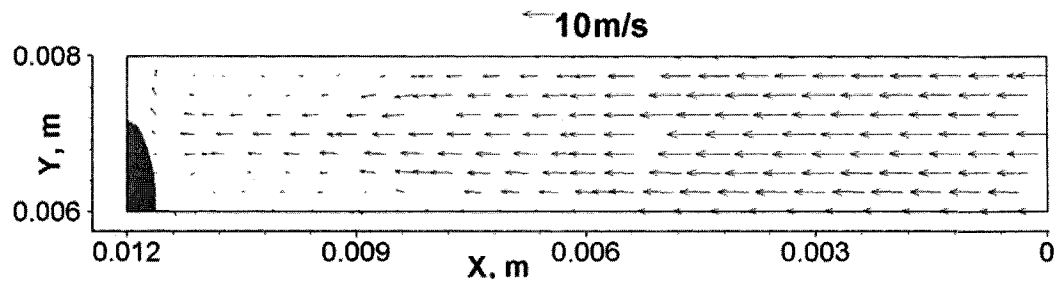

(f)

Fig. 20. Water distribution and velocity field on the vertical center-plane (z = 0.0135 m) in the inlet manifold for Case 2.

(a: t = 0.0003 s; b: t = 0.0012 s; c: t = 0.0024 s; d: t = 0.009 s; e: t = 0.012 s; f: t = 0.018 s)

4.2.2 Water amount variation

Fig. 21 shows water movement in 3-D view, as time progressed, different from the first case; water was distributed to all the three cells. Fig. 22 shows the variation of water amount in different volumes. For most of the time, Cell 3 had the largest amount of water (about 65% of total amount of initially-loaded water). Cell 1 with about 15% total amount of initially-loaded water was slightly more than that in Cell 2 (10%). From Fig. 21d, it could be observed that some water remained on the end walls of both the inlet and outlet manifolds. With help of Fig. 22, at time t = 0.08 s, we could find that about 10% of water sticking on the end wall of the inlet manifold, and 4% sticking on the end wall of the outlet manifold. The reason that we have water sticking on the end wall of inlet manifold was discussed in Case 1. The water transport in the outlet manifold will be discussed in the next section. The variation of overall water amount inside the cathode (stack) was shown in Fig. 23. The decreasing curve is similar to Fig. 18 for Case 1, the reason that the curve is decreasing step by step is because water was collected and

separated into several parts through the serpentine flow channels. In this case water started moving out of the stack at about 0.032 s, this is earlier than that in Case 1. At last, water amount remained at about 14%, which represents the water in both the inlet and outlet manifolds.

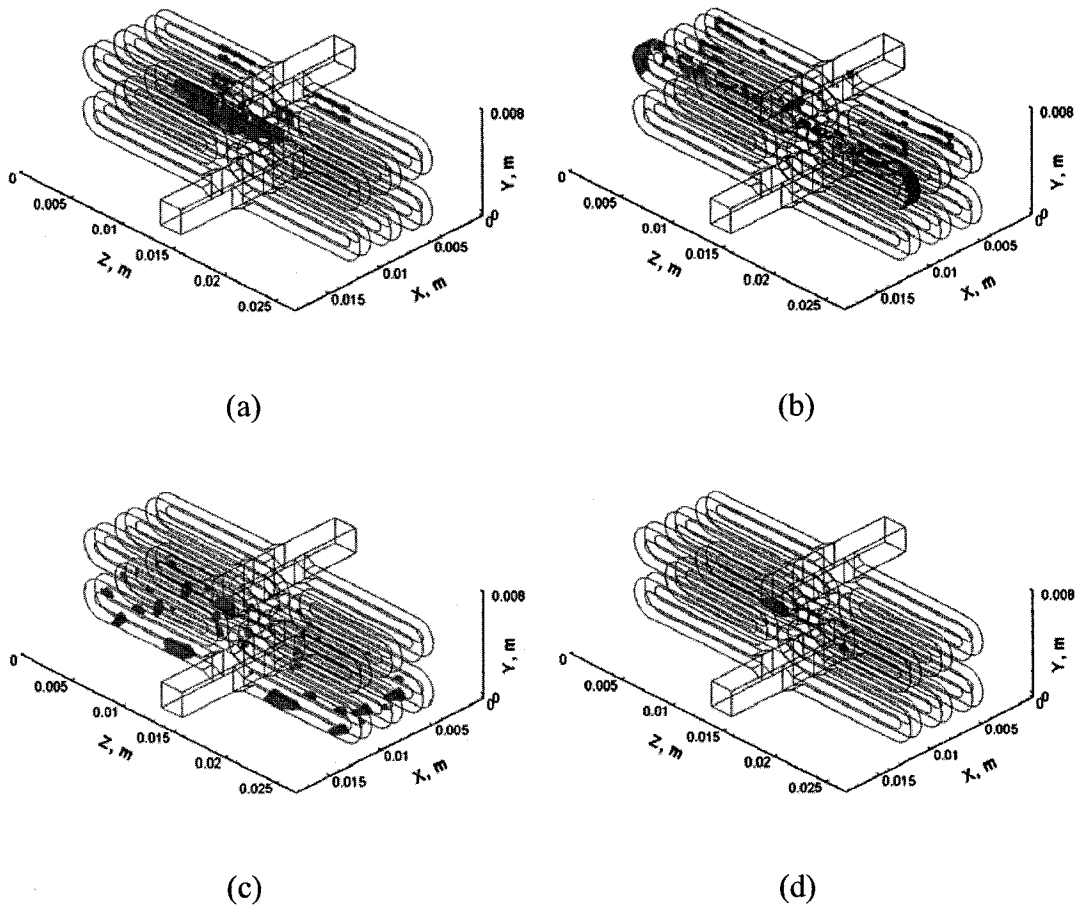

Fig. 21. Water movement in 3-D view for Case 2.

(a: t = 0.0015 s; b: t = 0.003 s; c: t = 0.03 s; d: t = 0.082 s)

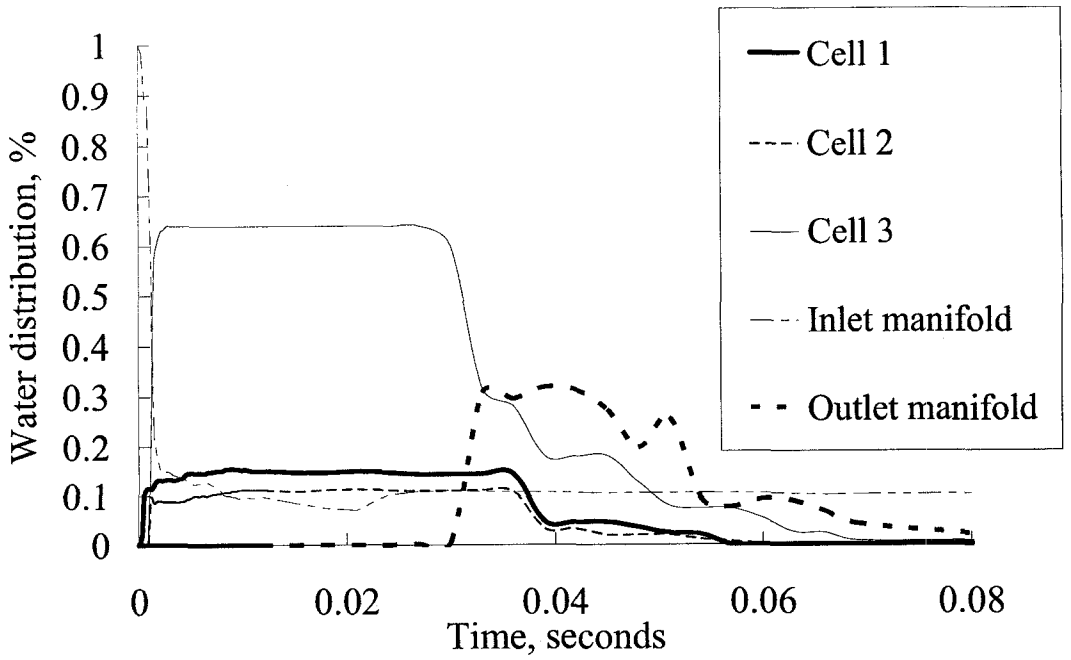

Fig. 22. Water amount variation in different cells and manifolds for Case 2.

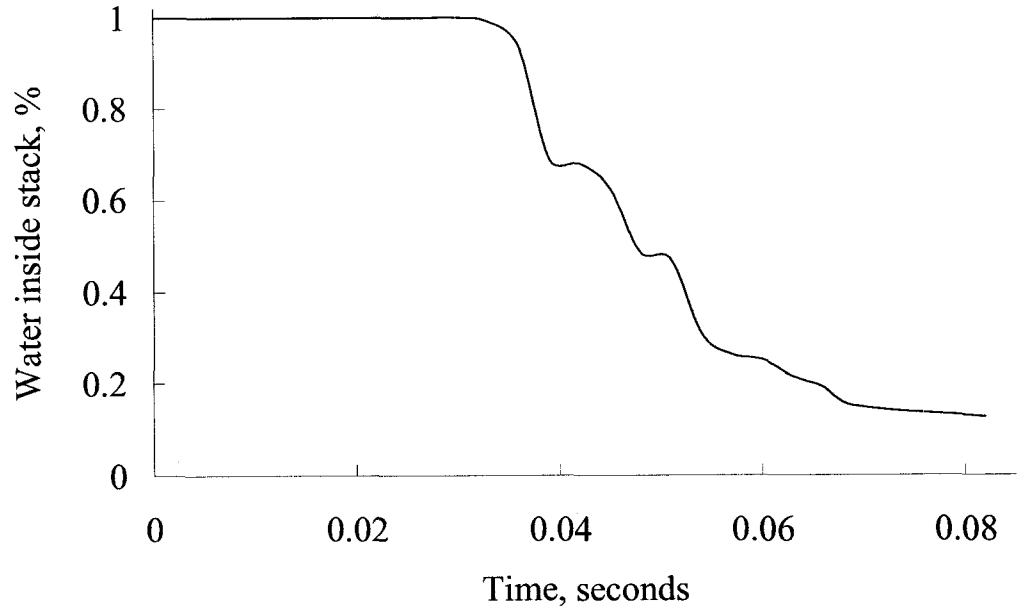

Fig. 23. Water amount inside stack versus time for Case 2.

4.2.3 "Squeezing" of water in the outlet manifold

Fig. 24 shows the vertical center plane with z = 0.0135 m of the outlet manifold. Water flowed into the outlet manifold from both sides of the gas flow channels and then would amalgamate on this plane. The air streams from both sides of gas flow channels would also squeeze each other on this plane. As shown in this figure, as time progressed, water was flowing onto this plane and then was squeezed to move along both the positive- and negative-x directions. After that, this part of water was tearing up, as shown in Fig. 24c. At a later time, as shown in Figs. 24d and 24e, some water from Cell 1 moved onto this plane, after being squeezed to both sides along the x-direction, some water moved onto the end wall (x = 0.005 m) of the outlet manifold and adhered to it. Therefore, due to the effect of wall adhesion and surface tension, the water sticking on this wall would be hard to move to anywhere else, thus explaining why some water remained in the outlet manifold.

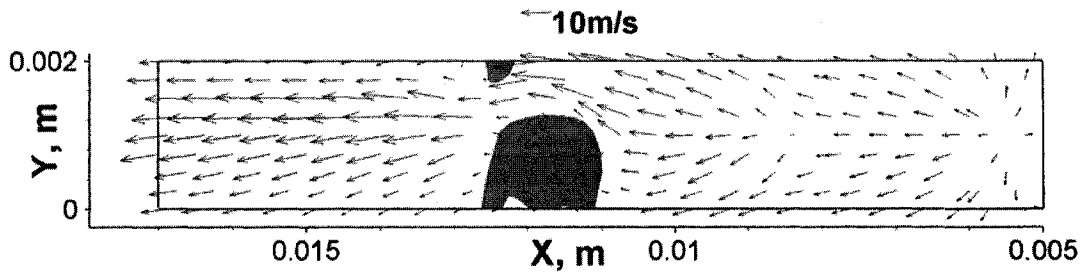

(a)

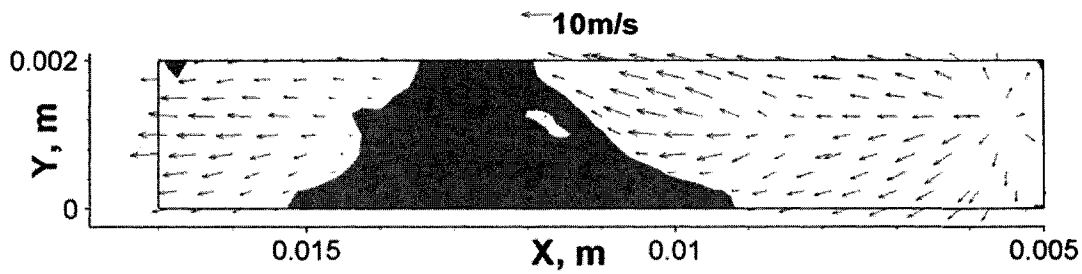

(b)

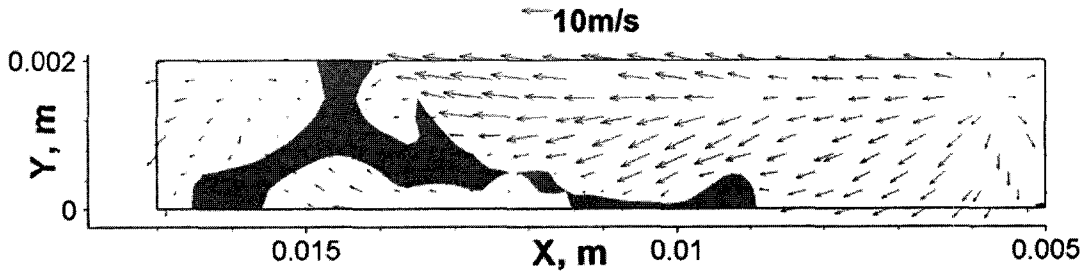

(c)

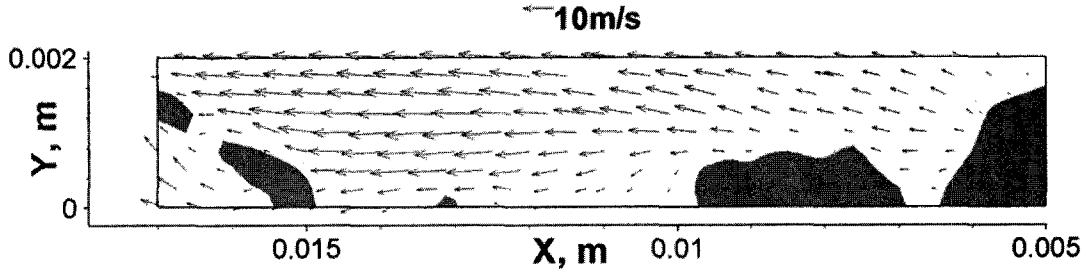

(d)

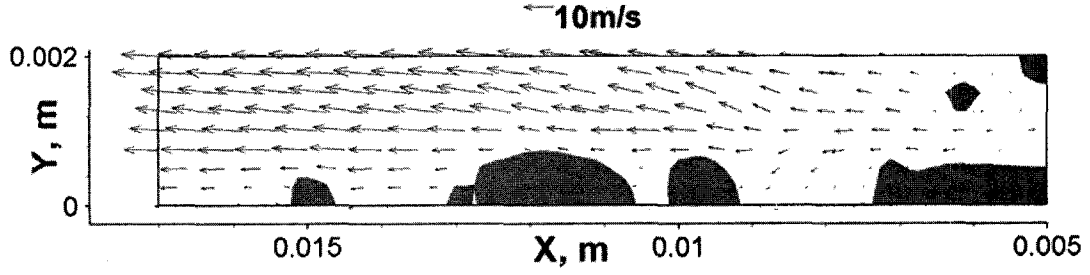

(e)

Fig. 24. Water distribution and velocity field on the vertical center-plane (z = 0.0135 m) in the outlet manifold for Case 2.

(a: t = 0.033 s; b: t = 0.0345 s; c: t = 0.036 s; d: t = 0.0375 s; e: t = 0.039 s)

4.2.4 Comparison of both pressure drop and flow behaviour of Cases 1 and 2

As shown in Fig. 25, the pressure drop changed more dramatically in Case 2, just note that the smaller graph in this figure represents the first 0.003 s period that could not be clearly shown in the main graph. Within the first 0.003 s, the pressure drop increase occurred in all the three unit cells while water passed the inlet of the three cells. Pressure drop increase first occurred at Cell 1 and then Cell 2, with almost the same magnitude of 6 kPa. While such a large amount of water flowing through, air could be squeezed and the pressure at the inlet would increase significantly, this was also mentioned in Case 1. The pressure drop increase in Cell 3 occurred later, but with the largest magnitude of 25 kPa. This is because there is an end wall (x = 0.012 m) at the inlet of this cell. As the water hit this wall, the squeezing effect would become more significant thus increasing the pressure. By looking at the whole time period, it could also be observed that the pressure drop in Cell 3 was always greater than that in cells 1 and 2. This is similar to the result obtained in Case 1. The overall pressure drop decreased from the beginning because the water was initially flowing away from the air inlet.

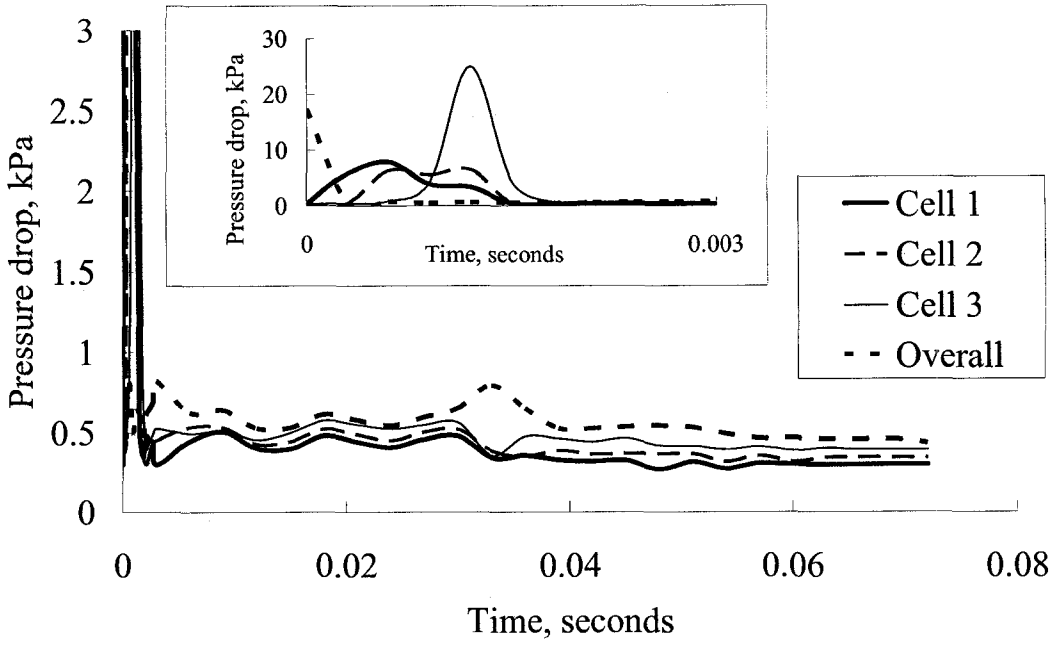

Fig. 25. Pressure drop along different volumes for Case 2.

By contrast, both Cases 1 and 2 showed that Cell 3 always had a larger pressure drop than Cells 1 and 2 (Figs. 19 and 25) and most of water moved into this cell (Figs. 17 and 22). Therefore, it could be concluded that Cell 3 is the most possible cell to have the largest amount of water in this kind of stack, regardless of where water was from in the inlet manifold. It was noticed that the water amount in the outlet manifold changed dramatically (Figs 17 and 22). This is because while water flowed into the outlet manifold, there would be some water flowing out of the manifold. However, in Case 2, it could be noticed that finally this curve remained at about 4%, as shown in Fig. 22, indicating that there was some water remained in the outlet manifold. As discussed before, this was because some water passed through Cell 1 in Case 2.

By comparing the flow behaviours in the first two cases, as mentioned before, it is difficult to have evenly distributed water among the three unit cells. In this kind of stack, the last cell (Cell 3) that is furthest away from the air inlet and connecting the end wall of the inlet manifold would always have the greatest pressure drop and the largest amount of water distribution from the inlet manifold. By investigating the velocity fields in the outlet manifold in both Case 1 and 2, it was found that the outgoing air streams from the three cells were blocking and squeezing the water in the outlet manifold. So water from Cell 3 would always be the easiest path for water to flow out from the stack, because this part of water would encounter the weakest resistance. Therefore, it could be concluded that, if the unit cell further away from the gas flow outlet had greater water distribution, then the water flowed out from this unit cell would be blocked by the air streams from the other unit cells. On the contrary, better water draining conditions could be achieved when the unit cell(s) closest to the gas flow outlet has (have) the largest water distribution, as in Cases 1 and 2.

4.3 Case 3: Water films with a thickness of 0.2 mm placed on the windward (left) side surface of each gas flow channel in the unit cells

In Case 3, the windward (left) side surface of each gas flow channel was covered with a water film with a thickness of 0.2 mm. These surfaces were assumed to be the electrode surfaces of the gas flow channels on the cathode side, on which water films could be formed by electro-chemical reactions and water vapour condensation during PEM fuel cell operations. Here the electro-chemical reaction was not considered while the water

film was used to simulate water production as stated in the Introduction section of this paper. The initial water distribution is shown in Fig. 11c for Case 3.

4.3.1 "Collecting-and-separating-effect" in serpentine gas flow channel

Fig. 26 shows how generally water was transported through the cell stack. At t = 0.0006 s, water in the gas flow channels was separated into different parts by the U-shaped corners (U-Turns). This is because the water approaching the U-turns would slow down and hit on the U-turn outside surface due to the inertia effect, but the water leaving the U-turn would resume its normal speed in the horizontal channel. Therefore, the water after the U-turns would move faster than the water coming to the U-turns. Thus that water was "separated" by the U-turn was explained. On the other hand, because the water coming to the U-turns moved slowly, this part of water would wait for the water leaving from its upstream U-turn. Therefore, at the U-turns of the serpentine gas flow channels, water was also "collected". Generally speaking, at the U-turns of the serpentine gas flow channels, water was collected and then separated into different parts. When the water films were separated into small droplets, it would be much easier to remove them. Therefore the serpentine design actually can facilitate the water removal by using its "collecting-and-separating-effect". This is just like the military strategy "divide and conquer". In Fig. 27, at t = 0.0006 s, it could be noticed that the velocity fields and water distribution were almost the same on the near-wall surfaces of the three unit cells (water in Cell 3 moved a little bit faster). Therefore, it could be expected that water in the three unit cells would have similar transportation characteristics. This could be appreciated with the help of Fig. 28, which shows the water amount variation along different unit cells and manifolds. In

particular this case (Case 3), since a relatively large amount of water was considered as evenly distributed in the gas flow channels, the water in the inlet manifold would always be maintained at zero. As shown in Fig. 28, water in the three unit cells had the same amount of initial water distribution, and moved into the outlet manifold within almost the same time period (Cell 3 was slightly faster), it could also be noticed that the curve representing the water amount in the three unit cells decreased step by step, which is similar as in Figs. 18, 23 and 29. The reason is as we mentioned, water was separated into several parts by the U-turns. Fig. 29 shows the overall water amount inside cathode (stack), the curve decreased step by step as in Figs. 18 and 23. Fig. 29 also showed that water started moving out of the stack at about 0.015 s.

At t = 0.04 s, as shown in Fig. 28, water in the three unit cells was already flown away, and the three curves maintained at almost zero. Even though the difference was not significant, the results showed that Cell 3 had a better water draining ability than Cells 1 and 2. At a later time, as shown in Fig. 26b, water was not just maintained on the windward wall of the unit cells, most of the water moved onto the bottom surfaces and even the leeward surfaces. It is not easy to ascertain to which surface water would adhere in such a long time period; this depends on different factors such as shape of the flow channels, airflow velocity, among others. The outlet manifold still had excessive water left which was about 5%, as shown in Figs. 26d and 28. This is because some of the water from Cell 1 was squeezed onto the end wall of the outlet manifold. The same phenomenon was shown in Case 2 (Figs. 21d and 22).

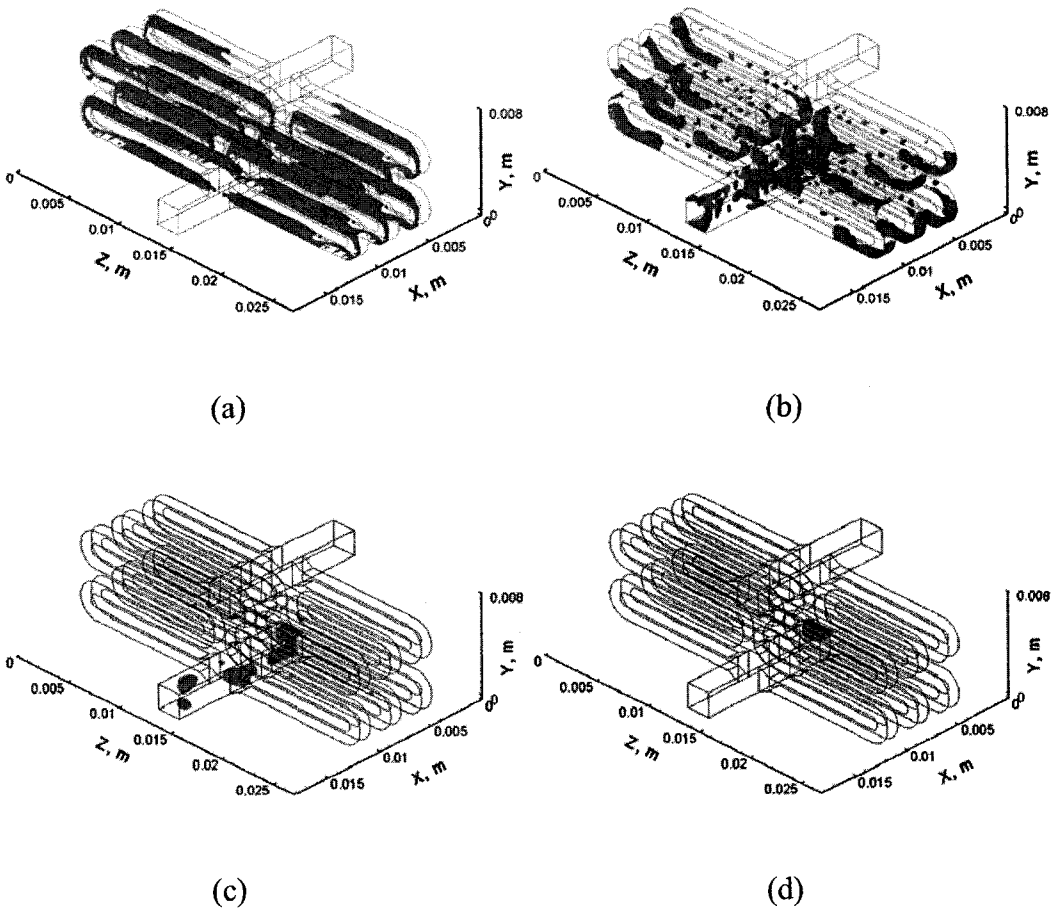

Fig. 26. Water movement in 3-D view for Case 3.

(a: t = 0.0006 s; b: t = 0.003 s; c: t = 0.039 s; d: t = 0.075 s)

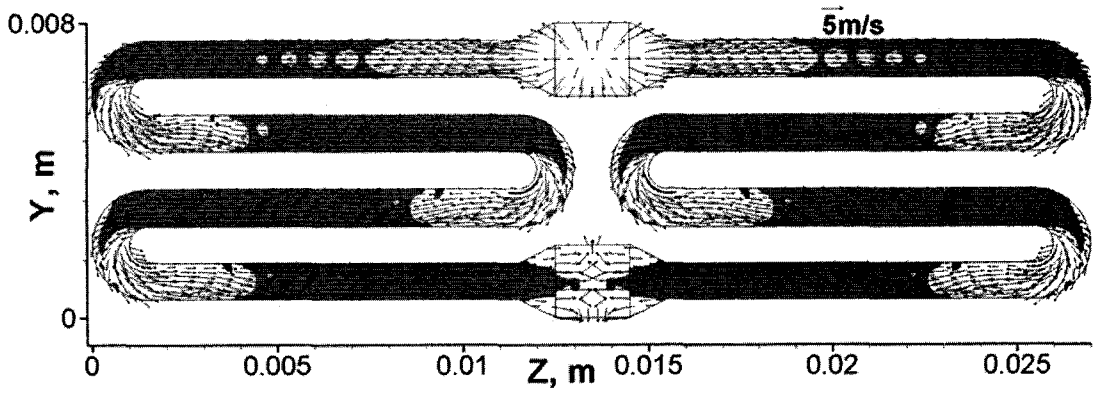

(a)

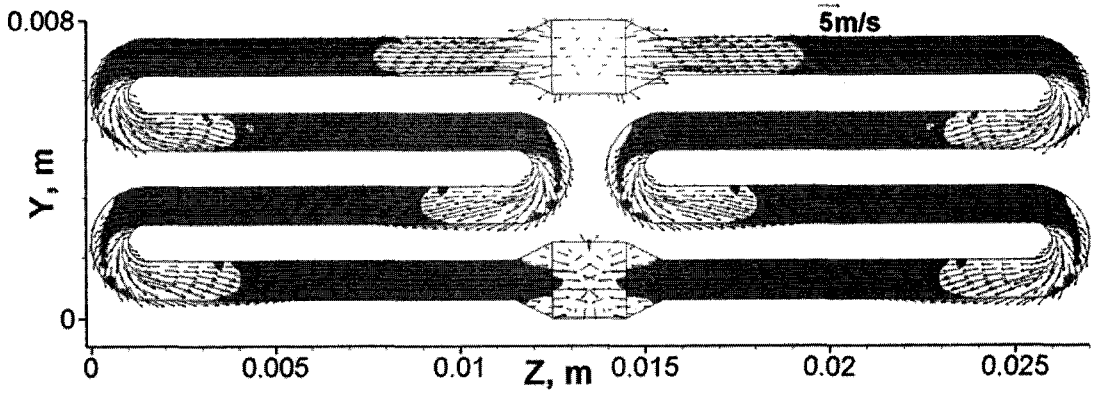

(b)

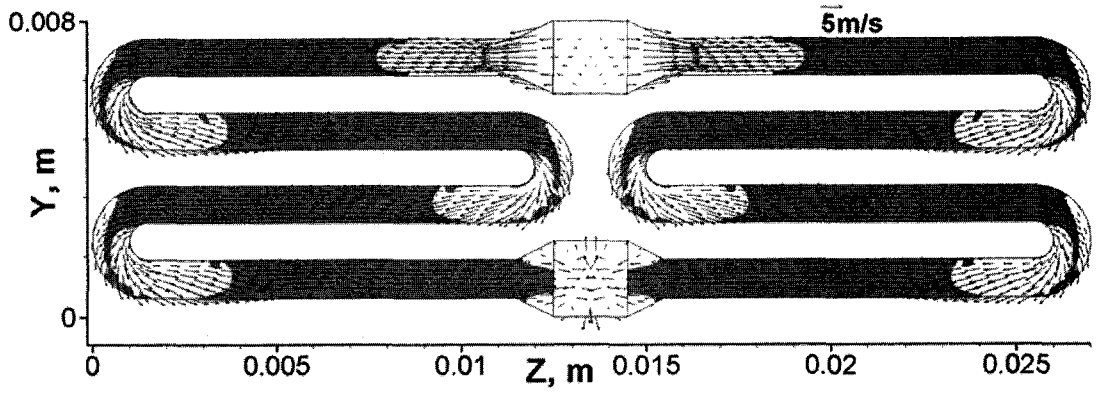

(c)

Fig. 27. Water on the near-wall surfaces at t = 0.0006 s for Case 3.

(a: x = 0.012 m; b: x = 0.009 m; c: x = 0.006 m)

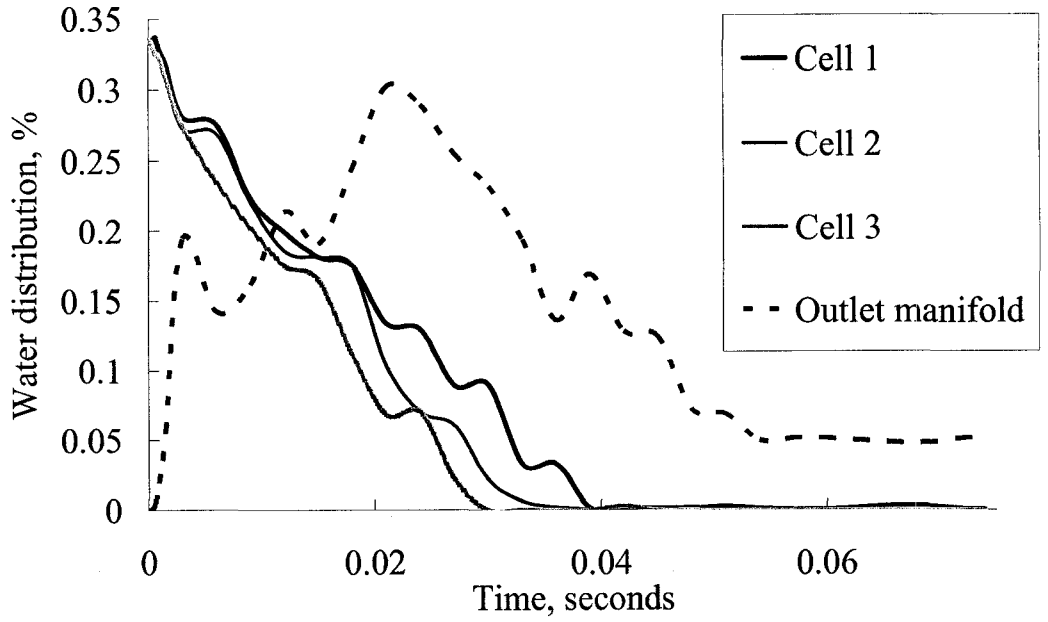

Fig. 28. Water amount variation in different cells and manifolds for Case 3.

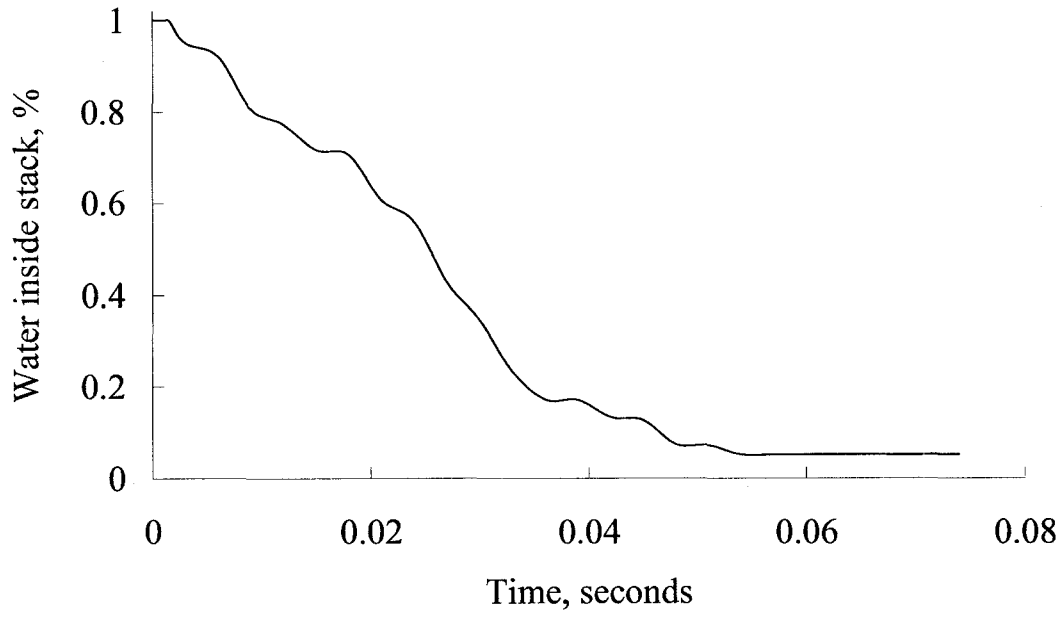

Fig. 29. Water amount inside stack versus time for Case 3.

4.3.2 Change of pressure drop when the outlet manifold blocked with water

The pressure drop in different volumes for this case is shown in Fig. 30. Different from Case 2, the pressure drop decreased in all the three unit cells within the first 0.003 s. This is because as the water flowed into the outlet manifold, the increasing amount of water in the outlet manifold would block the outlet of each unit cell, the pressure in the outlet manifold and the outlets of the unit cells could become very high. Therefore, the pressure drop along the unit cells decreased. The pressure drop decreased first in Cell 3, then Cells 2 and 1. In Cell 3, the pressure drop only decreased by about 0.4 kPa, and only for a little while, this is because Cell 3 is easier for the water coming out from it to flow into the outlet manifold (as was concluded in Case 2). But later, the pressure drop decreased more in Cells 1 and 2, by about 1 kPa, this is because water flowed out from these two cells could be blocked by the outgoing air streams from Cell 3, and the end wall (x = 0.005 m) of the outlet manifold was connecting to Cell 1, then due to the effect of wall adhesion, water coming out from Cell 1 could be more difficult to move out of the stack. Therefore, more water could stay in the outlet manifold at the outlets of Cells 1 and 2, and the pressure here could become very high. This explained why the pressure drop decreased severely in Cells 1 and 2. At about 0.0022 s, in Fig. 30, while the pressure drop in Cells 1 and 2 decreased, it could be observed that the pressure drop in Cell 3 increased simultaneously. Recalling from Equation (11), we know that the flow rate or velocity is the main factor that affects the pressure drop. Therefore, while air had difficulty to flow through some gas flow channels (Cells 1 and 2), more air would flow through the other cells (Cell 3), thus decreasing the pressure drop along Cells 1 and 2 and increasing the pressure drop along Cell 3. The overall pressure drop also increased during this time

period, because with the unit cells blocked, the pressure in the inlet manifold would be increased, thus increasing the overall pressure drop. At a later time, by looking at the overall time period, it could be observed that the pressure drop changed dramatically, but the pressure drop in the three unit cells never decreased or increased together. This is because when some unit cells have less air flowed in (the pressure drop would decrease), other unit cells would always have a much higher flow rate (the pressure drop would increase) to maintain the mass conservation. This could be observed in Fig. 30. Generally, by looking at the overall pressure drop in Fig. 30, it could be observed that Cell 3 still had a greater pressure drop than the others, and after 0.05 s, as all the water flowed out of the cells, the pressure drop in the three unit cells remained constant and Cell 3 still had its greatest magnitude.

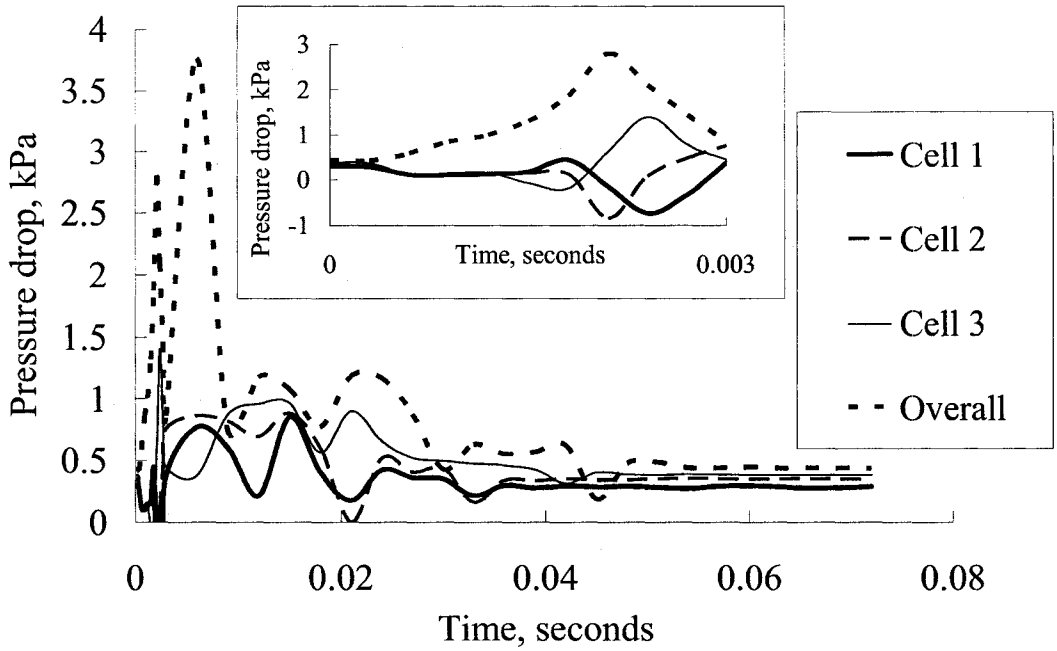

Fig. 30. Pressure drop along different volumes for Case 3.

4.4 Case 4: Water films with a thickness of 0.2 mm placed on the leeward (right) side surface of each gas flow channel in the unit cells

In Case 4 was simulated to compare with Case 3. In this case, the MEA side was assumed to be windward (on the left hand side), as shown in Fig. 11d. Therefore, the water films formed due to electro-chemical reactions would be assumed on this side.

4.4.1 Comparison of water flow behaviours in Cases 3 and 4

Similar to Case 3, water was initially broken up at the U-turn, as shown in Figs. 31 and 32. The "collecting-and-separating-effect" could also be noticed. As time passes, water in the gas flow channels moved to other surfaces, this is also similar to Case 3. Also as shown in Fig. 32, the water distribution and velocity fields were almost the same on the leeward surfaces for the three unit cells. After water moved away, it could be noticed that

there was some water remained on the end wall of the outlet manifold; this was shown in Cases 2 and 3 too. Therefore, the authors concluded that, once there is water flowing through the gas flow channels closest to the end of wall (the wall facing and furthest away from the air flow outlet), it is unavoidable to have some water adhering to this wall.

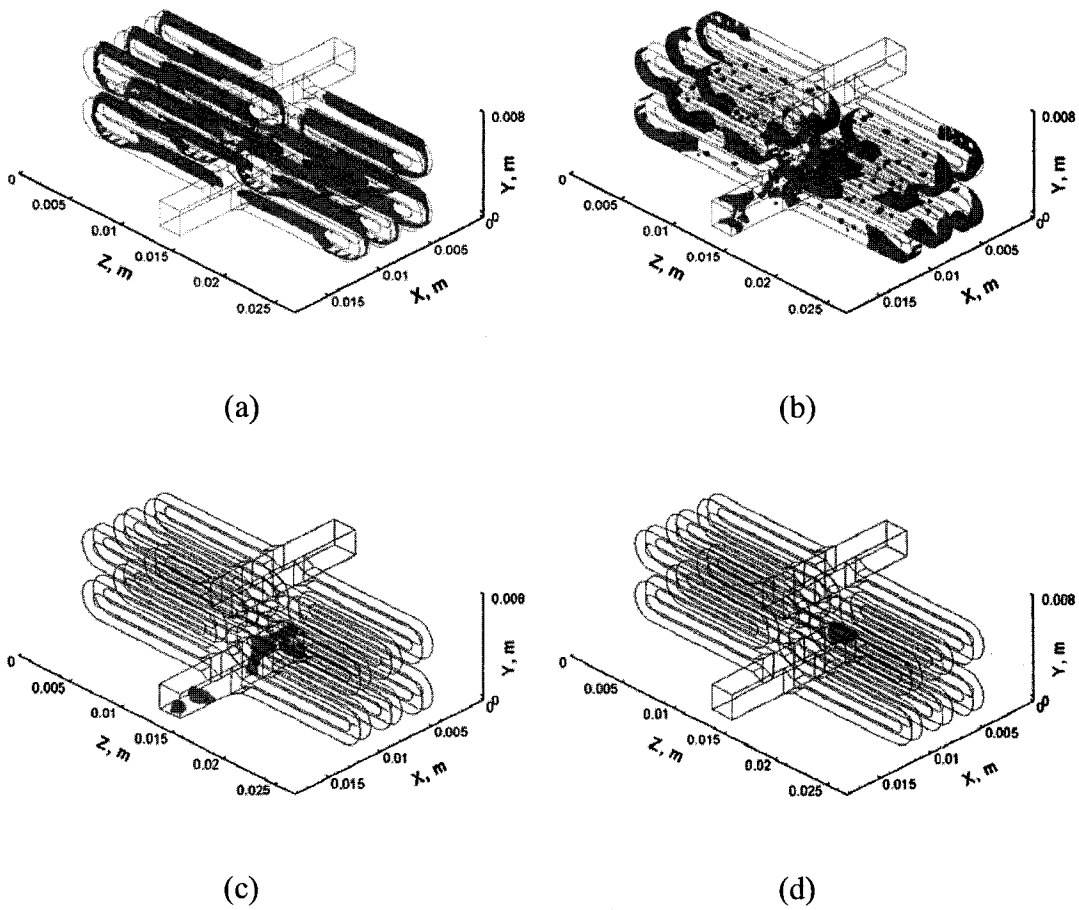

(a) (b)

(c) (d)

Fig. 31. Water movement in 3-D view for Case 4.

(a: t = 0.0006 s; b: t = 0.003 s; c: t = 0.048 s; d: t = 0.075 s)

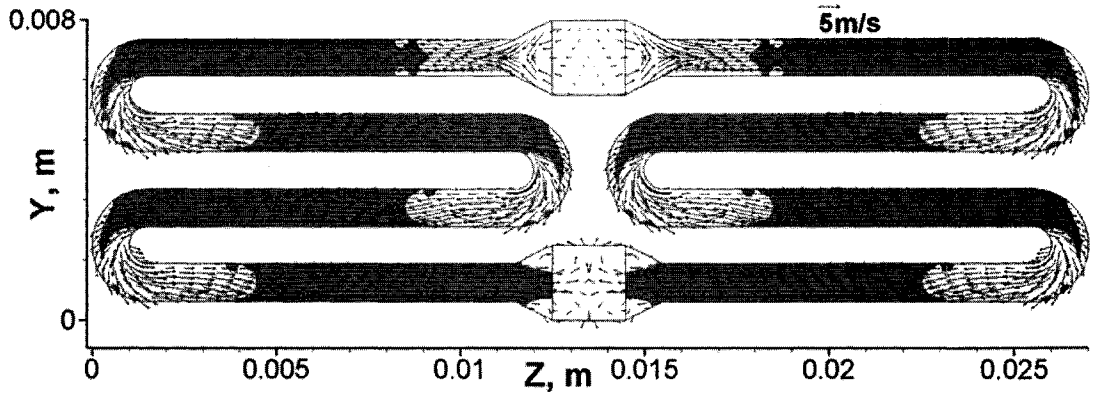

(a)

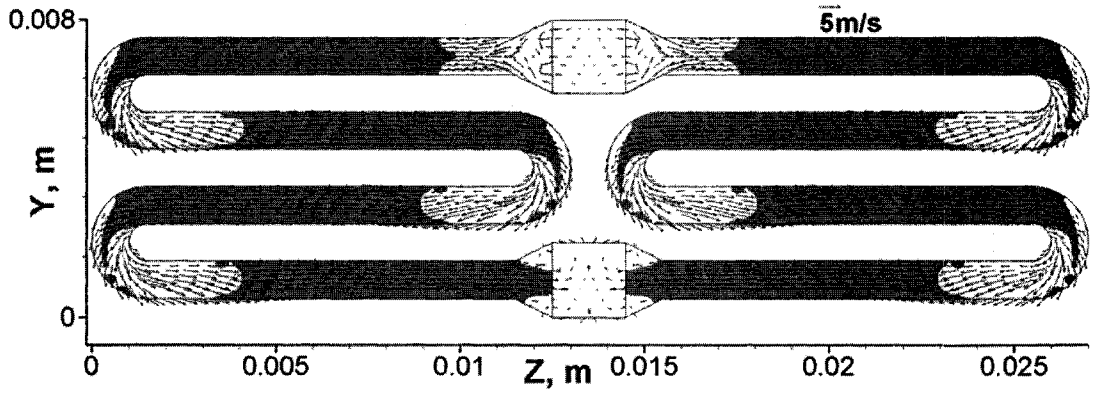

(b)

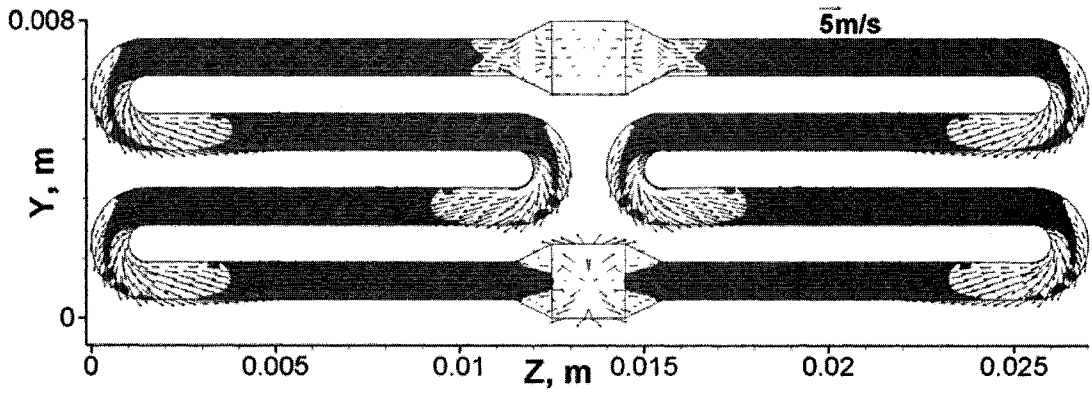

(c)

Fig. 32. Water on the near-wall surfaces at t = 0.0006 s for Case 4.

(a: x = 0.011 m; b: x = 0.008 m; c: x = 0.005 m)

Fig. 33 shows the water distribution along different volumes; this figure is very similar to Fig. 28. But in this case, it took a time period of 0.06 s to have all the water flow out of the gas flow channels; longer than that in Case 3 which was about 0.05 s. Also if we look at the overall water amount inside cathode (stack) for Case 4, as shown in Fig. 34, no significantly difference could be found by comparing to Fig. 29, both curves decreased step by step, the water flow behaviours were very similar between Cases 3 and 4, the only difference is that Case 3 had faster water drainage. The difference between Cases 3 and 4 is the initial water film arrangement; in Case 3 the water films were placed on the surfaces closer to the air outlet while in Case 4 they were placed further. Better water draining was achieved by placing the water films closer to the air outlet (as in Case 3), thus it could be concluded that arranging the MEA side of the unit cells closer to the gas flow outlet could obtain a better water draining process.

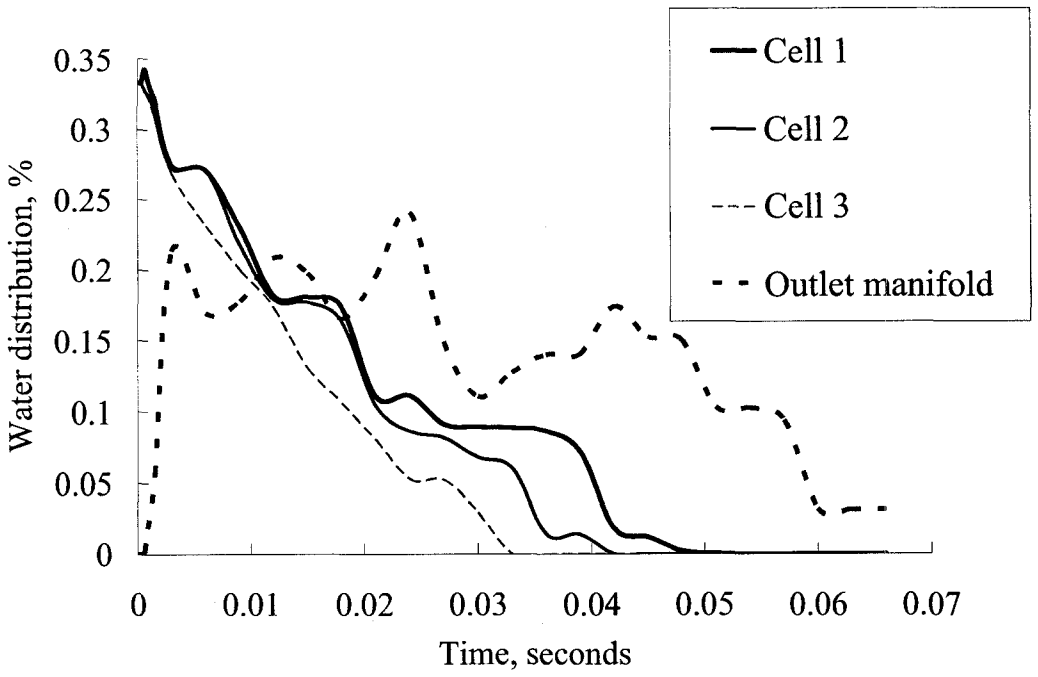

Fig. 33. Water amount variation in different cells and manifolds for Case 4.

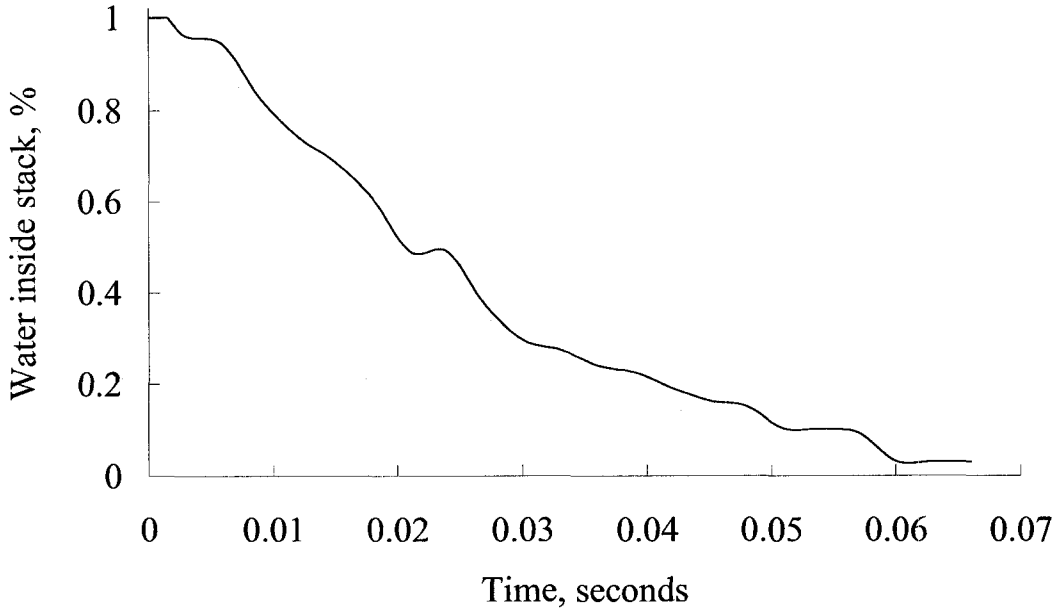

Fig. 34. Water amount inside stack versus time for Case 4.

4.4.2 Comparison of pressure drop in Cases 3 and 4

As shown in Fig. 35, the pressure drop in different volumes is also similar to Case 3, as shown in Fig. 30. In both figures, the pressure drop along the three unit cells never decreased or increased at the same instant, as we mentioned earlier, this is because once some cells had lower flow rate (pressure drop would decrease), other cells would have higher flow rate (pressure drop would increase). But Cases 3 and 4 approved that the pressure drop along different unit cells in this kind of cell stack is very sensitive, especially with different water distribution in each cell. Once one unit cell had a lower flow rate, the pressure drop along this cell would decrease, on the other hand, as the pressure drop decreased, the other cells' pressure drop would increase due to a higher flow rate, this is the problem that is hard to be avoided in this kind of parallel gas flow channels.

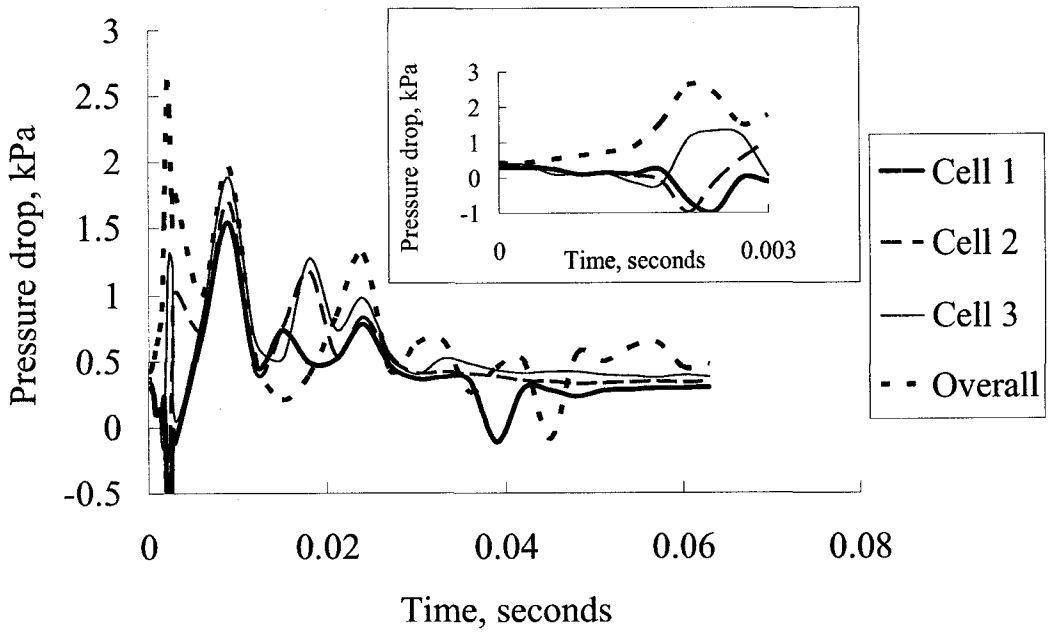

Fig. 35. Pressure drop along different volumes for Case 4.

CHAPTER 5

ANALYSIS OF RESULTS – TOPIC 2

5.1 Case 1: Water films with a thickness of 0.2 mm placed on the leeward (right) side surface of each gas flow channel in the unit cells

In Case 1, the leeward (right) side surface of each gas flow channel was covered with a water film that has a thickness of 0.2 mm. These surfaces were assumed to be the electrode surfaces of the gas flow channels on the cathode side, on which water films could be formed by chemical reactions and condensation during PEM fuel cell operations. Here the electro-chemical reaction is not considered while the water film is used to simulate the water production. The initial water distribution is shown in Fig. 12a. The ability of water draining was tested, and the velocity field affected by the water distribution was studied.

Water was initially evenly distributed in every gas flow channel. As shown in Fig. 36, in the long run, water started to descend due to the effects of gravity and the dragging force. The amount of water in each gas flow channel was the same, and the airflow rate was evenly distributed. Therefore, water descended with almost the same velocity and flow behaviour and at t = 0.003 s, all the water in every gas flow channel had been drained into the outflow manifold. Fig. 37 shows the velocity field and water distribution on different planes of the z-direction. At t = 0.003 s, all of the water had moved into the outflow manifold, and there was no water left in the gas flow channels. The velocity field in every gas flow channel was almost the same. At the exits of the gas flow channels, airflow was directed downward (along the negative y-direction) and strong air streams were formed. As mentioned earlier, these strong air streams would block air and water from the left

side (the other side of the gas flow outlet of manifold) and were also reflected by the bottom surface of the outflow manifold. Therefore, between every two air streams from the gas flow channels, there would be a velocity field formed directed upward (along the positive y-direction).

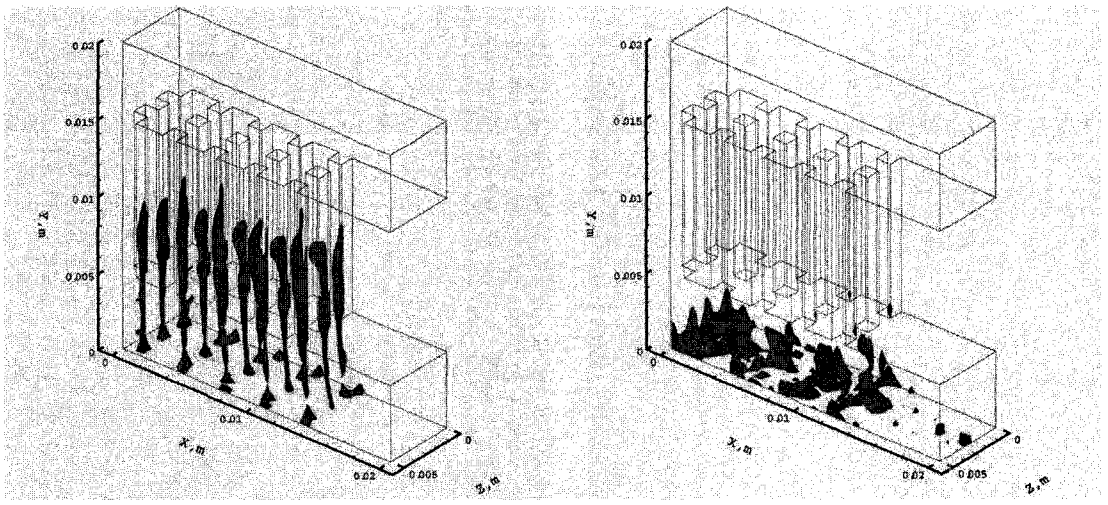

(a) (b)

Fig. 36. 3-D view of water distribution (a: t = 0.0015 s; b: t = 0.003 s).

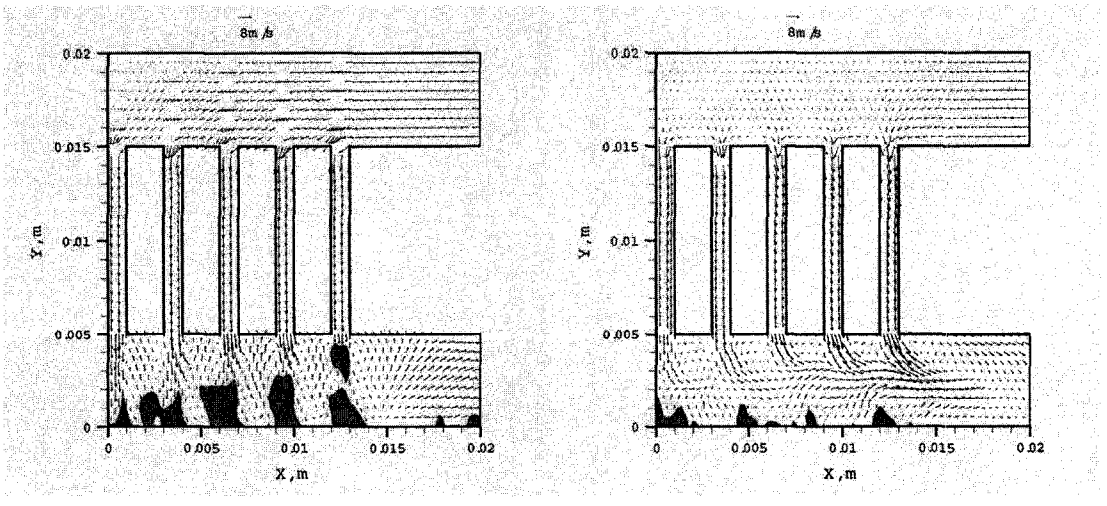

(a) (b)

Fig. 37. Water distribution and velocity field in different planes.

(a: t = 0.003 s, on the center-plane of the z-direction (z = 2.5 mm); b: t = 0.003 s, on the plane close to z = 0)

Fig. 38 gives a different view at t = 0.003 s. In the outflow manifold, on the plane crossing the center of the far left unit cell, as shown in Fig. 38a, airflow was directed downward with a relatively higher velocity. But at the sections between two downward flow streams, as shown in Figs. 38b and 38c, air and water were flowing upward with a relatively lower velocity. The air and water were squeezed into those sections by the two strong air streams on either side and since there were two high velocity fields formed on both sides of this section, it was difficult for the air and water to flow out and the path with lowest resistance was upward. Fig. 39 shows that at a later time, on the plane close to the surface at x = 0, water was squeezed and forced to ascend into the gas flow channels, as shown in Figs. 39b and 39c. Clearly, this indicates a severe problem because the gas flow channels were blocked again. The reason that this kind of flow phenomenon occurred was because the air streams from the gas flow channels were very strong. Water descended from every channel surface at the same time and thus the air streams passing through the gas flow channels met insignificant resistive forces. Fig. 40 shows a plane just between the two far left cells, at x = 2 mm. In time, water was pushed upward by a double vortex. Once the water reached the top surface of the outflow manifold (at y = 0.005 m), it remained on that surface and eventually moved into gas flow channels.

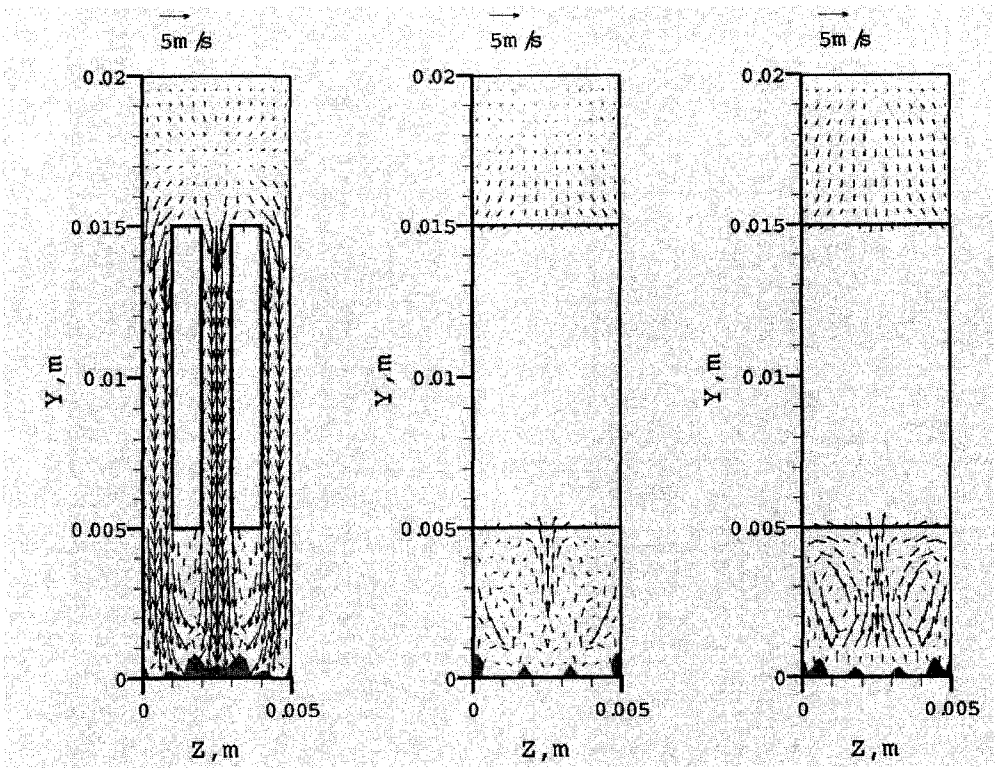

(a) (b) (c)

Fig. 38. Water distribution and velocity field on different planes.

(a: t = 0.003 s, on the center-plane crossing the far left cell (x = 0.5 mm); b: t = 0.003 s, on the plane at x = 1.5 mm; c: t = 0.003 s, on the plane at x = 5 mm)

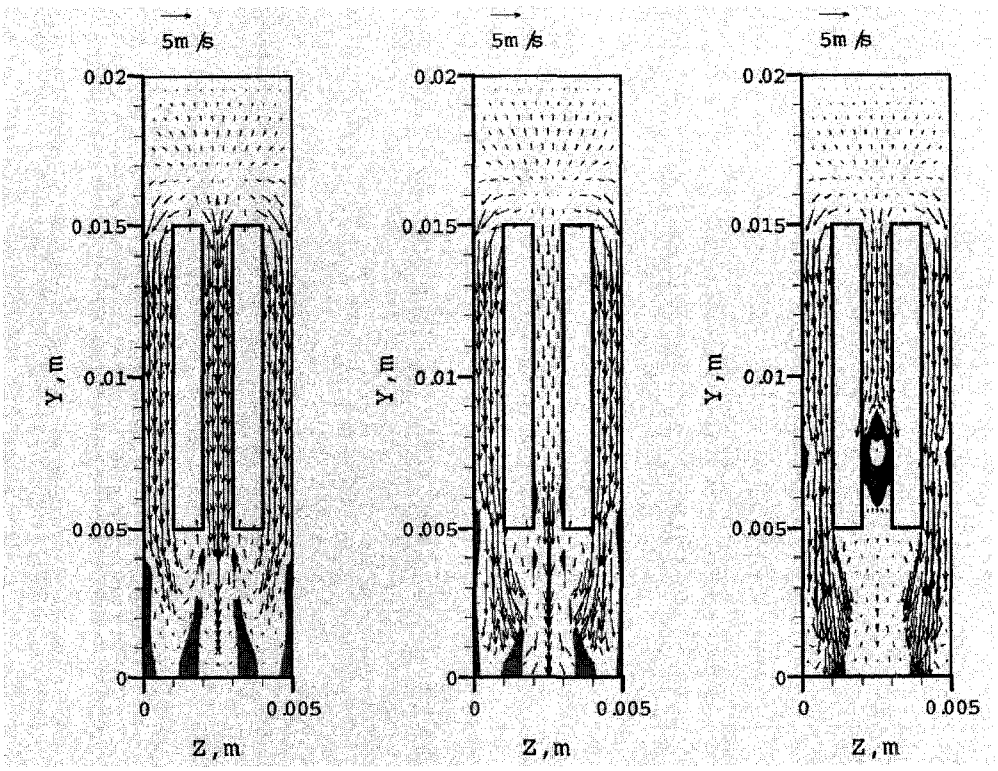

(a) (b) (c)

Fig. 39. Water distribution and velocity field on the plane close to x = 0.

(a: t = 0.0045 s; b: t = 0.006 s; c: t = 0.009 s)

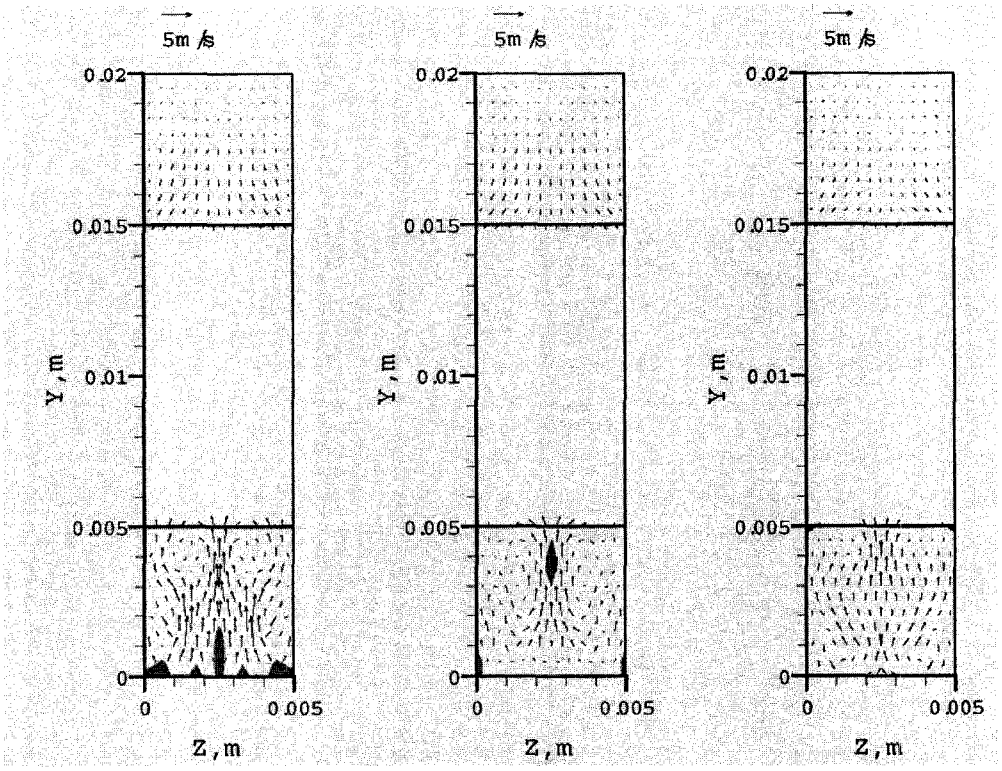

(a) (b) (c)

Fig. 40. Water distribution and velocity field on the plane at x = 2 mm.

(a: t = 0.003 s; b: t = 0.0045 s; c: t = 0.009 s)

As shown in Fig. 41, at t = 0.0024 s, the right sides of the gas flow channels were blocked by water films, and the air streams flowing out of these gas flow channels were reflected by the water films. Therefore, these reflected air streams descended and moved to the left (along the negative y-and x-directions), as shown. After these air streams flowed into the outflow manifold, they were reflected again by hitting the bottom surface and thus ascended and moved to the left (along the positive y-and negative x-directions). In this kind of condition, water was moved further away from the gas flow outlet. This is why some water stuck to the surface at x = 0 and ascended, as shown in Fig. 39. But this kind

of flow pattern did not last long and at t = 0.003 s, all the water films were pushed away from the gas flow channels. The air streams from the gas flow channels would no longer be reflected to flow along the negative x-direction. However, there was already some water moved to the left side (along the negative x-direction), especially for the water from the two left cells. After t = 0.003 s, the water which was initially pushed to the left side (along the negative x-direction) would keep ascending and get into the two far left cells, explaining why the two left cells were blocked with water. As the velocity field in the outflow manifold got closer to the gas flow outlet of the manifold, a larger exiting velocity could be observed in Figs. 41c and 41d. At a closer location to the gas flow outlet, there would be less air streams that resist air and water flowing out. For instance, for the far right cell, there were no air streams which stopped this cell's outgoing air streams from flowing out of the outflow manifold. But the outgoing air and water from the cell second to the right would be blocked by the far right cell's air streams. Generally, the further from the gas flow outlet of the manifold, the greater number of air streams that would block air and water flowing out. This is a common problem that is inevitable for parallel flow channels; however it could be remedied by modifying the shape of gas flow channels and manifolds. After a while, water ascended to the middle height of the gas flow channels (about y = 0.01 m), and after that, it could no longer keep moving upward, as shown in Fig. 41d. So that water will descend into the outflow manifold again.

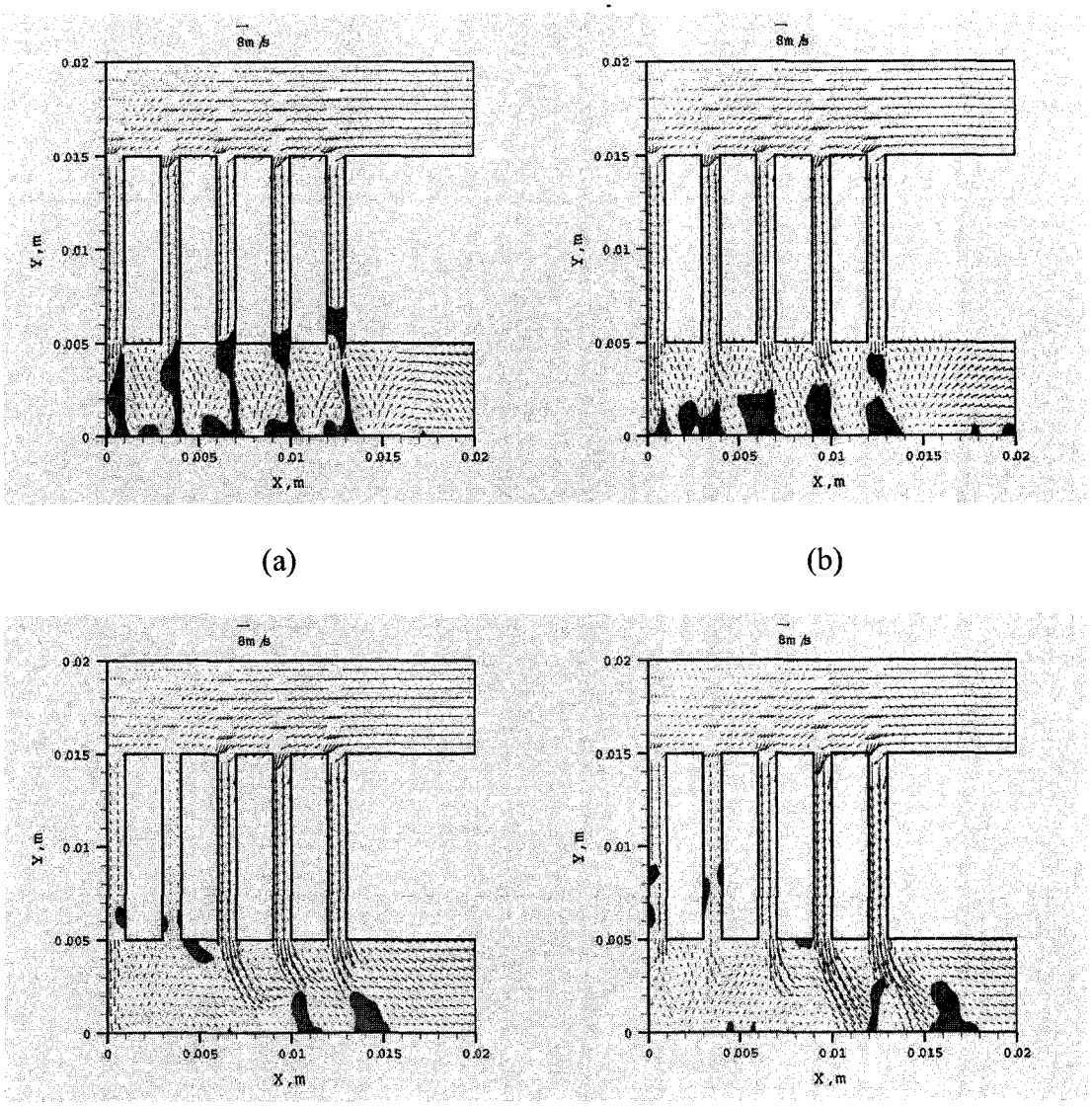

Fig. 41. Water distribution and velocity field on the center-plane of the z-direction (z = 2.5 mm).

(a: t = 0.0024 s; b: t = 0.003 s; c: t = 0.006 s; d: t = 0.009 s)

5.2 Case 2: Water films with a thickness of 0.2 mm placed on the windward (left) side surface of each gas flow channel in the unit cells

Case 2 was simulated to compare with Case 1. In this case, the MEA side was assumed to be windward (on the left hand side). Therefore, the water films formed due to chemical reactions would also be assumed on this side and the initial water distribution is shown in Fig. 12b.

Similar to Case 1, as shown in Fig. 42, all of the water films descended into the outflow manifold at the same time. In contrast to Case 1, the air streams from the gas flow channels were reflected another way: downward, but towards the gas flow outlet. This is because the water films in this case were on the other side. These air streams would be reflected again at the bottom surface of the outflow manifold, to ascend and flow out (along the positive y-and x-directions). Therefore, water in the outflow manifold was moved toward the gas flow outlet. This is the major difference between Cases 1 and 2. The water flown away by the two different reflected air streams would block different gas flow channels.

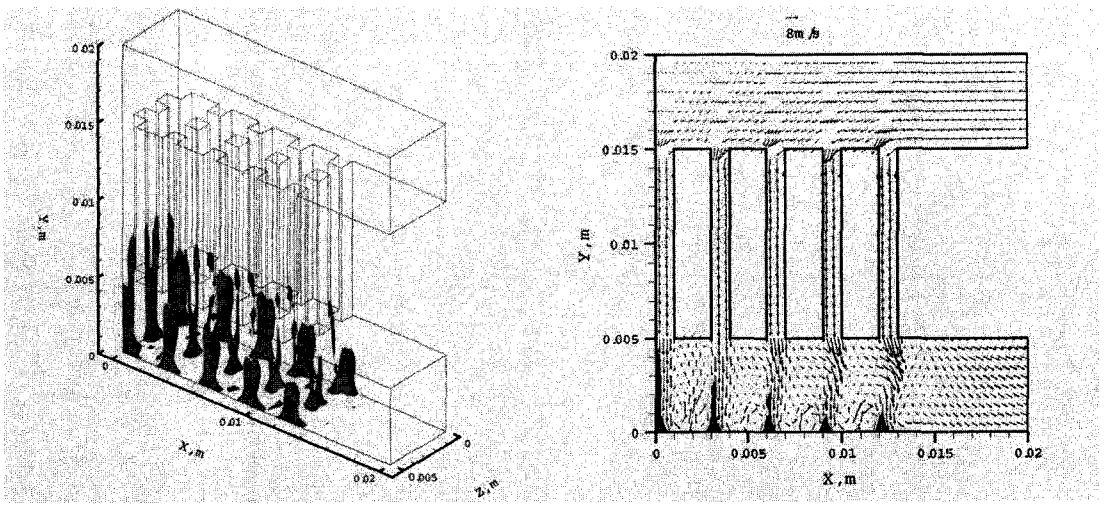

(a) (b)

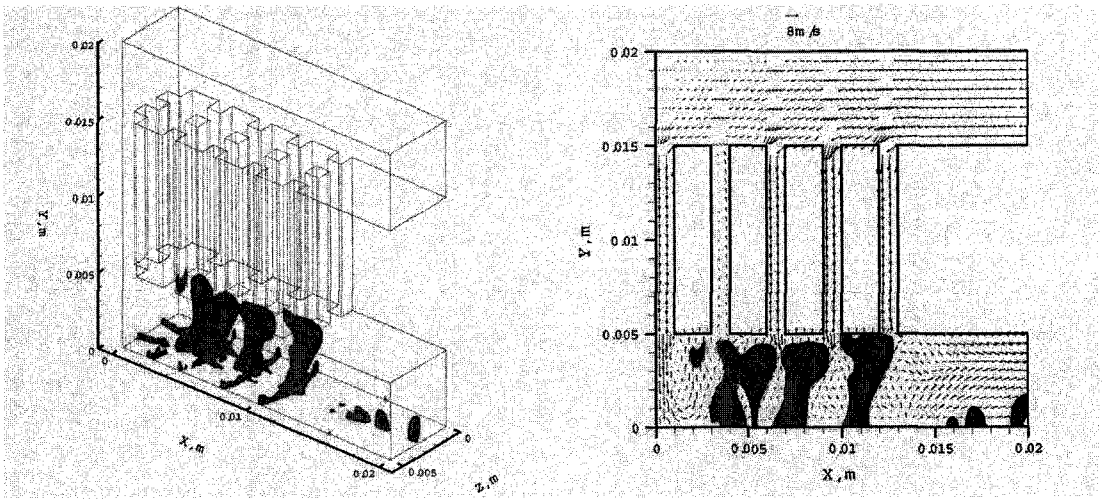

(c) (d)

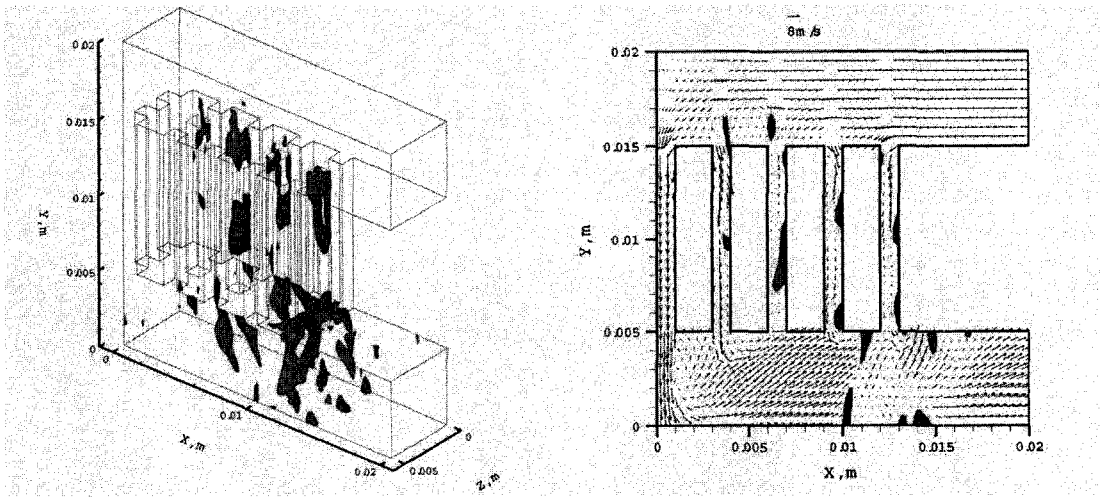

(e) (f)

Fig. 42. Water distribution and velocity field in 3-D view and on the center-plane of the z-direction.

(a: t = 0.0015 s, in 3-D view; b: t = 0.0015 s, on the center-plane of the z-direction (z = 2.5 mm); c: t = 0.003 s, in 3-D view; d: t = 0.003 s, on the center-plane of the z-direction (z = 2.5 mm); e: t = 0.009 s, in 3-D view; f: t = 0.009 s, on the center-plane of the z-direction (z = 2.5 mm))

Eventually, water started to ascend from the bottom surface of the outflow manifold. As mentioned earlier, water was initially slightly pushed to the gas flow outlet hence when the water moved upward, the cells on the right side would be blocked and it would keep ascending in the gas flow channels. At t = 0.009 s, as shown in Figs. 42e and 42f, some water even moved into the inlet manifold. The reason why the water moved higher in the gas flow channels than in Case 1 was because there were some reflected air streams that facilitated the water to flow upward. This could be explained with the help of Fig. 42f which shows that all the four right cells were blocked with water, and thus most of the air was flowing through the far left cell. As a result, very strong air stream was flowing out of the far left gas flow channel and was also reflected by the bottom surface of the outflow manifold. Therefore, there was a velocity field flowing up under the four right side cells which helped the water in the gas flow channels to keep ascending. But in Case 1, as earlier mentioned, the two left cells were blocked with water and most of the air was passing through the right side cells, and these air streams were also reflected by the bottom surface of the outflow manifold. Nevertheless, they were reflected to flow out of

the manifold, and thus would not facilitate the ascent of water in the two left cells. This phenomenon is shown in Fig. 41, and this is why the water flowed much higher than in Case 1.

It took a longer time for all the water to be drained in Case 2 than Case 1. Also in Case 2, water even moved into the inlet manifold, thus delaying the water draining process. Clearly, it is not a good phenomenon because the gas flow channels were blocked severely. Water in Case 1 only blocked 2 cells, and its ascent was not much. Therefore, positioning the MEA side of the fuel cell close to the gas flow outlet would greatly improve fuel cell performance. This is the same as mentioned in Topic 1 (Chapter 4). But Case 1 was still not a suitable condition for proper and efficient fuel cell operation; this is because the water still moved upward into the gas flow channels. One way to avoid this kind of problem is to optimize the shape of the flow channels and manifolds. In both Cases 1 and 2, water was flown up by reflected air streams from the gas flow channels. Remedying these air stream reflection effects is the key to fixing this kind of problem. The easiest way to solve it is simply to make the outflow manifold higher (expand the outflow manifold along the y-direction). With a larger outflow manifold, air streams from the gas flow channels would have more space to move in. This would greatly remedy the reflection effects, thus solving the upward flowing water problem.

CHAPTER 6

ANALYSIS OF RESULTS – TOPIC 3

6.1 Case 1: Water films with a thickness of 0.03 mm placed on membrane/catalyst layer for computation domain 1

The first case was simulated to investigate the effects of the GDLs with cubic micro-structures (Fig. 6b) on liquid water flow behaviour. As shown in Fig. 13, water films with a thickness of 0.03 mm were placed on membrane/catalyst layer in computation domain 1 (Fig. 6b). The rupture of water films, change of water occupation fraction in the MEA, and water transport inside the MEA were studied.

6.1.1 Rupture of water films

Fig. 43 shows the rupture of the initially attached water films while Fig. 44 depicts the water distribution and velocity field on the center-plane of the catalyst layer. The rupture of the water films started from the corner, as shown from Figs. 43b and 44b. One of the main reasons for the water film to rupture from the corner could be attributed to the strong secondary flows formed at that location. The flow field along the other two directions (the cross section of the main flow direction) became stronger thus breaking up the balance between the air flow and the water films. Detailed descriptions of this kind of flow phenomena were discussed in previous sections. By comparing Figs. 45 to 48, the enhancement of the secondary flow could also be observed. In the cross sections close to the serpentine corner (Figs. 45 and 46, x = 0.00205 m), the secondary flow is much stronger than at the cross sections further away from the corner (Figs. 47 and 48, x = 0.01105 m). Because of the formation of the ruptured areas, some of the porous holes at the corner were not facing the water films. This leads to a decrease in the flow resistance

at those holes facing the ruptured areas and subsequently breaking up the balance between air and water from these sections. As a result, more air could flow through these holes into the catalyst layer., The velocity at the corner, therefore, increased and the air started flowing from the emptied sections to both of the straight sections at the inlet and outlet, as observed from Fig. 44b, at t = 0.0005 s. As shown in Figs. 49 and 50, water distribution and velocity field on the center-plane in both of the inlet and outlet sections at the serpentine corner could be observed (please note that the vertical lines in the gas flow channel and the catalyst layer at x = 0.002 m do not represent walls, these lines only represent the joints of the serpentine sections and the straight sections, they are all interiors). As shown in Fig. 49a, for the inlet straight section at t = 0.0001 s, the initially attached flat water films were in wave-form, especially in the corner. Then, at t = 0.0002 s (Fig. 49b), the first rupture was formed at the corner. It could be noticed that the main flow in the catalyst layer is along the positive x-direction while it is along the negative x-direction in the flow channel. The air was taking the water from the ruptured areas towards the straight section, and the effects of the main flow direction in the gas flow channel were insignificant. A similar condition could be observed in Figs. 50a and 50b. Ruptured areas formed and water started flowing towards the straight section but along the same direction as the main flow in the flow channel. However, this is not due to the effect of the main flow, as mentioned.

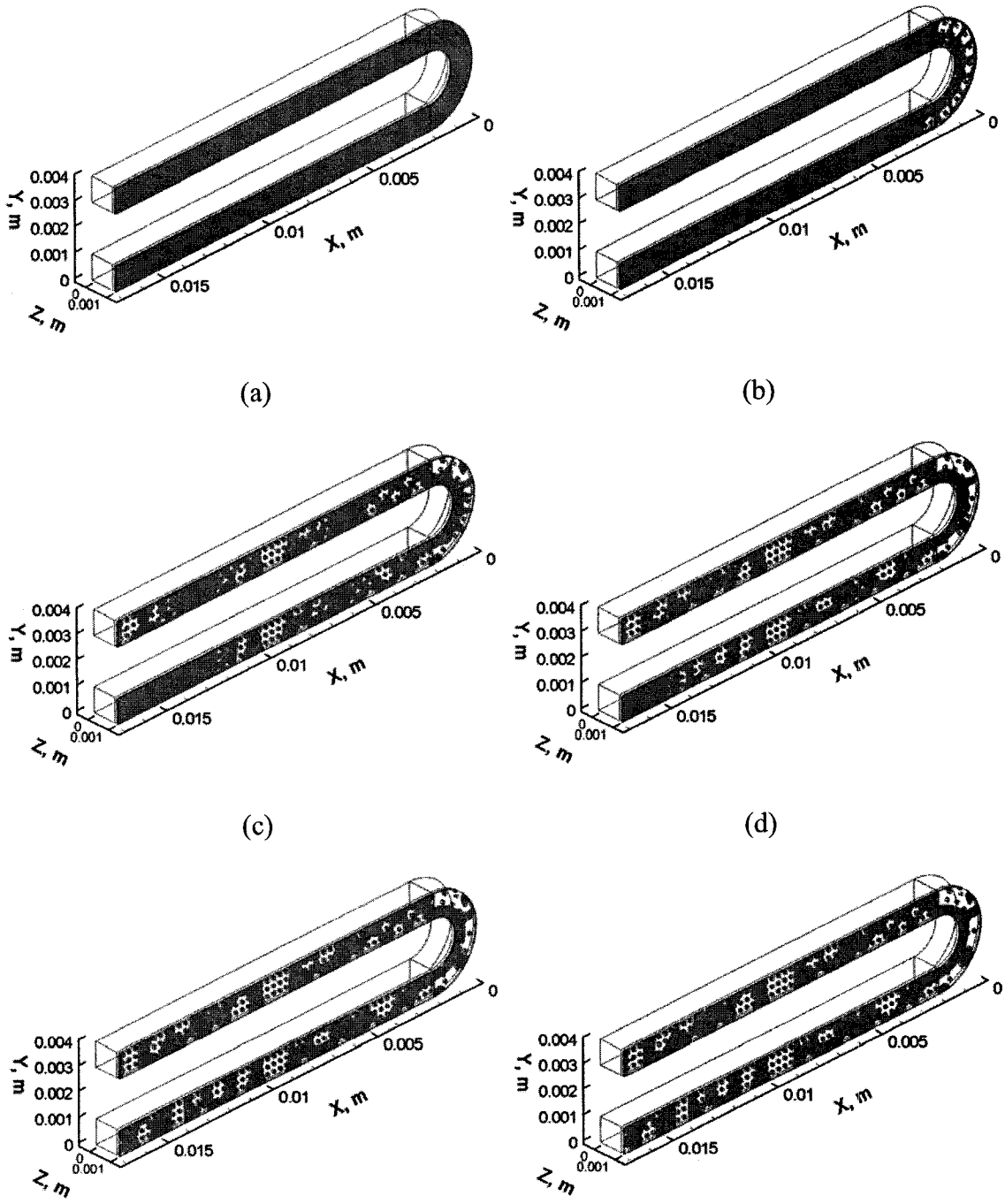

Fig. 43. Rupture of water films in 3-D view for Case 1.

(a: t = 0 s; b: t = 0.0005 s; c: t = 0.003 s; d: t = 0.005 s; e: t = 0.007s; f: t = 0.02 s)

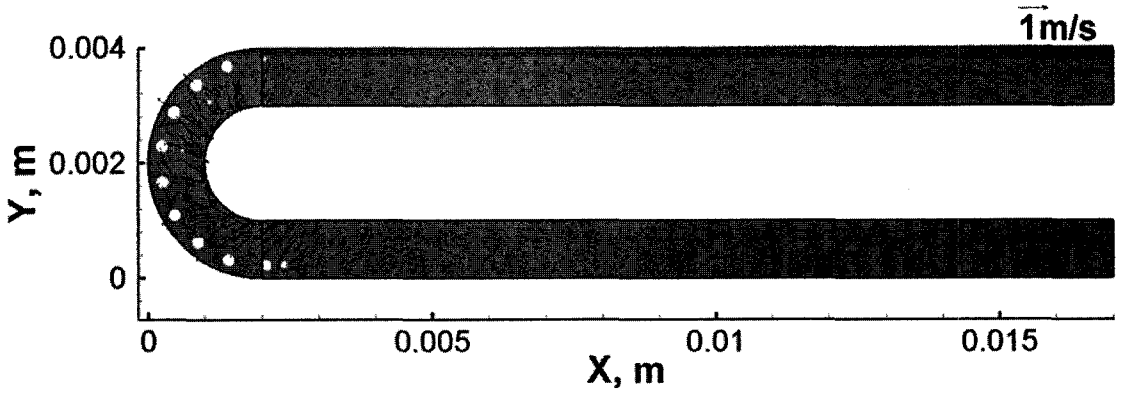

(a)

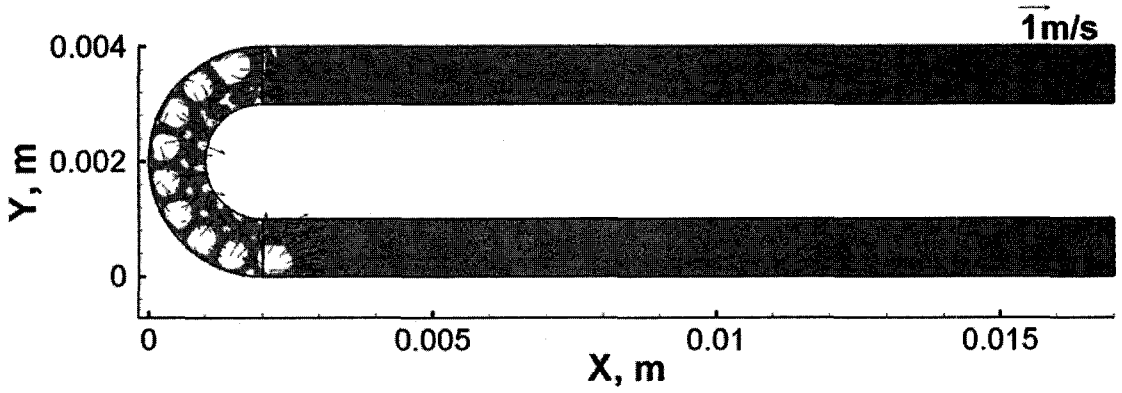

(b)

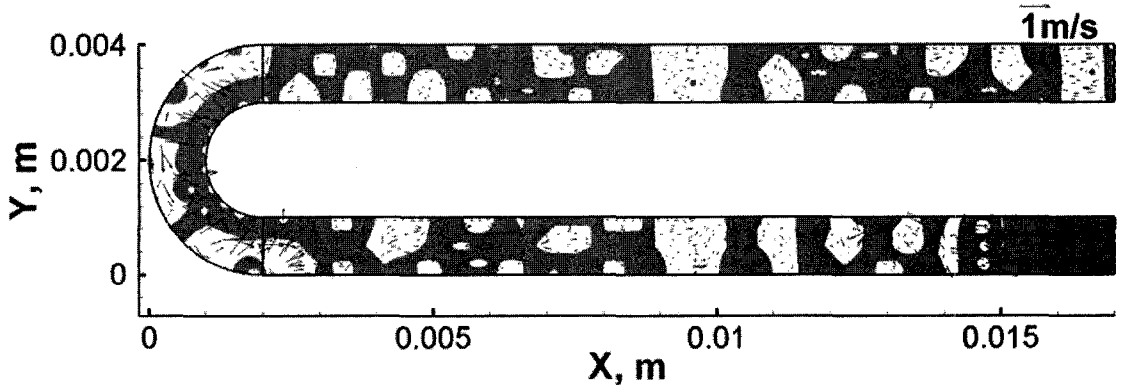

(c)

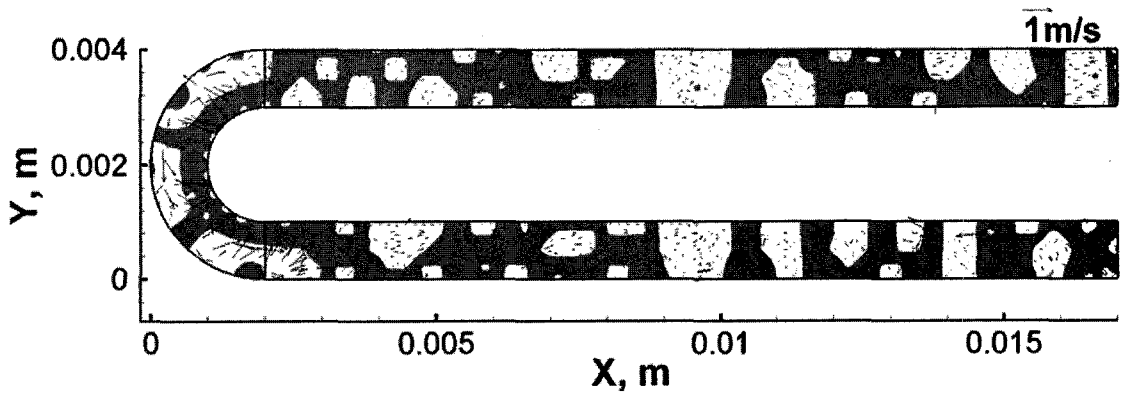

(d)

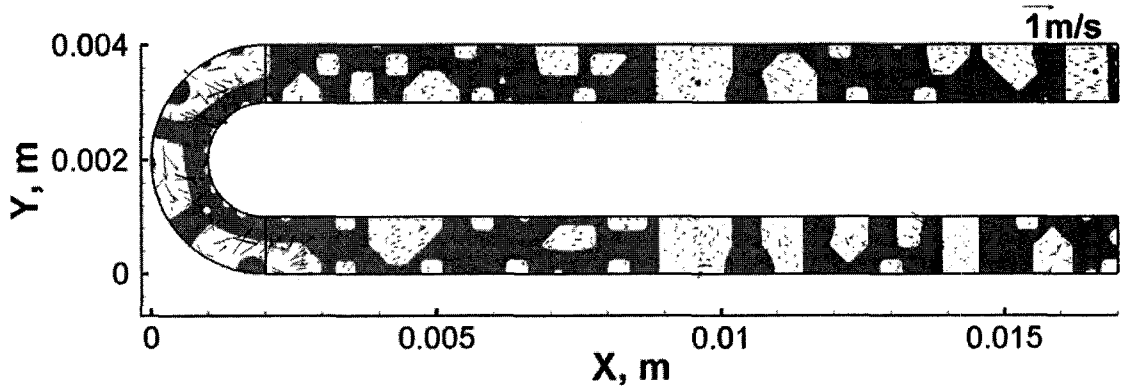

(e)

Fig. 44. Water distribution and velocity field on the center-plane (z = 0.001125 m) in the membrane/catalyst layer for Case 1.

(a: t = 0.0001 s; b: t = 0.0005 s; c: t = 0.005 s; d: t = 0.007 s; e: t = 0.02 s)

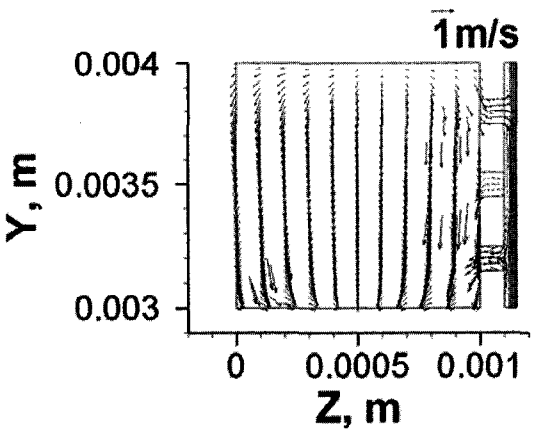

(a)

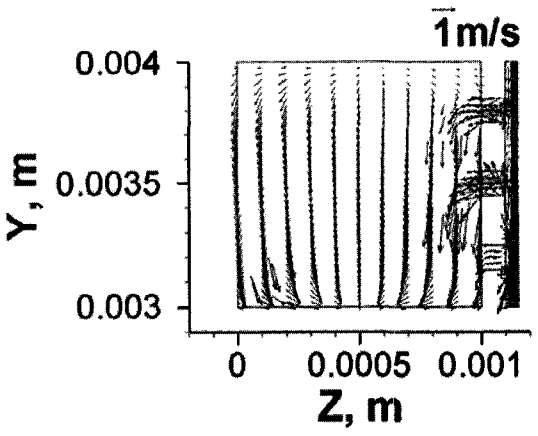

(b)

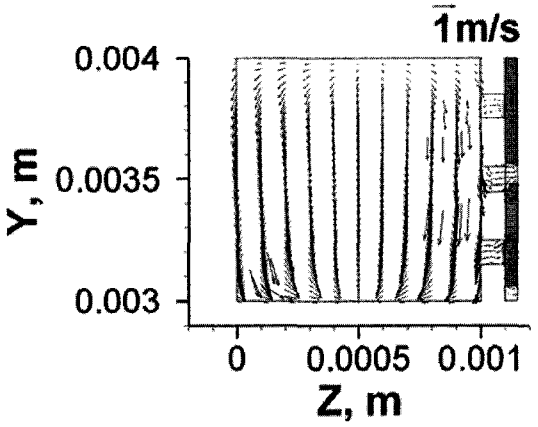

(c)

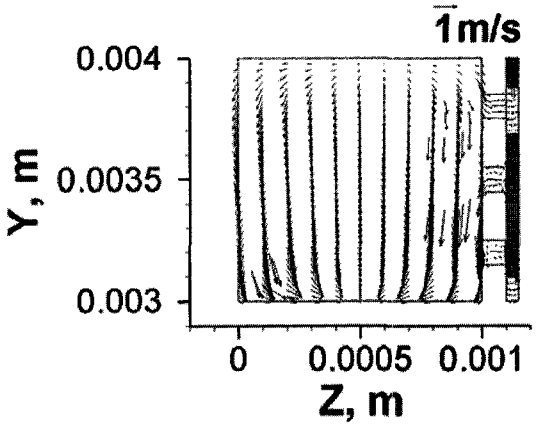

(d)

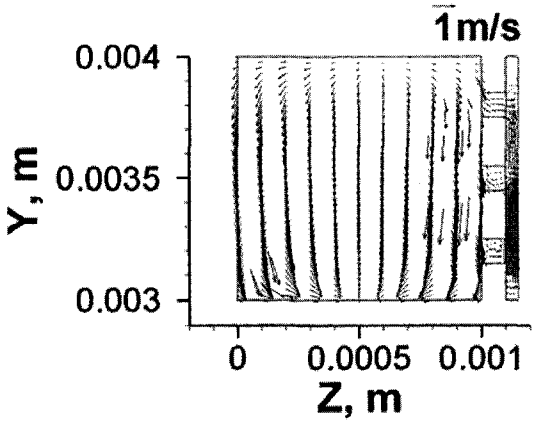

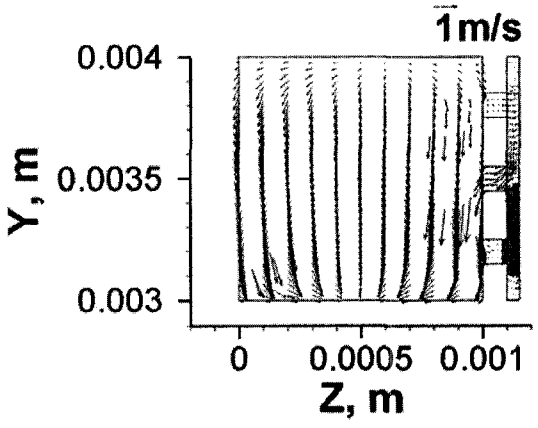

(e) (f)

Fig. 45. Water distribution and velocity field on the plane at x = 0.00205 m in inlet section for Case 1.

(a: t = 0.0001 s; b: t = 0.0005 s; c: t = 0.001 s; d: t = 0.002 s; e: t = 0.003 s; f: t = 0.02 s)

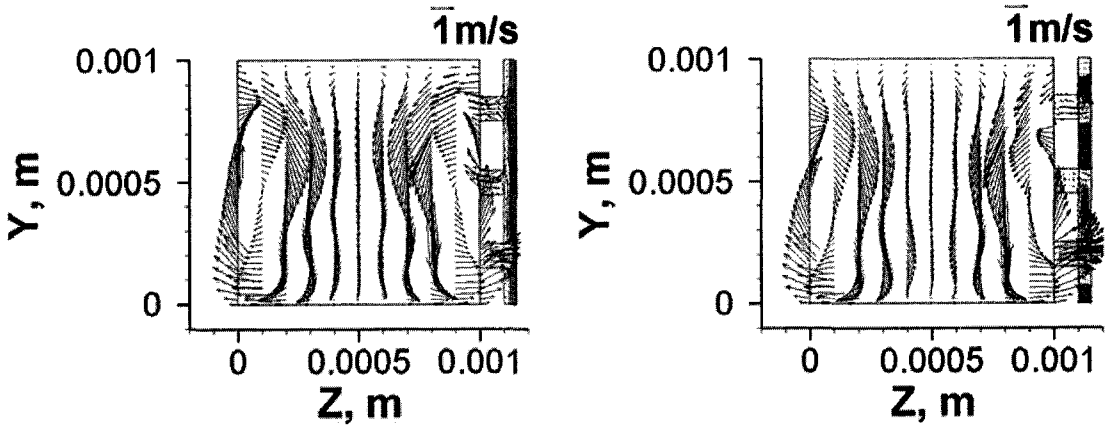

(a) (b)

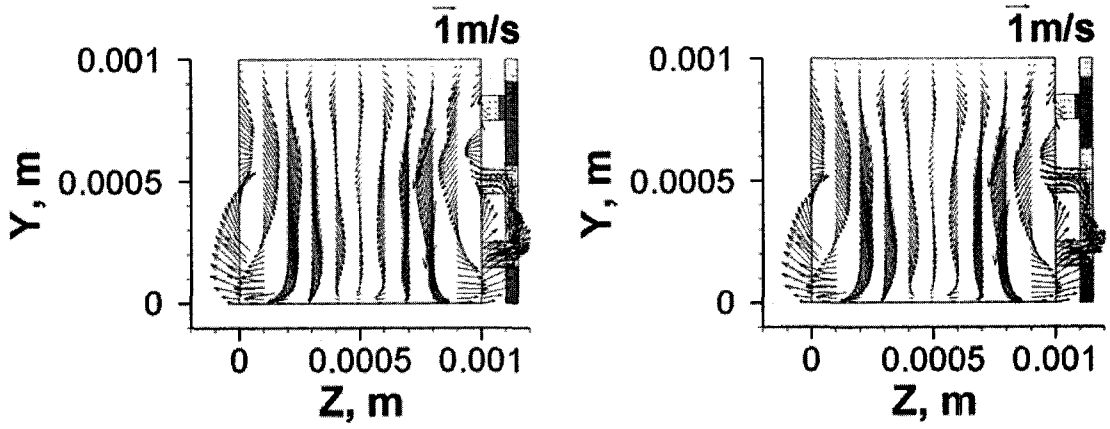

(c) (d)

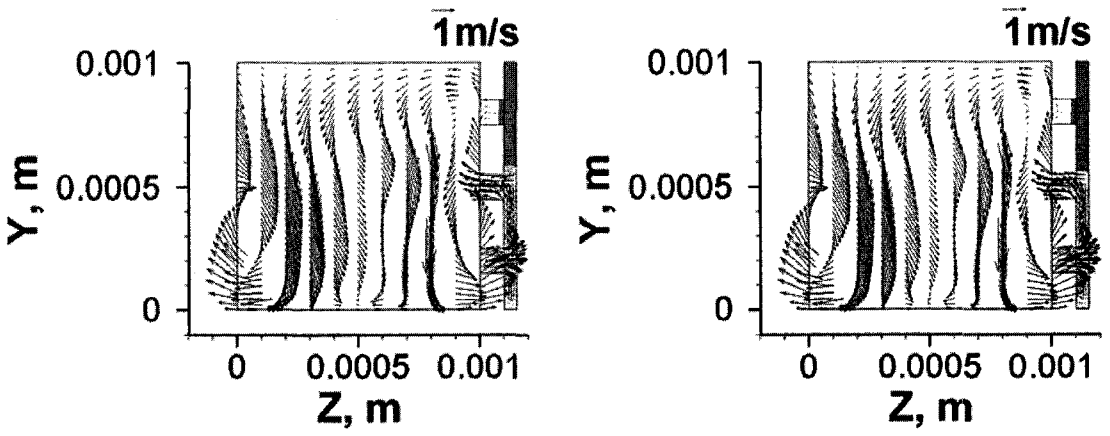

(e) (f)

Fig. 46. Water distribution and velocity field on the plane at x = 0.00205 m in outlet section for Case 1.

(a: t = 0.0001 s; b: t = 0.0005 s; c: t = 0.001 s; d: t = 0.002 s; e: t = 0.007 s; f: t = 0.02 s)

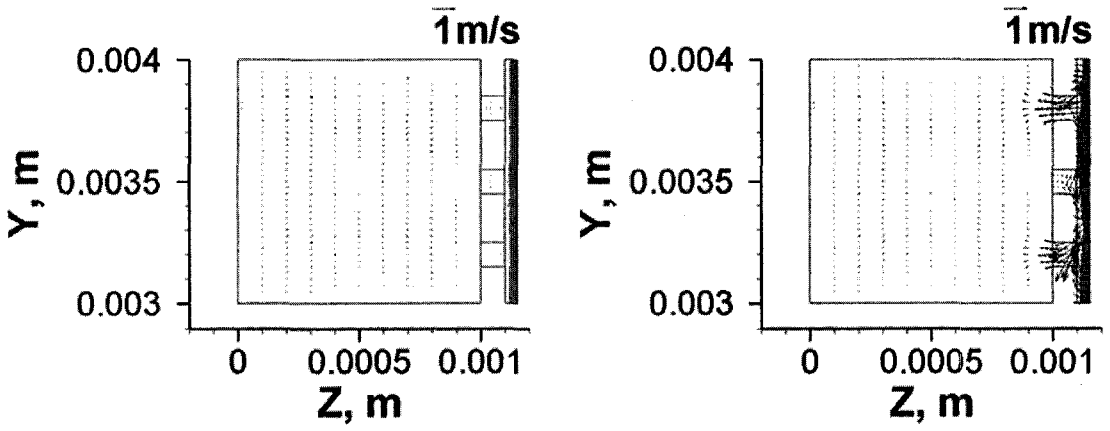

(a) (b)

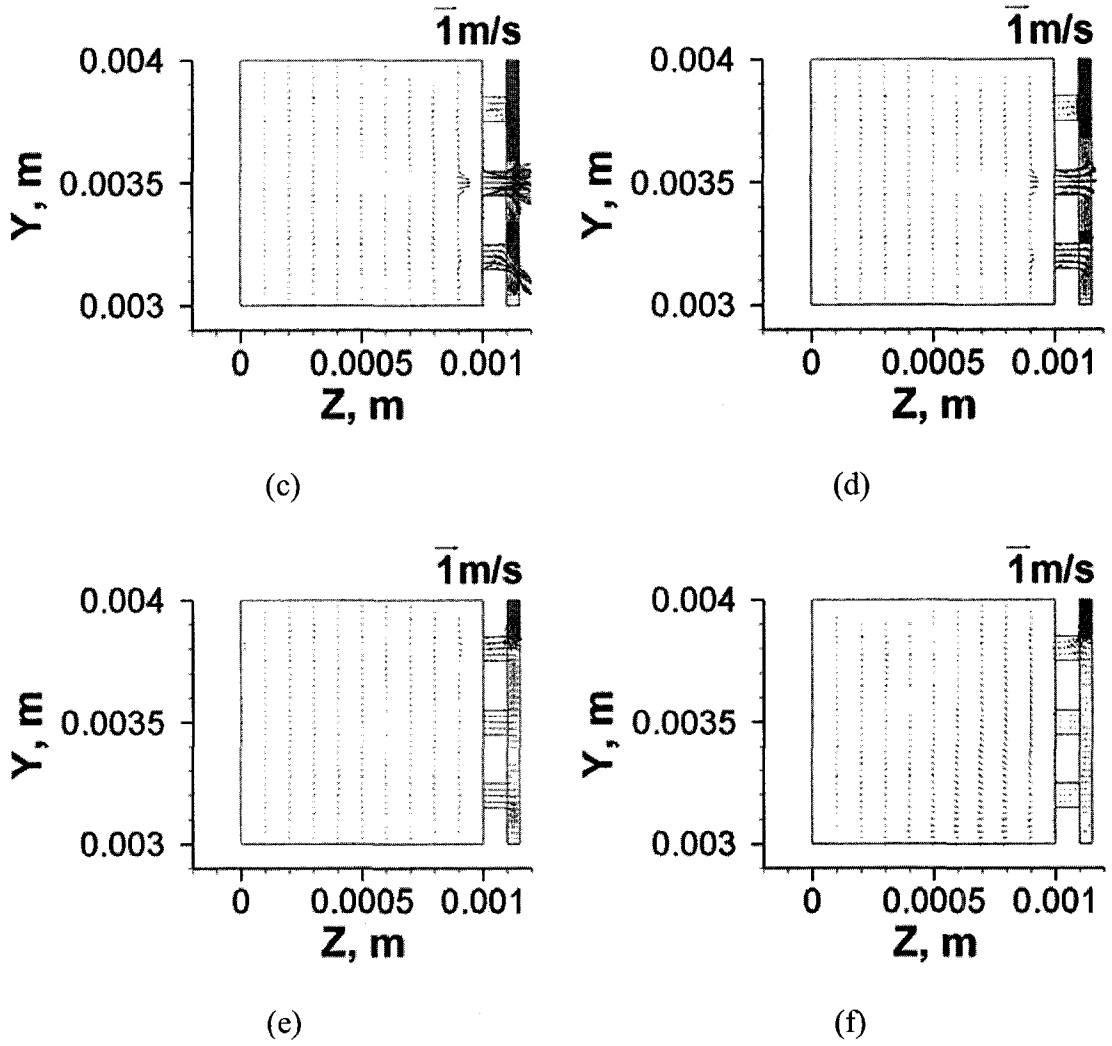

Fig. 47. Water distribution and velocity field on the plane at x = 0.01105 m in inlet section for Case 1.

(a: t = 0.001 s; b: t = 0.002 s; c: t = 0.0022 s; d: t = 0.0025 s; e: t = 0.003 s; f: t = 0.02 s)

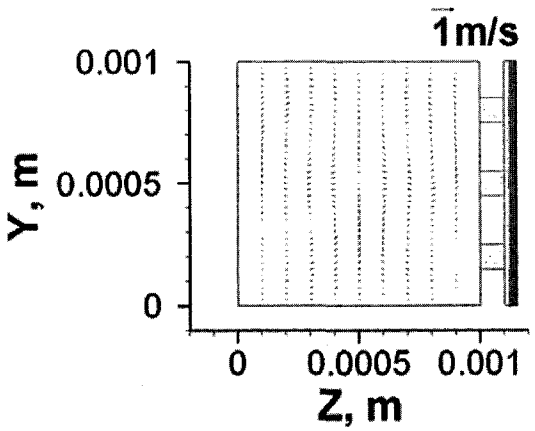

(a)

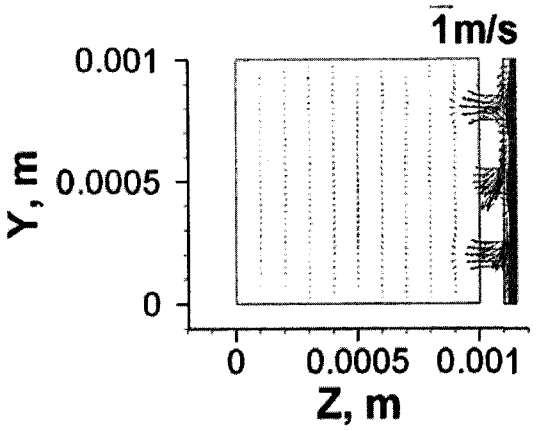

(b)

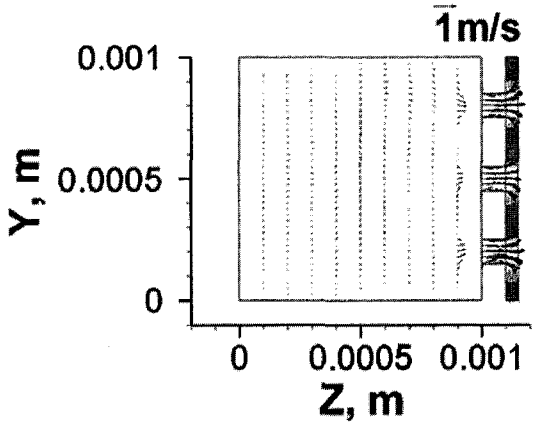

(c)

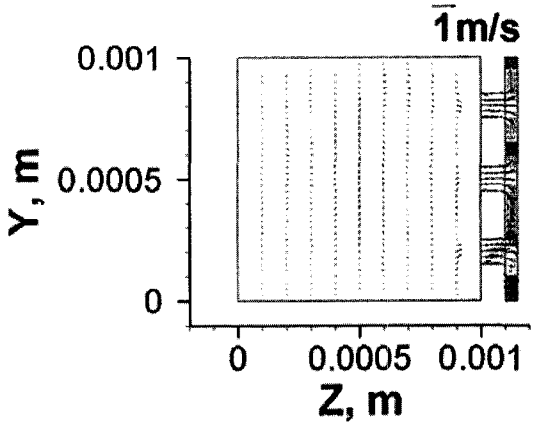

(d)

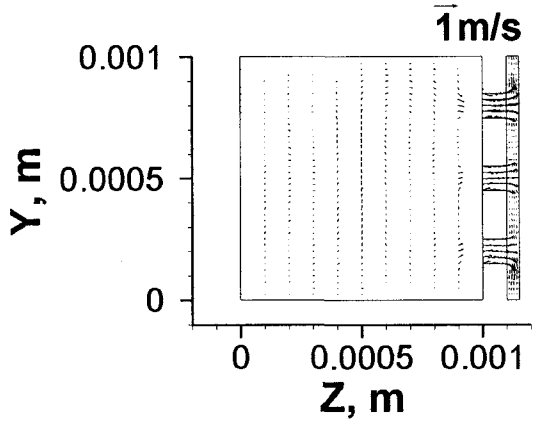

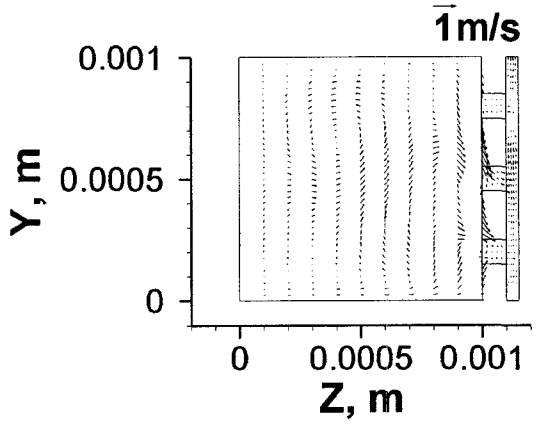

(e) (f)

Fig. 48. Water distribution and velocity field on the plane at x = 0.01105 m in outlet section for Case 1.

(a: t = 0.001 s; b: t = 0.002 s; c: t = 0.0022 s; d: t = 0.0025 s; e: t = 0.003 s; f: t = 0.02 s)

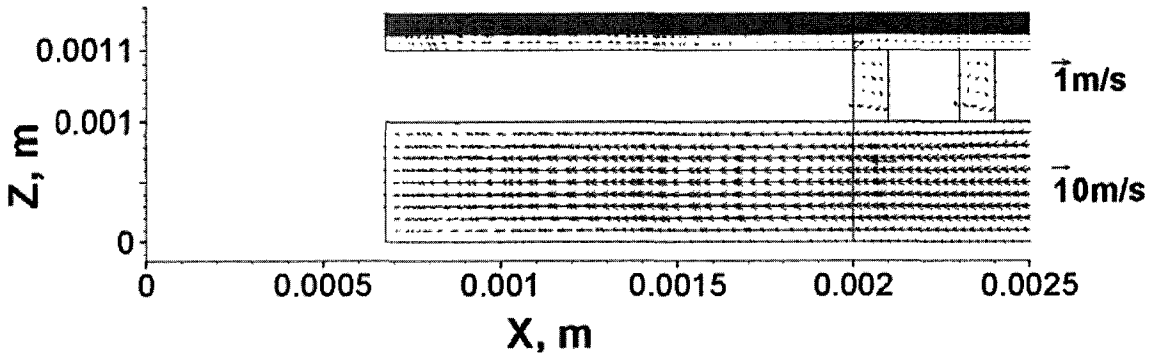

(a)

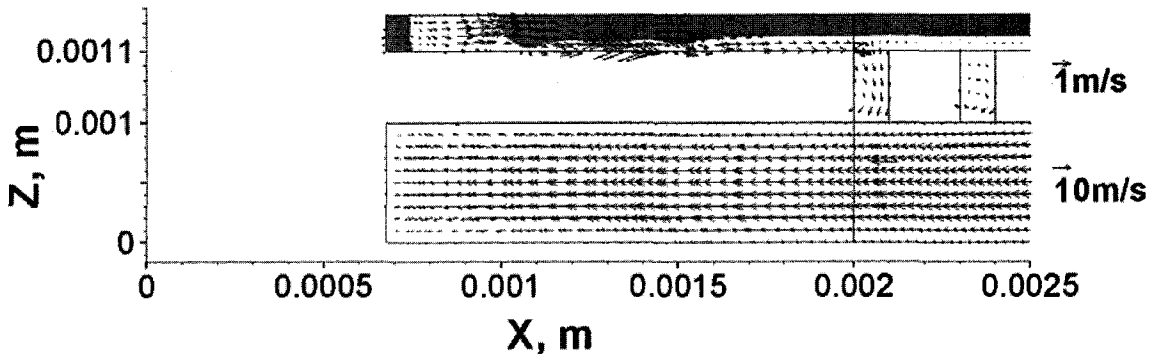

(b)

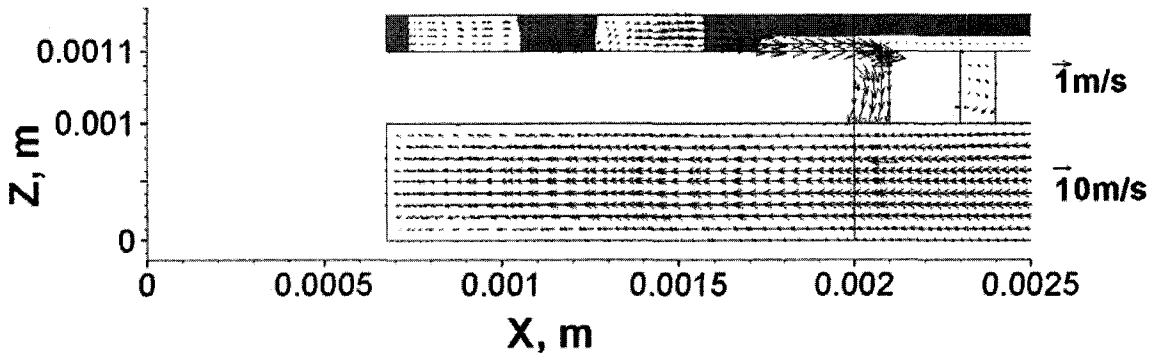

(c)

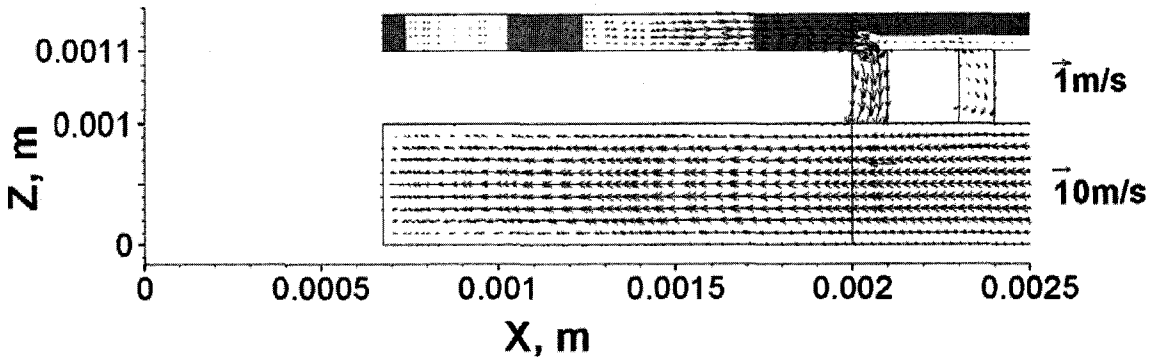

(d)

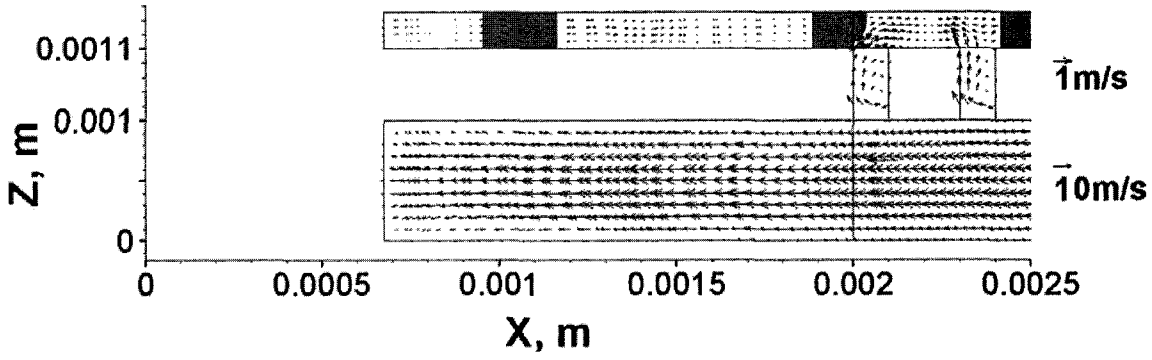

(e)

Fig. 49. Water distribution and velocity field on the center-plane (y = 0.0035 m) in inlet section at the corner for Case 1.

(× 2 magnification along the z-direction for the MEA, × 3 minification along the z-direction for the flow channel) (a: t = 0.0001 s; b: t = 0.0002 s; c: t = 0.0003 s; d: t = 0.0005 s; e: t = 0.001 s)

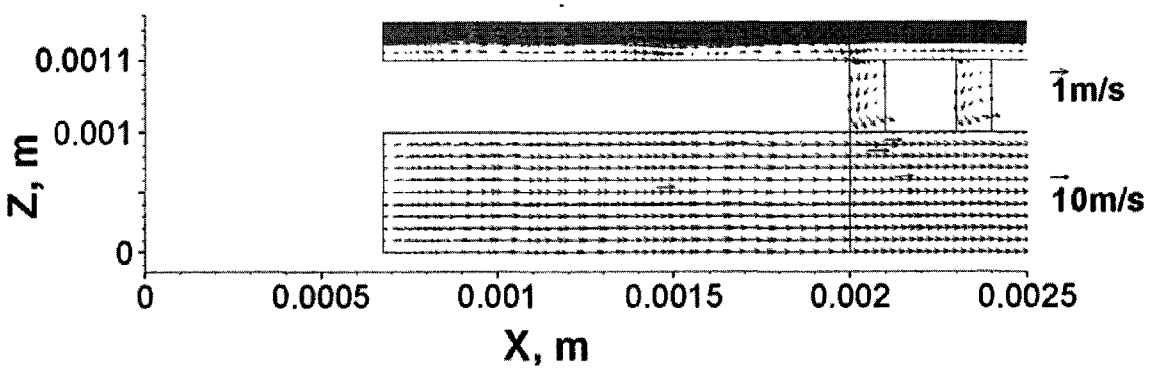

(a)

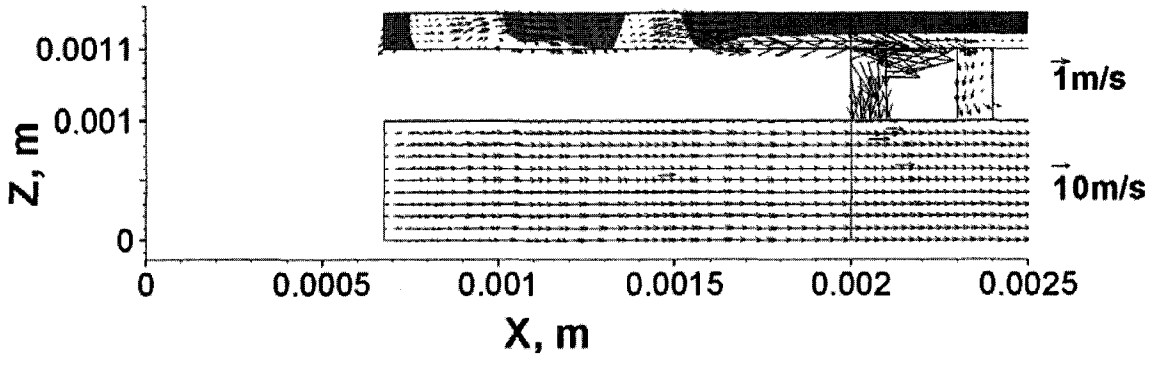

(b)

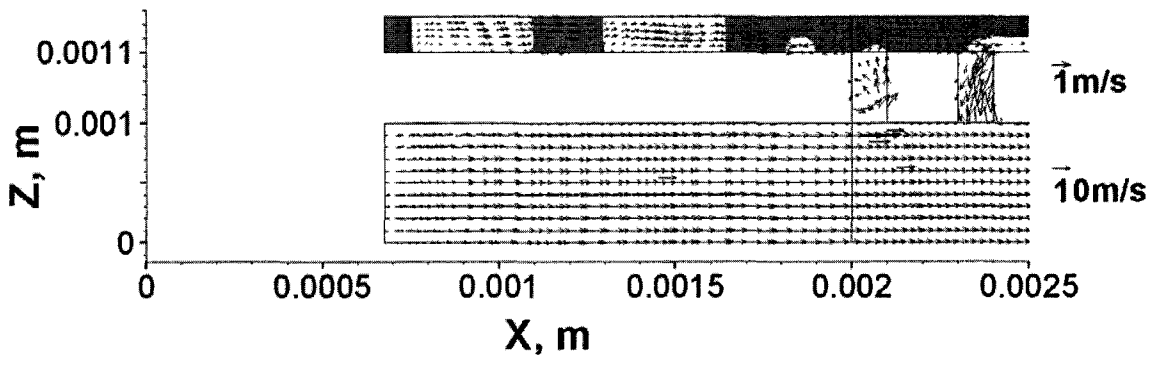

(c)

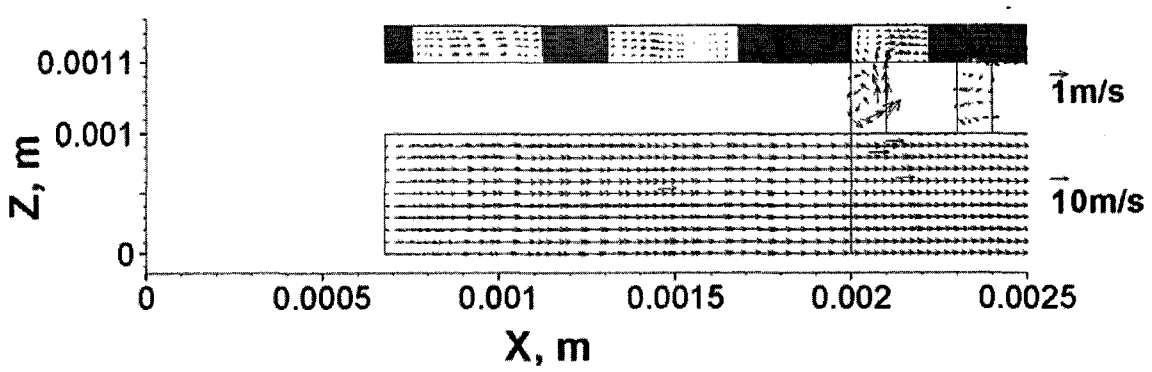

(d)

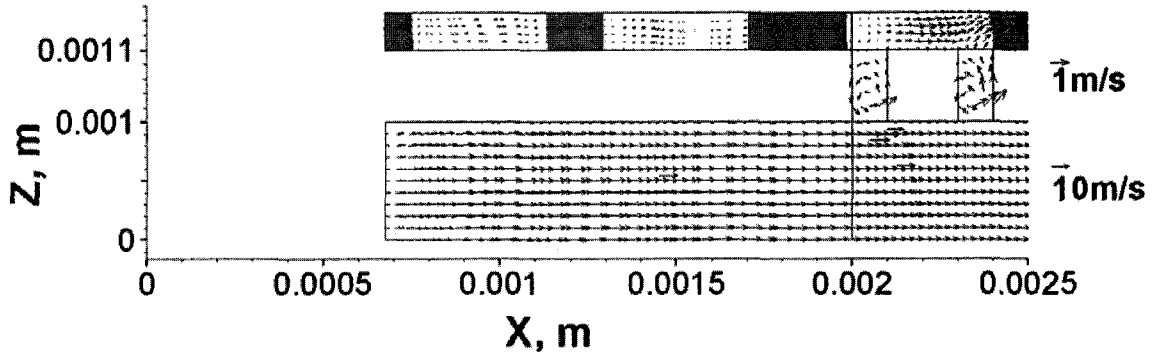

(e)

Fig. 50. Water distribution and velocity field on the center-plane (y = 0.0005 m) in outlet section at the corner for Case 1.

(× 2 magnification along the z-direction for the MEA, × 3 minification along the z-direction for the flow channel) (a: t = 0.0001 s; b: t = 0.0002 s; c: t = 0.0003 s; d: t = 0.0004 s; e: t = 0.0005 s)

At the air flow inlet, because the air flow was not fully developed, the air flow around the boundaries was stronger than that of the fully developed flows further from the inlet. Stronger air flow was formed across the porous holes close to the inlet, thus breaking up the balance between the air and water, and ruptured areas were formed as well. Fig. 51 shows the detailed process on the center-plane at the inlet section. At t = 0.001 s (Fig.

51a), the deformation of the water film could be observed, and then at t = 0.0011 s (Fig. 51b), the deformation increased and stronger air flow was formed across those porous holes. Ruptured areas were formed and strong air streams were flowing across the porous holes into the catalyst layer at t = 0.0012 s (Fig. 51c). Later on, those air streams started moving the liquid water in the catalyst layer along the negative x-direction, and more ruptured areas were formed from the initial raptures, as shown in Figs. 51d and 51e.

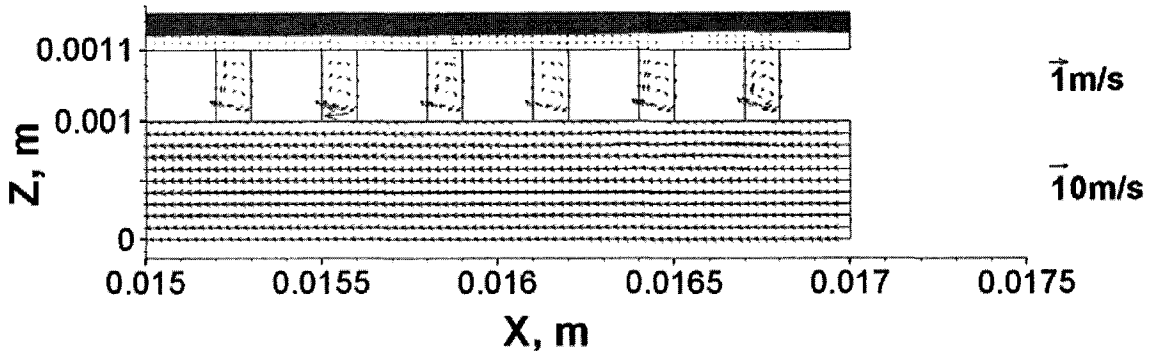

(a)

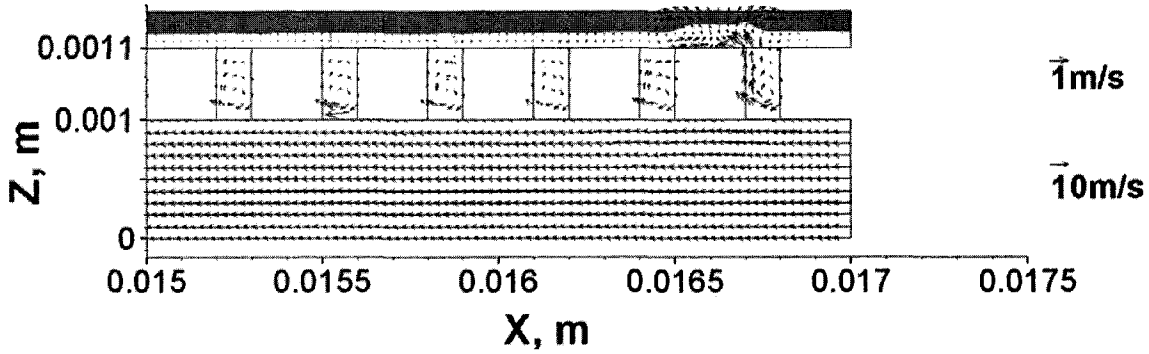

(b)

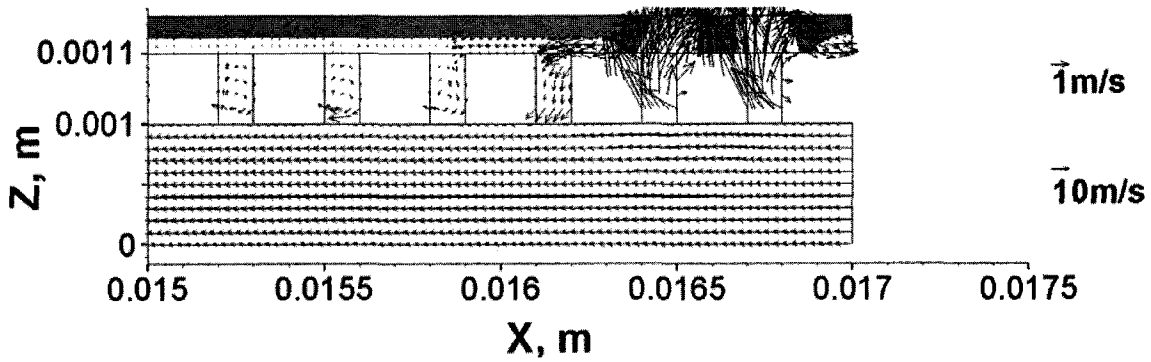

(c)

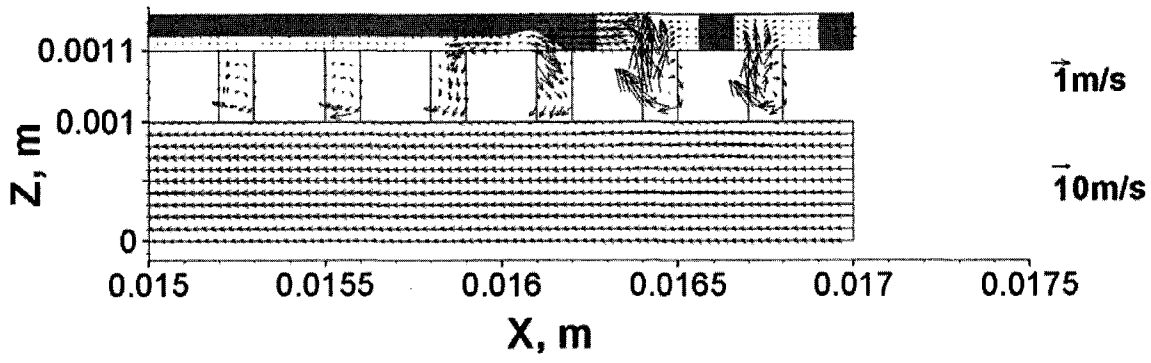

(d)

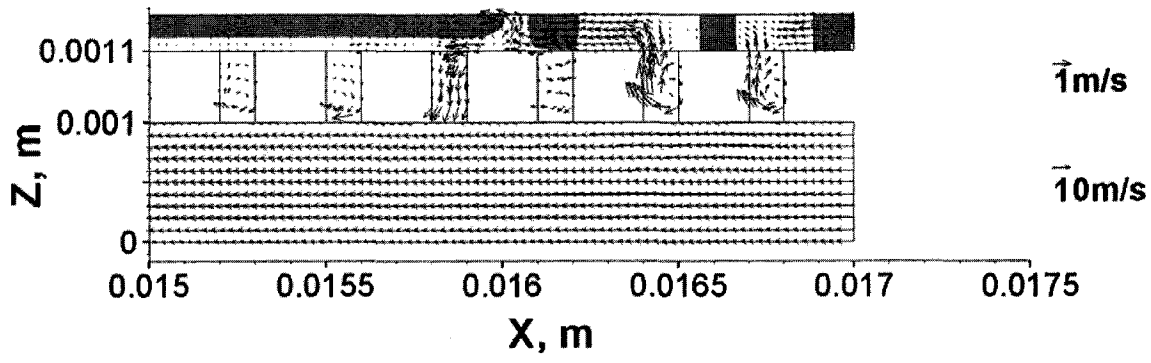

(e)

Fig. 51. Water distribution and velocity field on the center-plane (y = 0.0035 m) in inlet section at the inlet for Case 1.

(×2 magnification along the z-direction for the MEA, ×3 minification along the z-direction for the flow channel) (a: t = 0.001 s; b: t = 0.0011 s; c: t = 0.0012 s; d: t = 0.0014 s; e: t = 0.0015 s)

As mentioned, liquid water films ruptured at the corner due to the stronger secondary flow and the inlet due to the developing flow. Air started moving from those ruptured areas towards the rest of the un-ruptured water films. The whole process could be observed in 3d view from Fig. 43. Fig. 44 presents the water distribution and velocity field on the center-plane of the catalyst layer. At t = 0.003 s, as shown from Fig. 43, for the inlet straight section (upper section), the water film was broken up from both the inlet and the corner, and for the outlet straight section (lower section), water film was only broken up from the corner. At t = 0.005 s, the whole water film in the inlet straight section was ruptured while there was still a small part left in the outlet straight section, which is close to the gas flow outlet. For the straight section at the inlet, even though the ruptures occurred from the both ends, the rupture that occurred from the corner (from t = 0.0001 s) was earlier than that from the inlet (t = 0.0013 s). In real operating conditions, the flow fields in most parts of the gas flow channels are fully developed, therefore, the rupture of water films at the corner and the spreading to both of the straight sections are the most important flow phenomena that should be considered. By comparing Figs. 45 to 49, for the cross sections of both straight sections, it could also be observed that on the

cross sections closer to the corner (x = 0.00202 m), the rupture occurred earlier (t = 0.001 s) than on the cross sections further from the corner (x = 0.01102 m, t = 0.002 s). It can be observed that the spreading speeds of the rupture along both straight sections were almost the same (the outlet straight section was slightly faster). This could prove that the effect of the flow direction inside the gas flow channel on the flow direction in the catalyst layer is very small because the flow direction inside the catalyst layer is mainly dominated by the water distribution (flowing from empty sections towards liquid water).

After a period of time, as shown from Figs. 43e, 43f, 44d and 44e, all the water films were broken up into different pieces. It could be observed that since t = 0.007 s, most of the water was no longer moving. The velocity field achieved steady-state and the balance between air and liquid water was attained, which means, all the forces between the two phases, such as surface tension, viscous stresses, wall adhesions etc. were balanced. For example, as shown in Fig. 44e, at the corner, it could be observed that air was flowing from the empty sections to the liquid water. The liquid water was surrounding the inner boundary of the serpentine corner and there was no path for the liquid water to flow elsewhere. This part of liquid water therefore achieved a balance of the forces. When the balance was achieved (no significant movement of liquid water could be observed), as shown in Fig. 44e, there was almost no liquid water isolated from the surrounding walls. Almost all the liquid water was connecting to the surrounding walls to achieve the force balance.

From Figs. 45f, 46f and 47f, at t = 0.02 s while the force balance was achieved, water had difficulties staying between two porous holes and such places suffered air streams flowing from the surrounding holes. Therefore, it is challenging for such places to maintain liquid water, which is good for water drainage. On the other hand, those places around the surrounding wall, which maintained most of the liquid water, are not good for water drainage. In real PEM fuel cell operating conditions, if a whole piece of MEA was considered, these surrounding walls as shown from Fig. 44e, would be connecting to the catalyst layer under the lands of the bipolar plates. Such places are the ideal destinations that the liquid water should move to. Therefore, it could be concluded that for the catalyst layer, the areas under the lands of the bipolar plate and those close to the surrounding walls are the most possible places that liquid water would move to. Other locations that suffer strong air flow and are not surrounded by any walls are relatively difficult in maintaining liquid water.

Fig. 52 shows the water distribution and velocity fields on the x-y planes at both ends of the catalyst layer after the balance between air and liquid water was achieved (t = 0.02 s). It could be observed that the water distributions on these two planes were almost the same. The plane closer to the GDL (Fig. 52a) contained slightly smaller amounts of water because it is closer to the air flow. Additionally, by considering Fig. 44e which shows the plane between them at the same time, very similar water distribution could be observed. Therefore, it could be concluded that liquid water inside the catalyst layer would tend to reach a force balance by touching both the top and bottom surfaces. This is the most stable condition for liquid water because the force due to the wall adhesion effects is the

maximum and the effect of the surface tension between air and liquid water is the minimum.

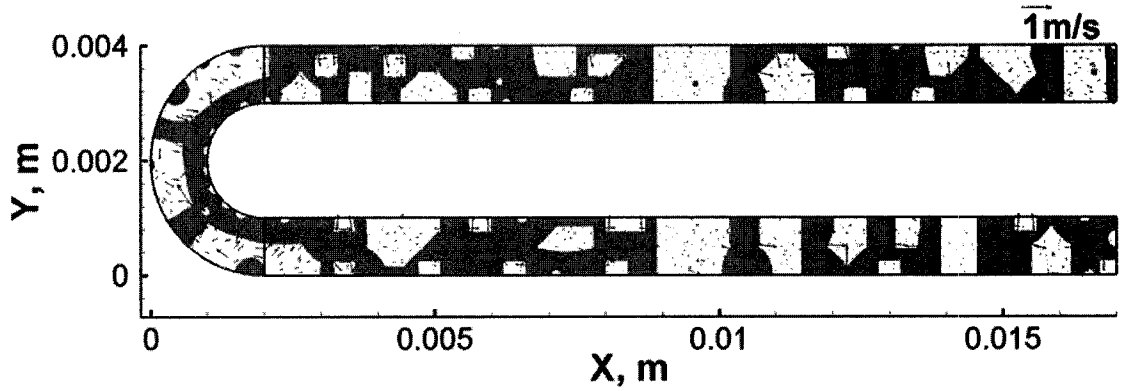

(a)

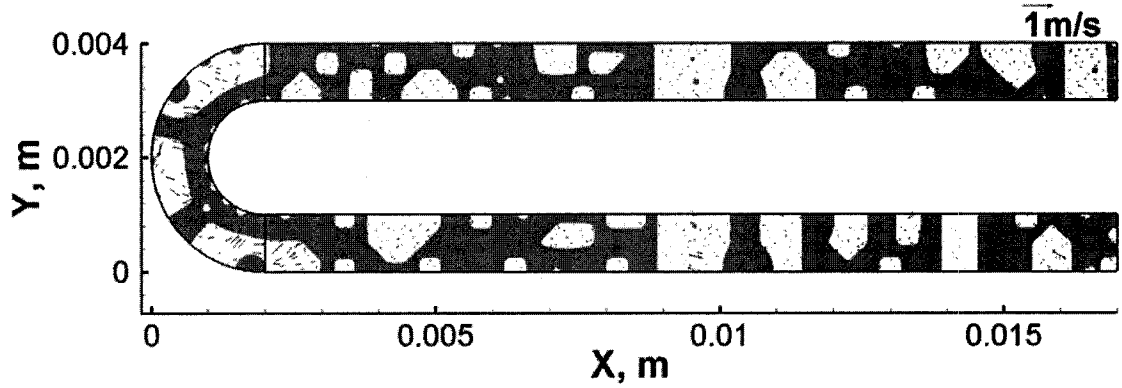

(b)

Fig. 52. Water distribution and velocity field on the planes close to the GDL (z = 0.0011 m) and close to the membrane (z = 0.00115 m) at t = 0.02 s for Case 1.

(a: z = 0.0011 m; b: z = 0.00115 m)

6.1.2 Water occupation fraction variation

Fig. 53 shows the water occupation fraction (the average volume fraction of water) inside the MEA for Case 1. It was observed that the total water occupation fraction inside the MEA only decreased from 50.4% to 44.9% i.e. only a very small amount of water was removed. It was observed that the water amount inside straight sections of the MEA even increased. This is because liquid water inside the corner moved into those straight sections, as mentioned above. At the beginning, the water occupation fraction inside the straight sections reached the maximum. This is because in that time period, the rate of liquid water moving into those sections from the corner was higher than the rate of water moving out. Later on, a slight reduction of water occupation fraction inside those straight sections could be observed; because at that time the rupture of liquid water films at the corner was complete and water movement relatively decreased. After the balance was achieved, the water occupation fraction inside the straight sections became almost constant. Furthermore, water occupation fraction inside the straight section at the inlet was larger than at outlet (the total volume of these two sections are the same). This could be explained with the help of Fig. 44b, at t = 0.0005 s, as the water films ruptured at the corner, it could be noticed that water films also ruptured from the left side of the straight section at outlet, close to the corner. Such rupture was, however, not observed at the inlet straight section. This is because as air flowed through the corner, the secondary flow was still very strong although air already flowed into the straight section. The comparison of the secondary flow before entering the corner and after exiting could be noticed in Figs. 45 and 46. Fig. 46 (for the outlet section) showed stronger secondary flow than Fig. 45 (for the inlet section). Therefore, water films ruptured from the left side of the straight

section at outlet first, at the strong air flow formed there could prevent some water flowing from the corner, thus explaining why the straight section at inlet contained more water. It could also be observed that the straight section at inlet reached a constant water occupation fraction earlier than at outlet. This is because for the straight section at inlet, liquid water ruptured from the both ends (as mentioned, also from the inlet due to the developing flow), thus the liquid water ruptured faster than the straight section at outlet. The highest reduction of water occupation fraction could be observed at the corner, which was only 9% by comparing its original water occupation fraction at 54%. The strong secondary flow at the corner did not help removing the water significantly, and the 9% even contained some water flowed into the straight sections.

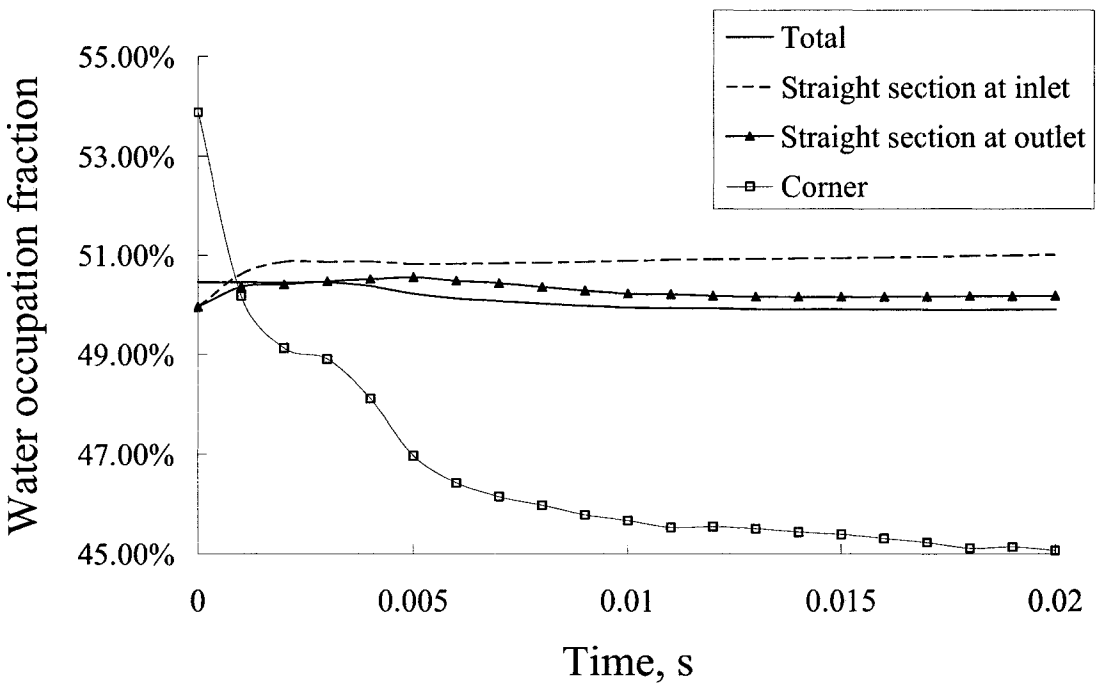

Fig. 53. Water occupation fraction inside the MEA for Case 1.

Fig. 54 shows the water occupation fraction inside the catalyst layer for Case 1. This figure showed a very similar water variation to that shown in Fig. 53. However, in the catalyst layer, water occupation fractions inside the straight sections were finally less than the initial condition. This is because some water moved into the GDL. Fig. 55 shows the water occupation fraction inside the GDL for Case 1. As mentioned above water was only removed significantly at the corner, however, the porous holes contained the most water at the corner and the straight section at inlet contained the least. The reason that the GDL also contained some water after the balance was achieved is as discussed above. All the water was finally connecting to the both ends of the catalyst layer and the water could also be able extend into the GDL and remain balanced due to water's viscosity. Such phenomena could be observed in Figs. 45 and 46.

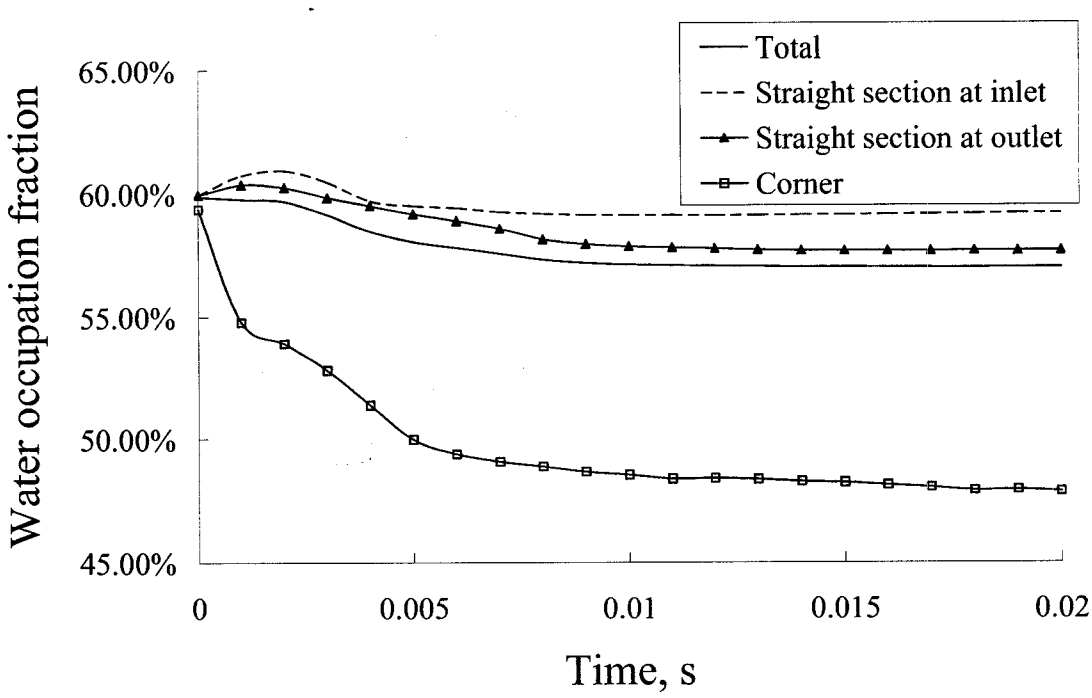

Fig. 54. Water occupation fraction inside the catalyst layer for Case 1.

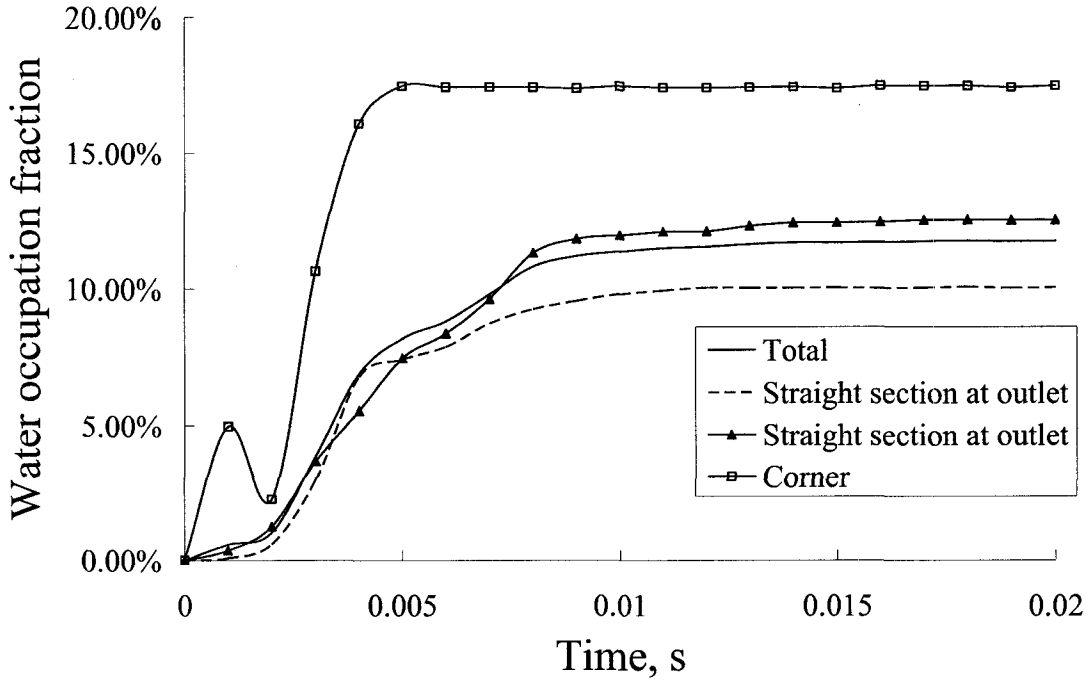

Fig. 55. Water occupation fraction inside the GDL for Case 1.

It could be concluded that the secondary flow is still strong after exiting the serpentine corner; therefore, the water was easier to be removed after air exits from the corner than before air enters the corner. Even though water was removed faster at the corner, some parts of the water did not flow into the flow channel but flowed into other parts of the MEA, which is still not good for PEM fuel cell performance. The more water removed from the catalyst layer, the more possibility that the GDL contains more water. The regular cubic micro-structure of the GDL is not good for water removal as only 0.5% of the total volume was removed with this structure.

6.2 Case 2: Water films with a thickness of 0.03 mm placed on membrane/catalyst layer for computation domain 2

The second case was simulated to investigate the effects of the GDLs with trapeziform micro-structures on liquid water flow behaviour. The trapeziform porous holes in computation domain 2 (Fig .6c) had a height of 0.1 mm along the z-direction with the minimum area (0.1 × 0.1 mm along the x- and y- directions) facing the catalyst layer. As shown in Fig. 13, water films with a thickness of 0.03 mm were placed on the membrane/catalyst layer in computation domain 2. The rupture of water films, change of water amount in the MEA, and water transport inside the MEA were studied.

6.2.1 Rupture of water films

The only difference between the first two cases is the shape of the porous holes. As shown in Fig. 56, it could be noticed that the general water transport phenomena was similar to Case 1. The rupture of water films started at the corner and the inlet with the balance between air and water achieved after all the liquid water films ruptured. Liquid water would stay around the end walls in the catalyst layer and almost all the liquid water would connect the both ends of the catalyst layer (the membrane side and the GDL side). Fig. 57 shows the cross section on the y-z planes close to the corner. It was noticed that the secondary flow in the plane at the downstream of the corner was stronger than at the upstream (also shown in Case 1).

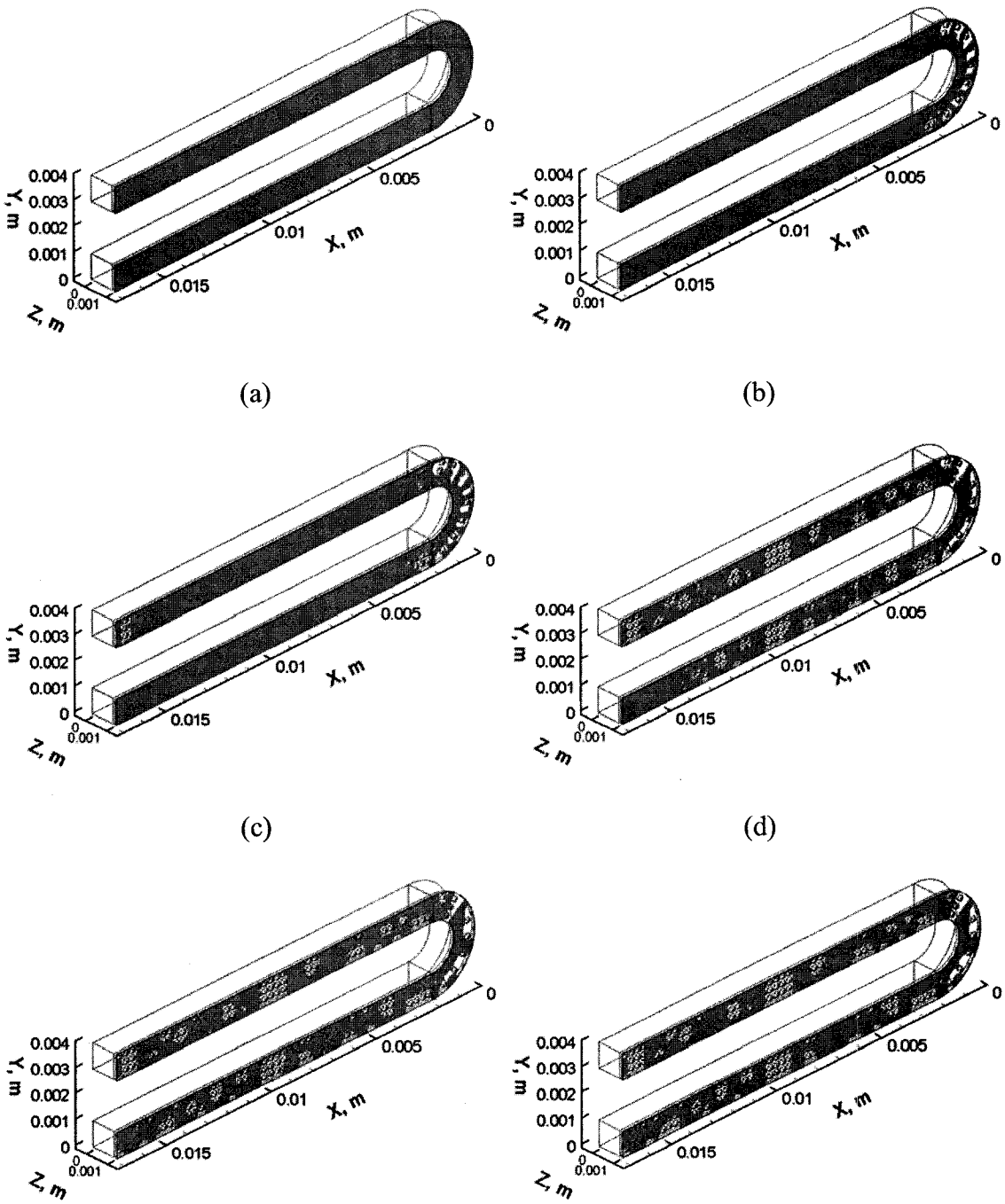

Fig. 56. Rupture of water films in 3-D view for Case 2.

(a: t = 0 s; b: t = 0.0005 s; c: t = 0.001 s; d: t = 0.005 s; e: t = 0.01s; f: t = 0.02 s)

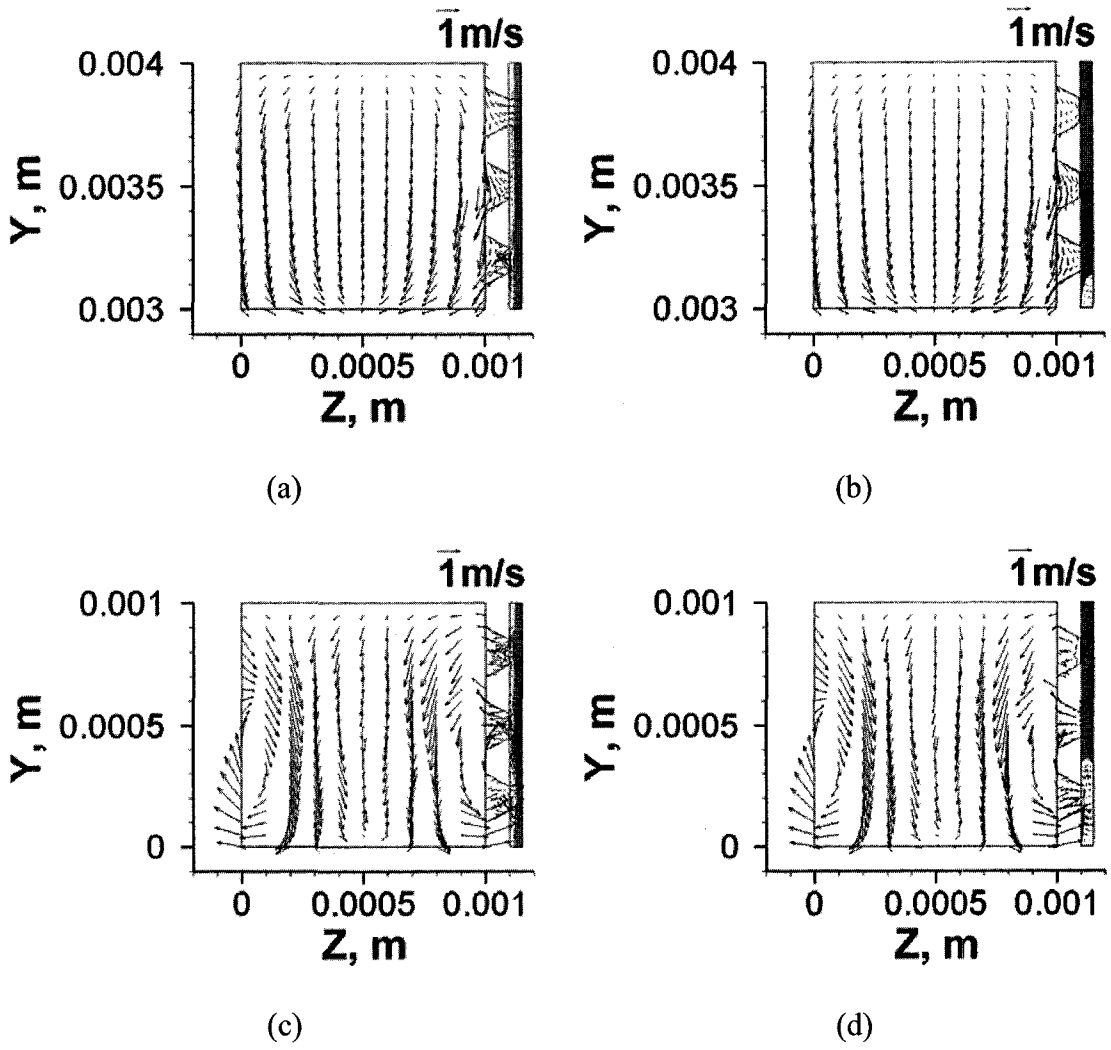

Fig. 57. Water distribution and velocity field on the plane at x = 0.00205 m in both inlet and outlet sections for Case 2.

(a: t = 0.0001 s at inlet section; b: t = 0.02 s at inlet section; c: t = 0.0001 s at outlet section; d: t = 0.02 s at outlet section)

Even though the general flow characteristics between the first two Cases were similar, the water flow behaviours inside the MEA were still different. By observing Figs.56 to 59, no water was flowing into the GDL and thus the water removal ability was even weaker than in Case 1. As shown in Figs. 58 and 59, the water distribution and velocity field on

the center-planes of the inlet and outlet sections could be observed. Initially it was the same as in Case 1 in that the water film was broken up into small pieces, however, later on those small pieces did not flow through the porous holes into the gas flow channel. The small pieces of liquid water attached together again to form larger pieces. Such large pieces are difficult to remove and then the balance between air and water was achieved. With the help of Figs. 58 and 59, the reason that the small pieces of liquid water did not flow through the GDL and formed larger pieces could be explained. The micro-structure of the porous holes was trapeziform in this case with the minimum area facing the catalyst layer. While air flowed through these holes, the direction of the flow started concentrating together along the boundary of the holes. Therefore, the flow between two holes in the catalyst layer was weaker than in Case 1. Because such air flow inside the catalyst layer was weak those small pieces of liquid water became easier to attach to each other rather than being broken up and flowed out of the MEA. As seen from Figs. 58 and 59, the air flow between the pieces of liquid water was not strong enough to prevent them from coalescing. Therefore, after a larger piece was formed, the liquid water became even harder to be removed.

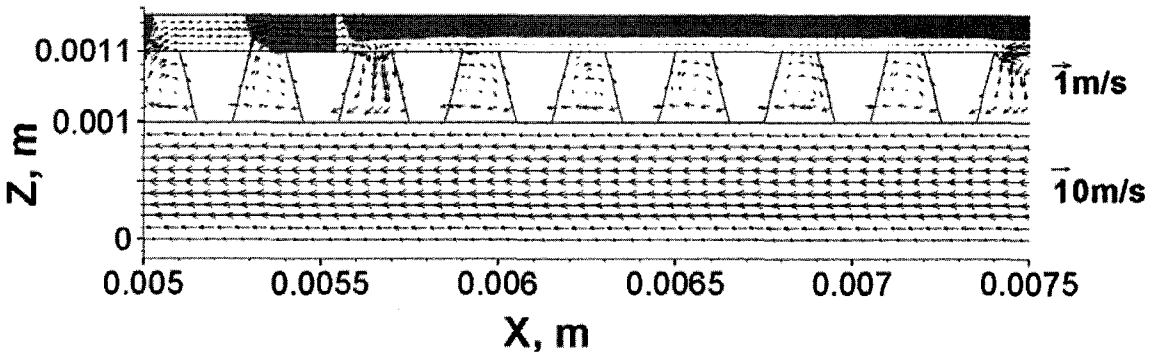

(a)

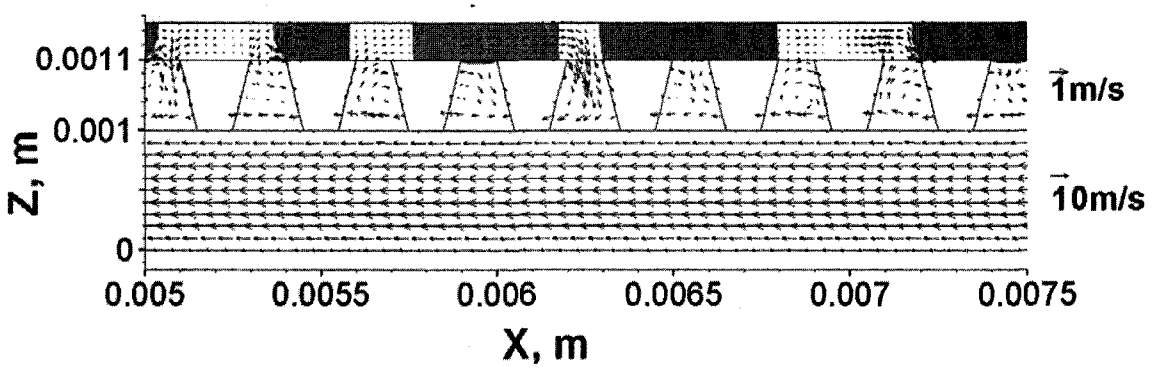

(b)

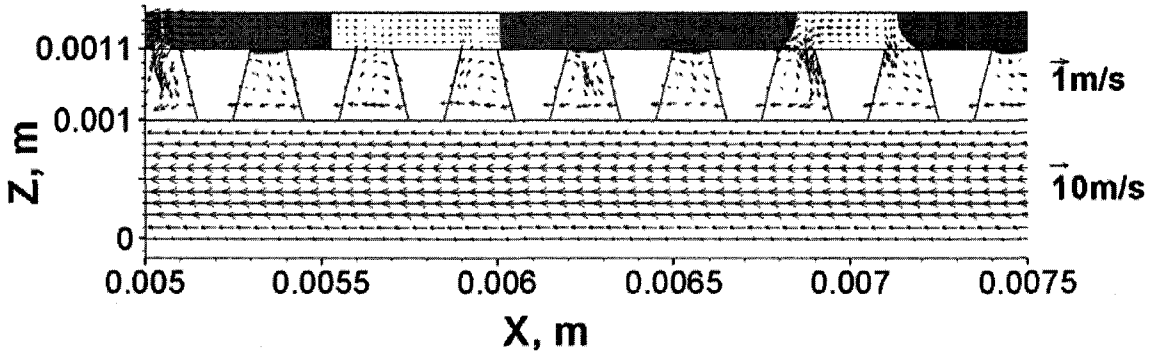

(c)

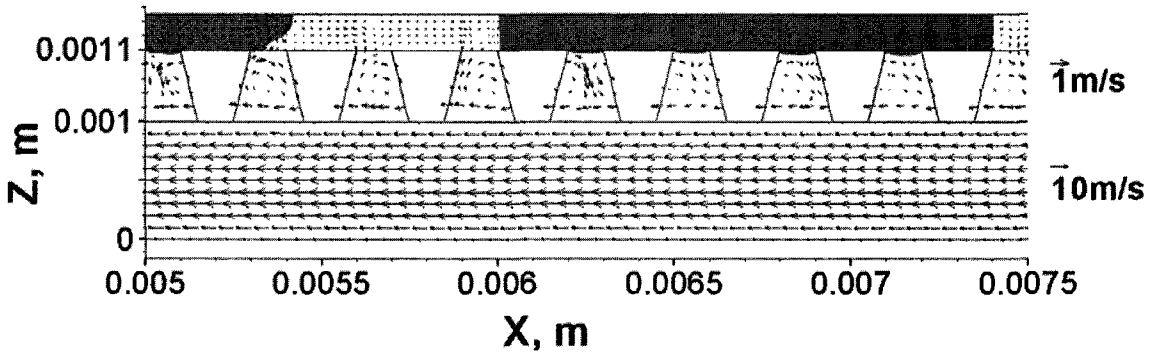

(d)

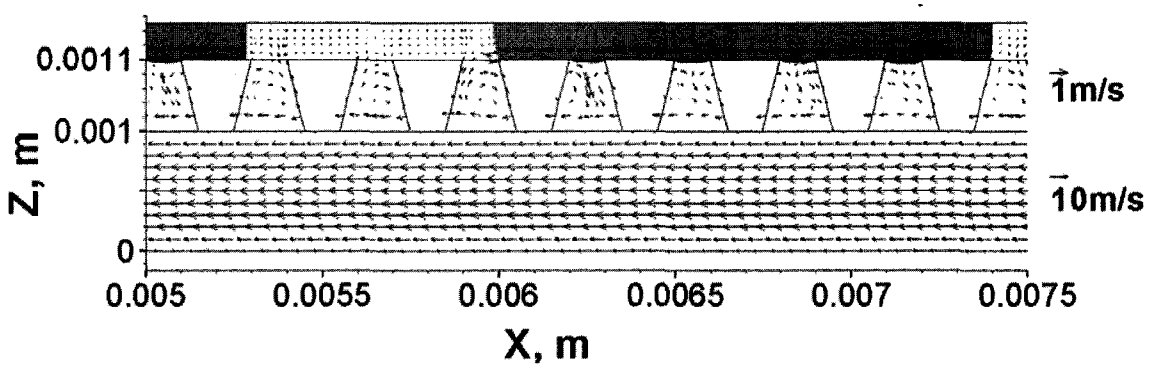

(e)

Fig. 58. Water distribution and velocity field on the center-plane (y = 0.0035 m) in inlet section for Case 2.

(× 2 magnification along the z-direction for the MEA, × 3 minification along the z-direction for the flow channel) (a: t = 0.003 s; b: t = 0.004 s; c: t = 0.005 s; d: t = 0.006 s; e: t = 0.02 s)

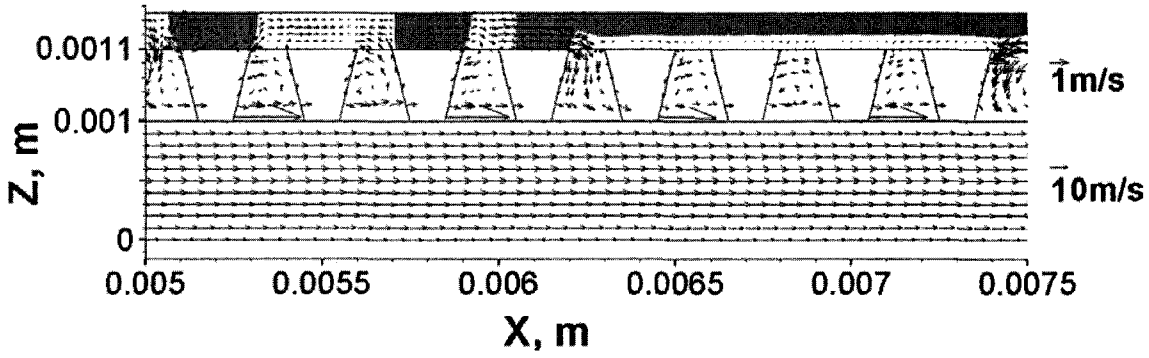

(a)

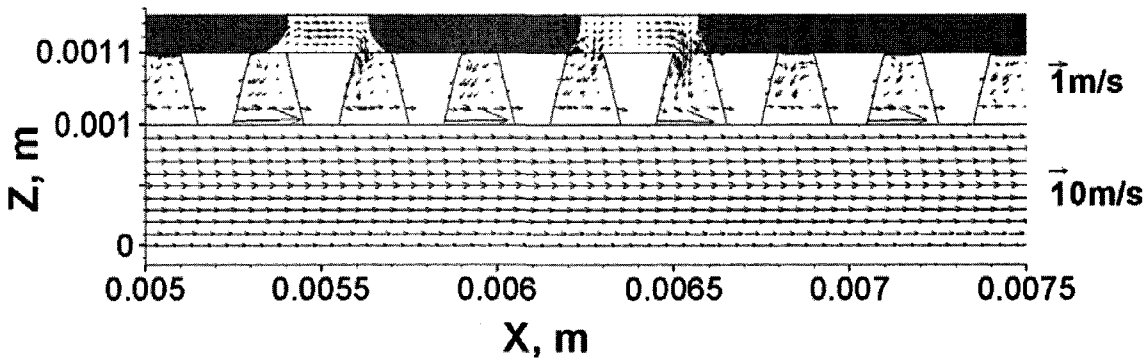

(b)

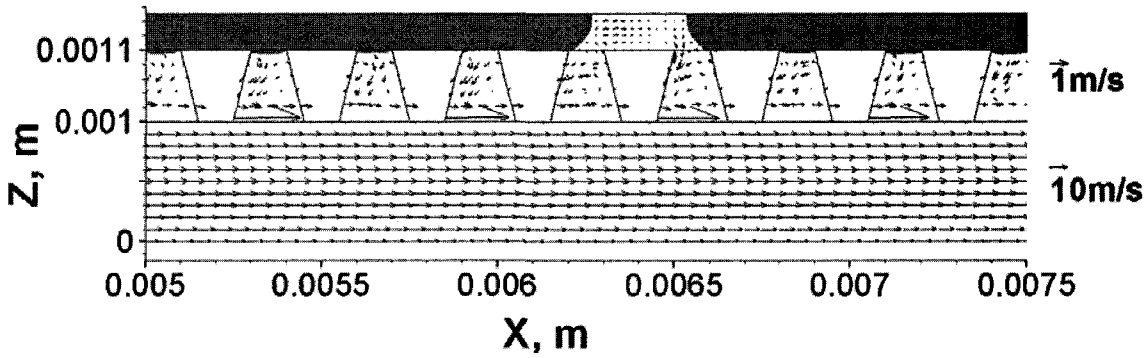

(c)

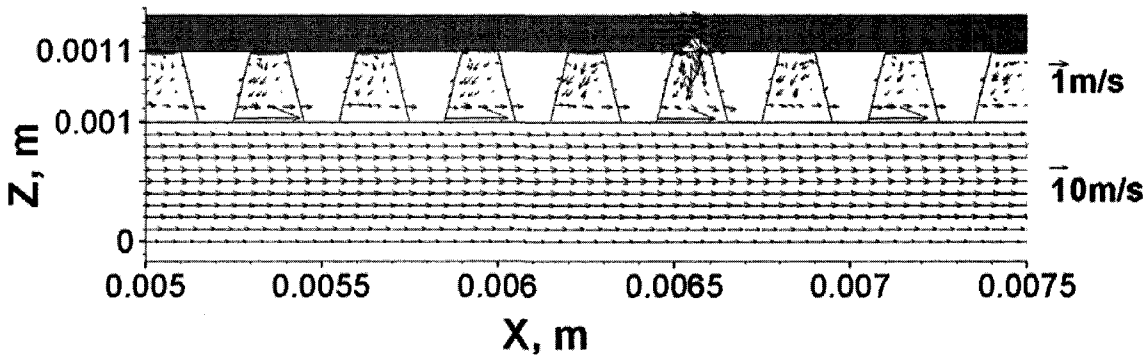

(d)

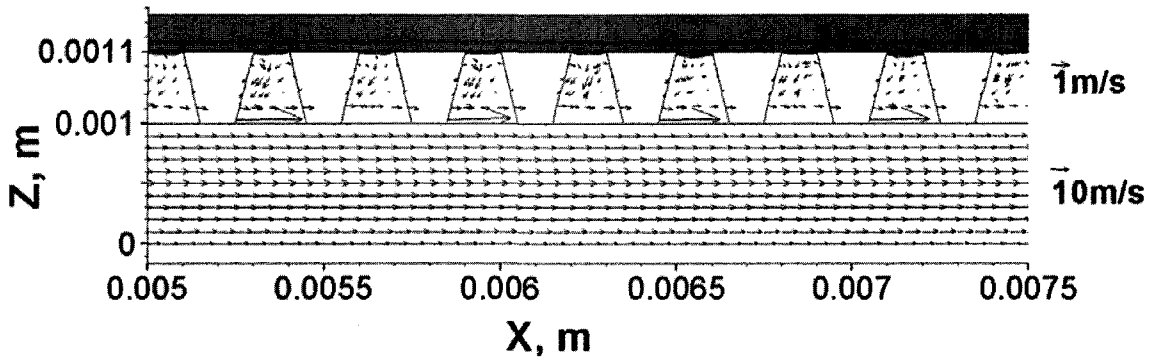

(e)

Fig. 59. Water distribution and velocity field on the center-plane (y = 0.0005 m) in outlet section for Case 2.

(× 2 magnification along the z-direction for the MEA, × 3 minification along the z-direction for the flow channel) (a: t = 0.003 s; b: t = 0.005 s; c: t = 0.007 s; d: t = 0.01 s; e: t = 0.02 s)

6.2.2 Water occupation fraction variation

Fig. 60 shows the water occupation fraction inside the MEA for Case 2. It was observed that there was no water flowing out of the MEA. An initial reduction of water at the corner could be noticed, however, a slight increase of water occupation fraction was observed later. This is because initially some water was flowing from the corner to the straight sections but there was no water removed from the MEA. Therefore, after a period of time, some excess water in the straight sections flowed back into the corner. This could be illustrated by the water occupation fraction variation inside the straight sections which, after an initial increase decreased and then reached constant levels. Because no water was removed from the MEA, in contrast with Case 1, the water occupation fractions in both of the straight sections finally became almost the same. By looking at

the water occupation fraction variation inside the catalyst layer in Fig. 61, a 5% reduction of water occupation fraction at the corner was observed. This part of water flowed into the straight sections resulting in a slight increase of water occupation fraction inside the straight sections. Fig. 62 showed that only a small amount of water flowed into the GDL and the water occupation fraction was only about 0.8%. Therefore, most of the water was still inside the catalyst layer.

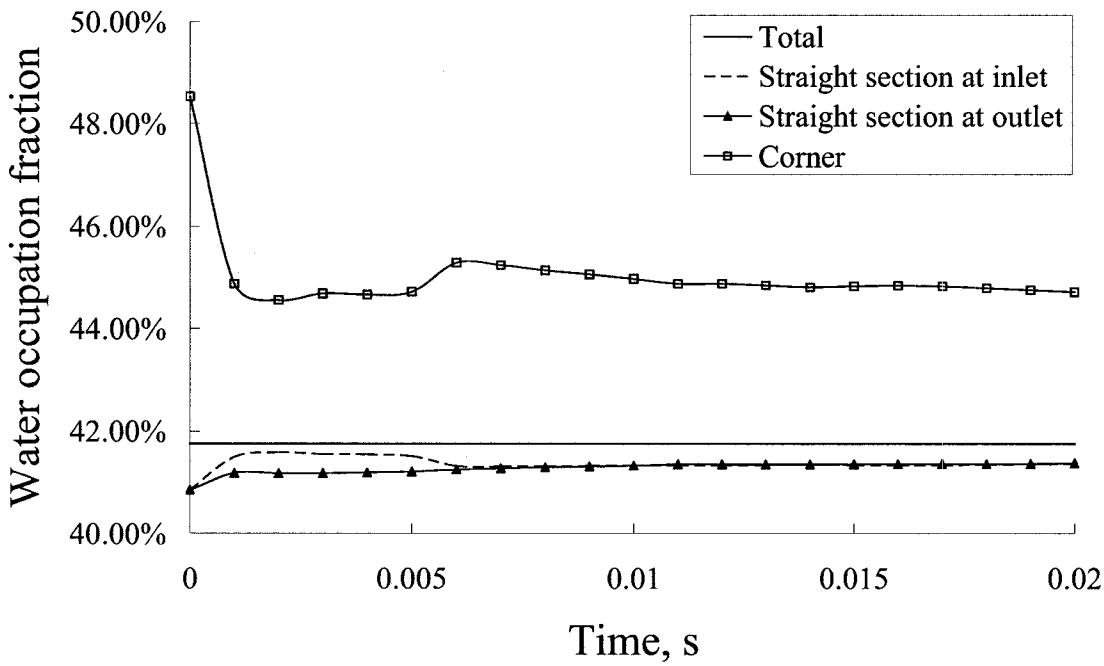

Fig. 60. Water occupation fraction inside the MEA for Case 2.

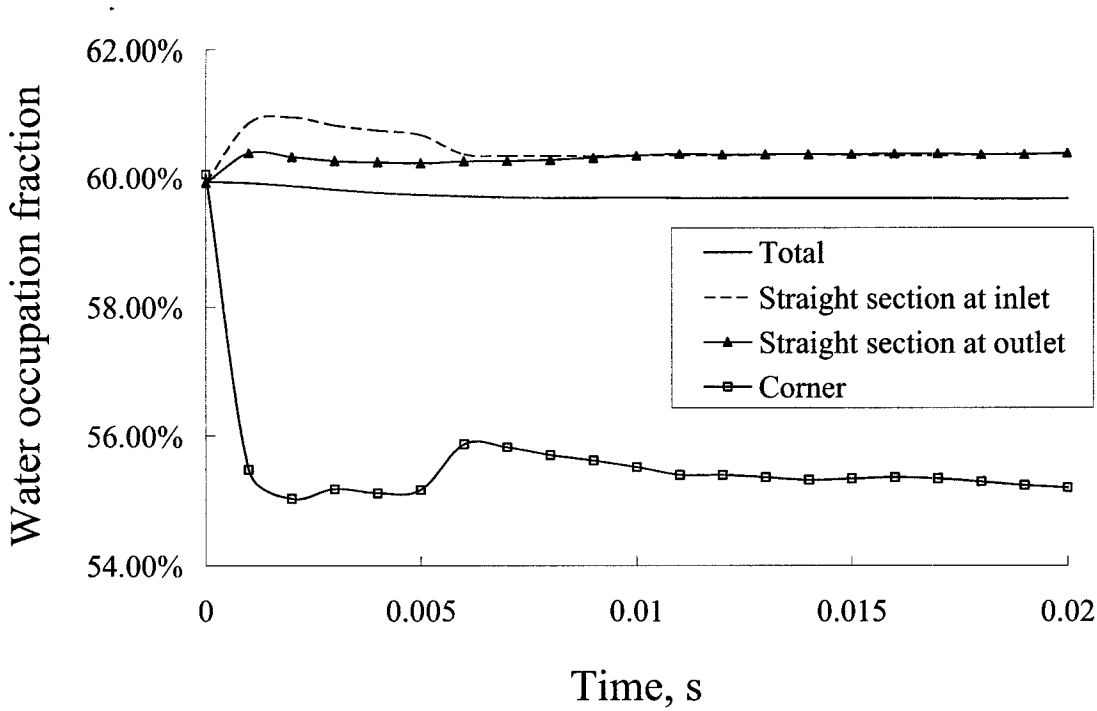

Fig. 61. Water occupation fraction inside the catalyst layer for Case 2.

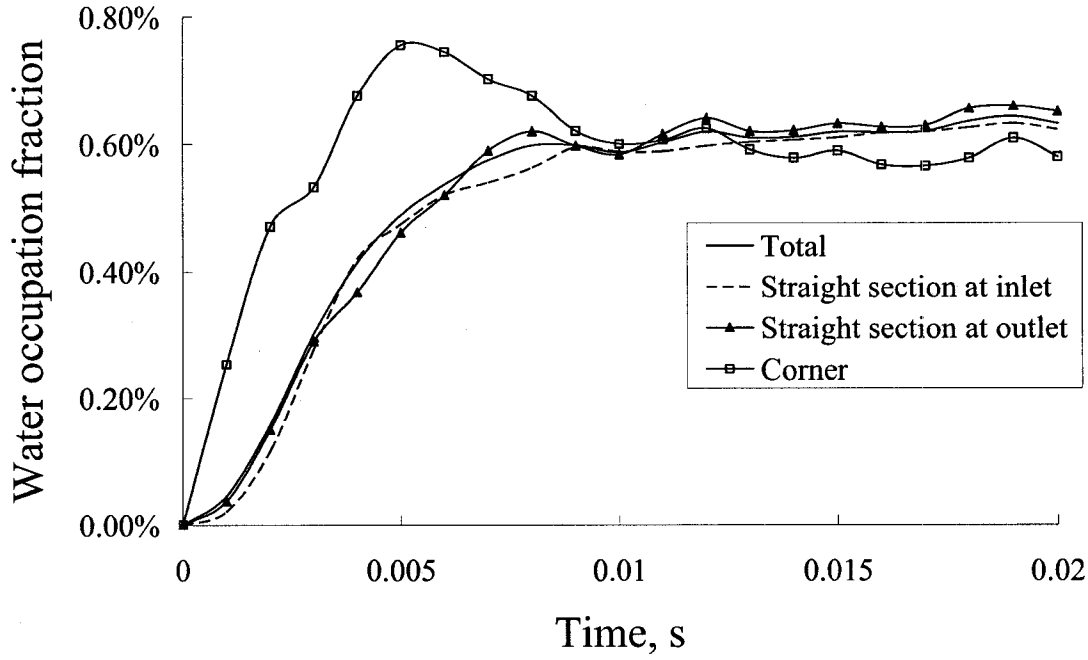

Fig. 62. Water occupation fraction inside the GDL for Case 2.

As mentioned, in comparison with cubic porous holes, the trapeziform micro-structure (with the minimum area facing the catalyst layer) results in a weaker air flow inside the catalyst layer. The water removal ability of such GDL is not acceptable. However, the general flow phenomena are not affected by changing the micro-structures of the GDL.

6.3 Case 3: Water films with a thickness of 0.03 mm placed on membrane/catalyst layer for computation domain 3

This case was simulated to investigate the effects of the GDLs with trapeziform micro-structures on liquid water flow behaviour. The trapeziform porous holes in computation domain 3 (Fig .6d) had a height of 0.1 mm along the z-direction with the minimum area (0.1 × 0.1 mm along the x- and y- directions) facing the gas flow channel. As shown in

Fig. 13, water films with a thickness of 0.03 mm were placed on the membrane/catalyst layer in computation domain 3. The rupture of water films, change of water amount in the MEA, and water transport inside the MEA were studied. Comparison between the three different micro-structures of GDL was also discussed.

6.3.1 Rupture of water films

The general water transport behaviour in this case was similar to Cases 1 and 2. From Fig. 63, the rupture of water films also started from the corner and the inlet. However, after the rupture process was complete the balance between air and water was achieved. The residual water would also tend to stay around the walls in the catalyst layer and connect to the both ends of the catalyst layer. Stronger secondary flow was also observed at the downstream of the corner, as shown in Fig. 64. The only difference between the first three cases is the micro-structures of the GDL. Therefore, it could be concluded that the effects of the micro-structures of the GDL on general liquid water transport serpentine unit cells are insignificant.

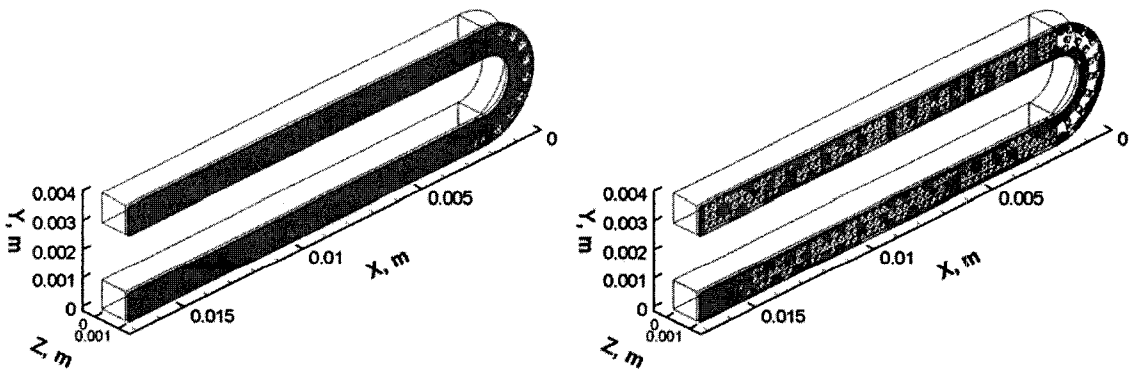

(a) (b)

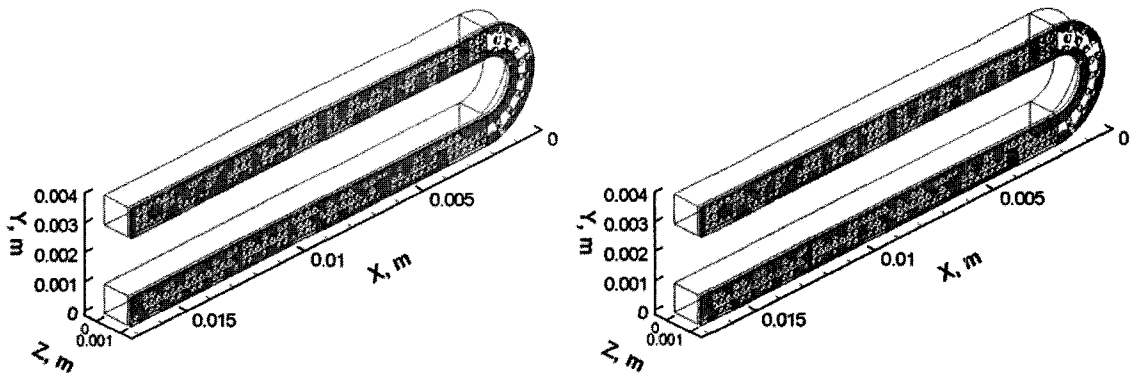

(c) (d)

Fig. 63. Rupture of water films in 3-D view for Case 3.

(a: t = 0.0002 s; b: t = 0.005 s; c: t = 0.01 s; d: t = 0.02 s)

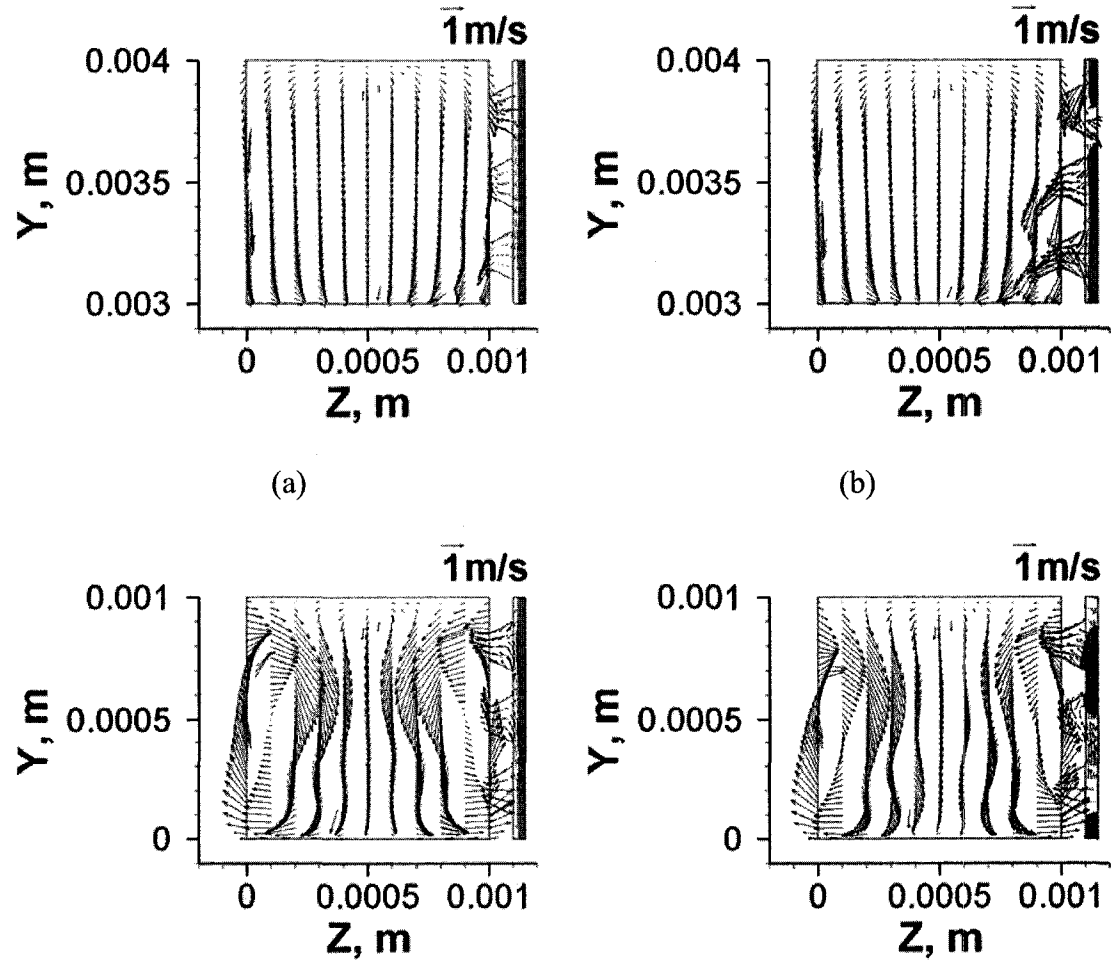

(c) (d)

Fig. 64. Water distribution and velocity field on the plane at x = 0.00205 m in both inlet and outlet sections for Case 3.

(a: t = 0.0001 s at inlet section; b: t = 0.0005 s at inlet section; c: t = 0.0001 s at outlet section; d: t = 0.0005 s at outlet section)

However, by observing these figures, a difference in the water amount left could be noticed. The amount of water left in Case 3 was significantly lower than in Cases 1 and 2, Even though the general flow patterns were similar, the flow behaviours of liquid water across the GDL were different i.e. the water removal abilities of different GDLs are different. Fig. 65 shows the liquid water distribution and velocity fields on the center-plane in the outlet straight section. It was observed that during the rupture process, liquid water was separated into small pieces, which was significantly different from Case 2.

As discussed in Case 2, the air flow from the porous holes was relatively localized and the air streams from these holes were not affecting each other. Consequently, the air streams were not strong enough to separate liquid water into small pieces. In this case, the maximum areas of the porous holes were facing the catalyst layer, as shown in Fig. 64. Such flow resulted in air flowing through the porous holes and spreading rather than concentrating into the catalyst layer. Therefore, air streams from the porous holes would flow to each other and produce stronger air flow, which could facilitate breaking up the water films.

From Fig. 65, the water film was deformed and then broken up. The small pieces of liquid water suffered air flows from its surrounding holes and they were compressed by those air flows. As those pieces of liquid water were compressed, they would move across the only path, which are the porous holes between the surrounding holes. Therefore, liquid water flowed across these holes into the gas flow channel. However, water was still not fully flowing out of the MEA. The water was not only left around the end walls but also between the porous holes. As discussed in Case 1, the liquid water had difficulties to stay between the porous holes. However, if the balance between the surrounding air flows could be achieved, such conditions would still be possible.

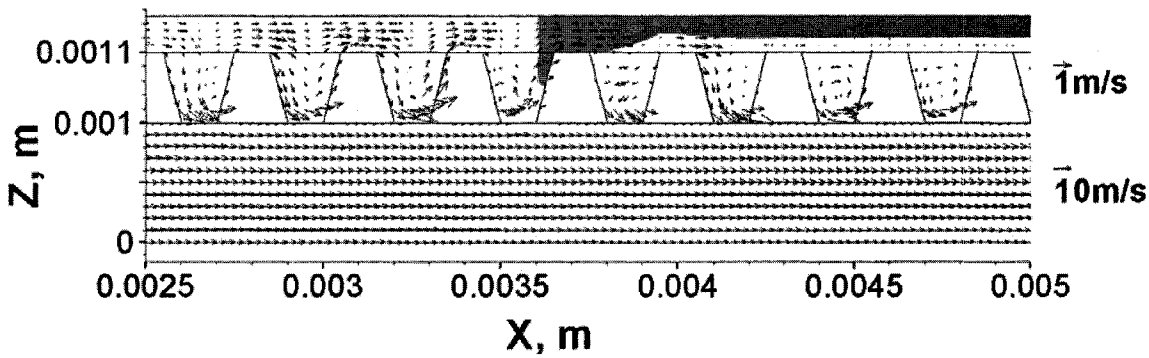

(a)

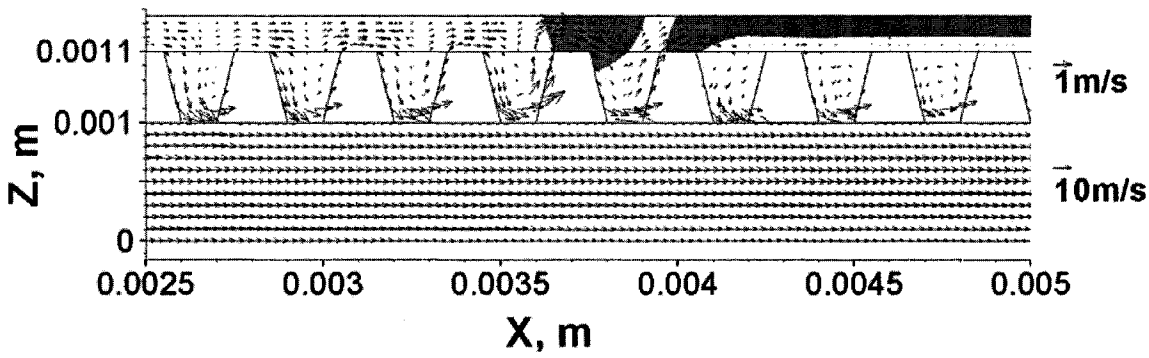

(b)

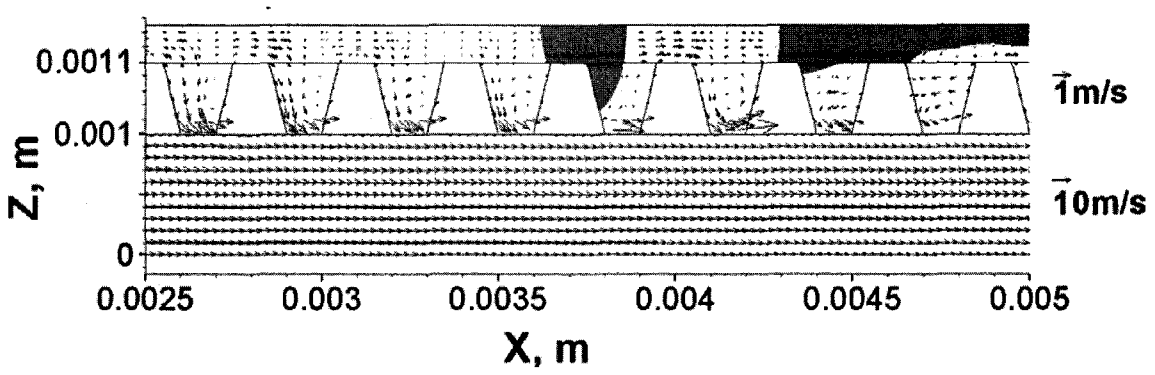

(c)

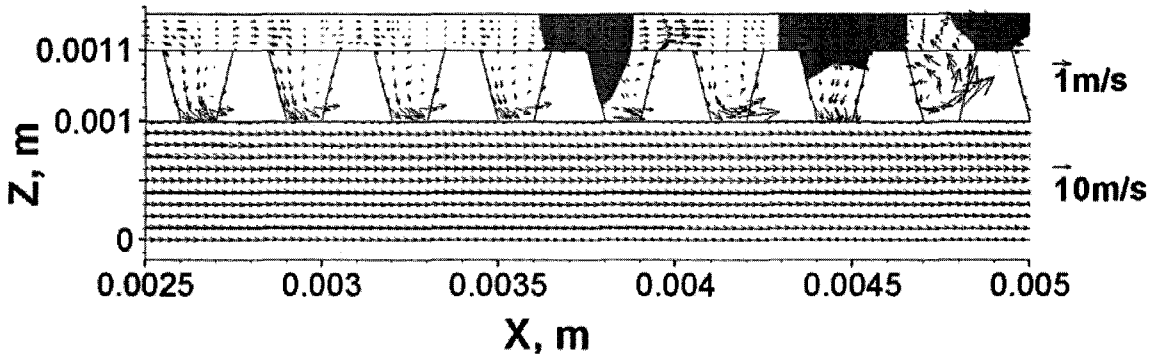

(d)

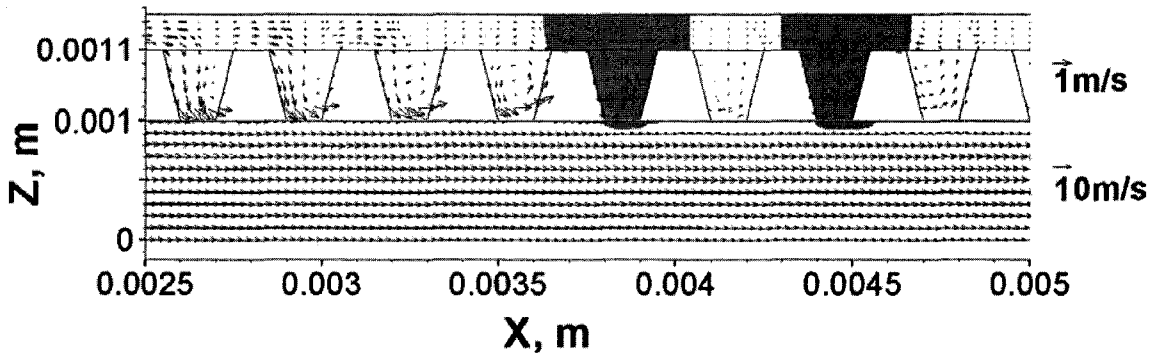

(e)

Fig. 65. Water distribution and velocity field on the center-plane (y = 0.0005 m) in outlet section for Case 3.

(×2 magnification along the z-direction for the MEA, ×3 minification along the z-direction for the flow channel) (a: t = 0.0012 s; b: t = 0.0013 s; c: t = 0.0019 s; d: t = 0.002 s; e: t = 0.003 s)

Fig. 66 shows the liquid water distribution and velocity fields on the center plane of the straight section at the inlet. As the water film was broken up, similar to the situation shown in Fig. 65, small pieces of liquid water were formed. The difference in this condition is that the small pieces of liquid water surrounding holes were next to each other without any hole between them. While the liquid water was compressed, it had no path to flow through. In such conditions, two results were observed. One was as shown in Figs. 66a, 66b and 66c while the other is presented in Figs. 66d and 66e. From Figs. 66a to 66c, there was a small piece of liquid water on the left hand side between two porous holes. It was compressed and then disappeared. This is because the flow from the liquid water's surrounding holes was not balanced and the liquid water flowed along the strongest air flow to another place. From Fig 66d and 66e the balance between those holes was achieved. There was a piece of liquid water between two porous holes which did not move because the forces from the surrounding holes were balanced. From the first three cases, Case 3 had the least amount of water between the holes because the air flow was the strongest in this case.

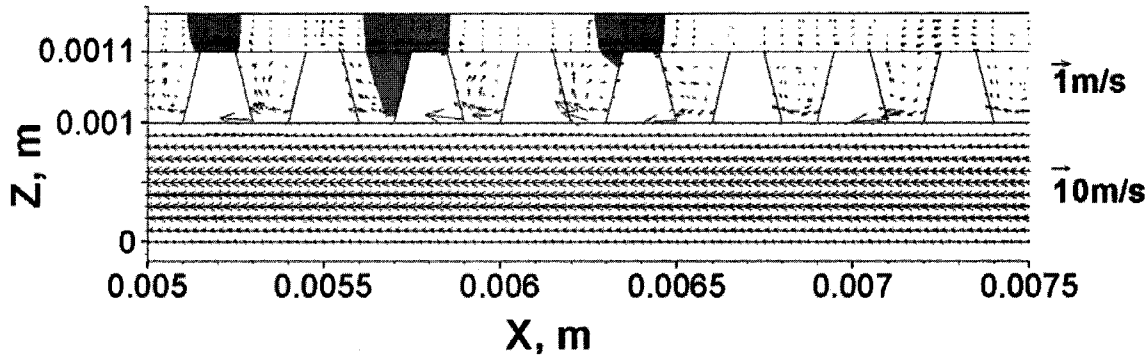

(a)

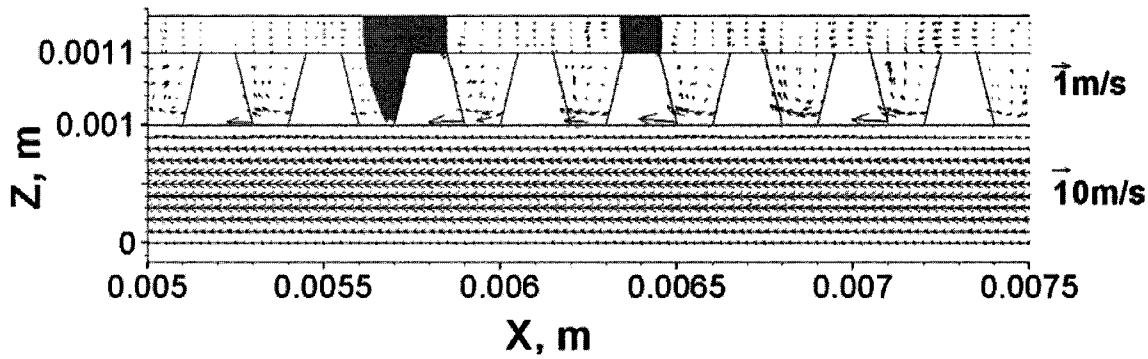

(b)

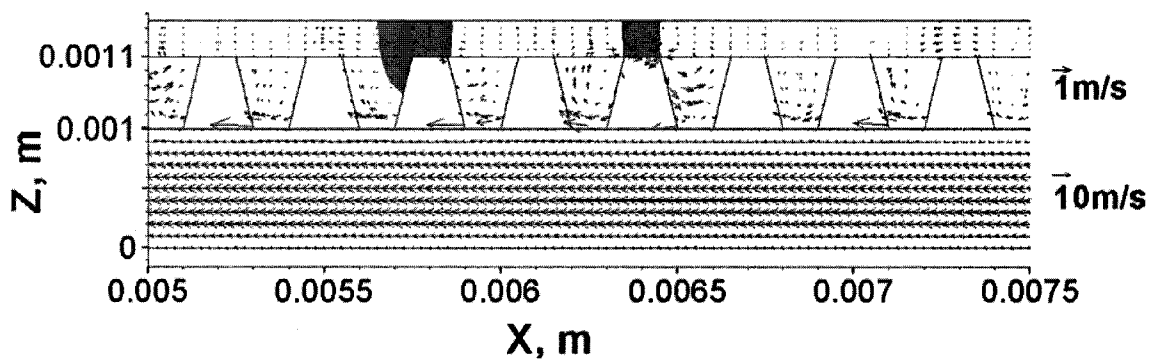

(c)

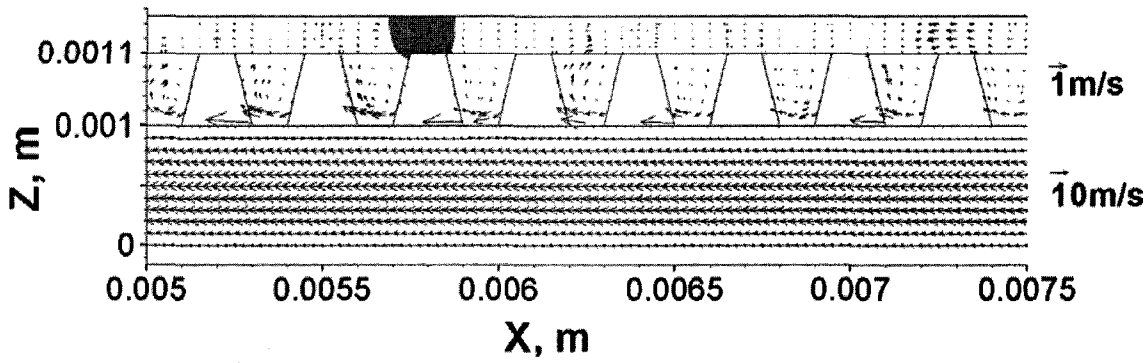

(d)

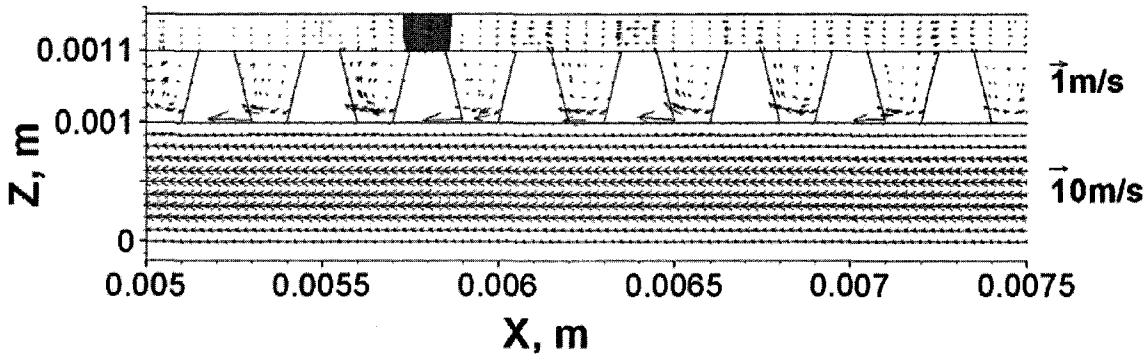

(e)

Fig. 66. Water distribution and velocity field on the center-plane (y = 0.0035 m) in inlet section for Case 3.

(×2 magnification along the z-direction for the MEA, ×3 minification along the z-direction for the flow channel) (a: t = 0.0045 s; b: t = 0.005 s; c: t = 0.006 s; d: t = 0.007 s; e: t = 0.02 s)

6.3.2 Water occupation fraction variation

Figs. 67, 68 and 69 show the water occupation fraction inside the MEA, catalyst layer and GDL respectively. In contrast to the first two cases, the straight sections achieved better water removal than the corner in both the catalyst layer and the GDL. Even though it has been shown that the secondary flow around the corner was still stronger than at the

straight sections, the different kinds of micro-structures of the GDL could still enhance water removal ability significantly resulting in better water drainage at the straight sections than at the corner. Similar water occupation fraction variations were also observed. The straight section at the outlet achieved better water removal than at the inlet, and when the balance was achieved, the variations became almost constant.

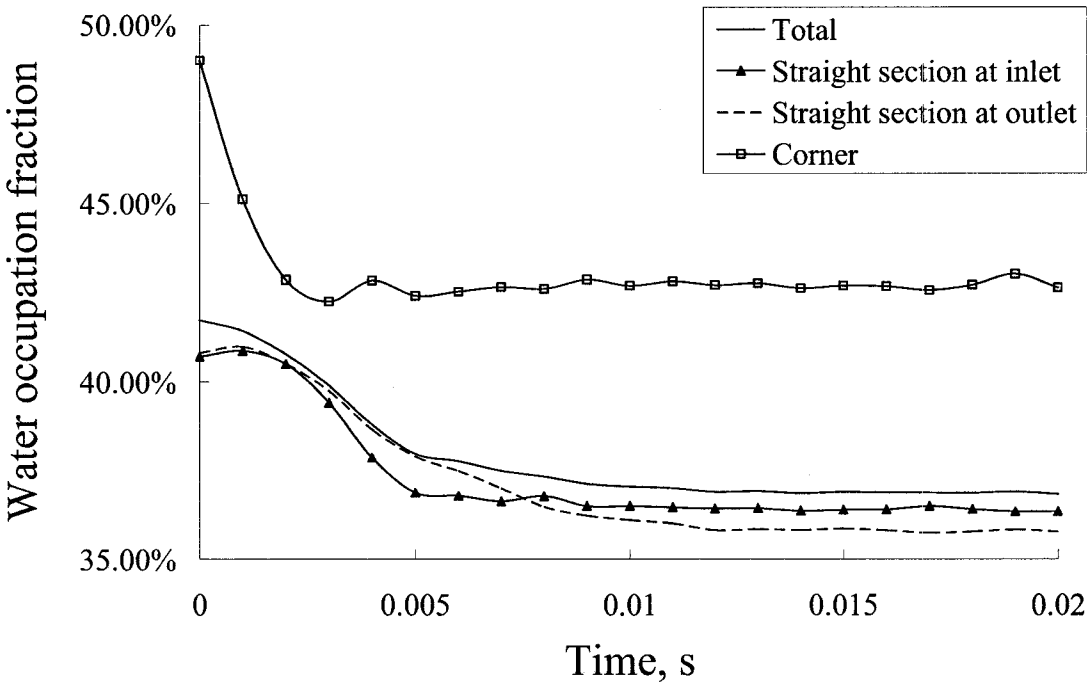

Fig. 67. Water occupation fraction inside the MEA for Case 3.

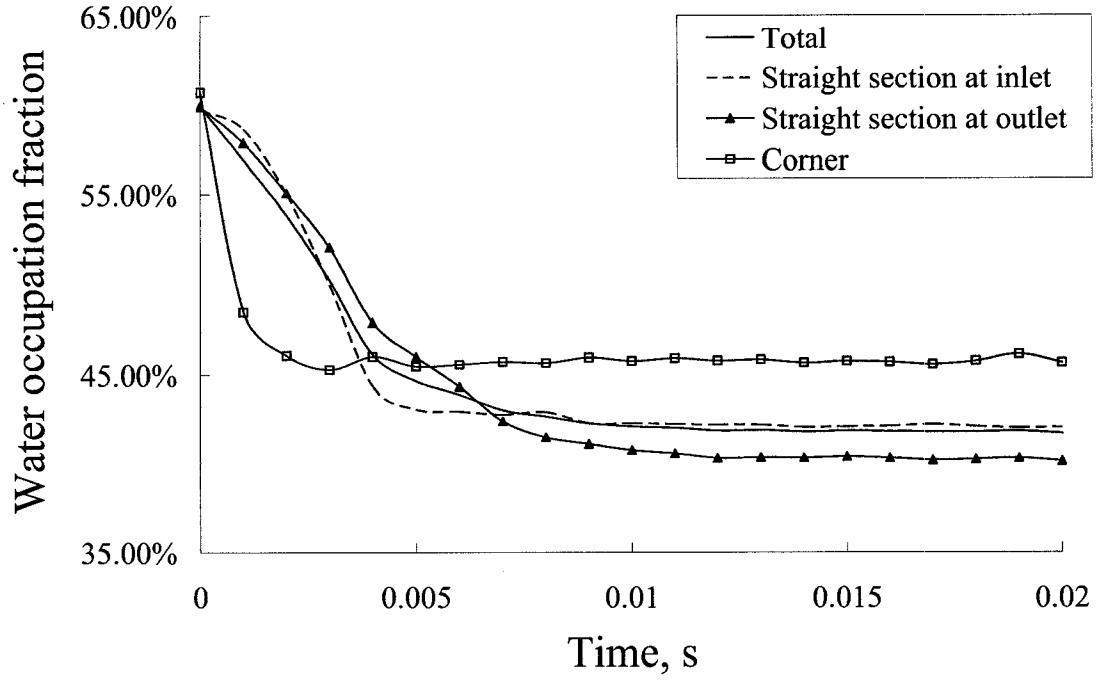

Fig. 68. Water occupation fraction inside the catalyst layer for Case 3.

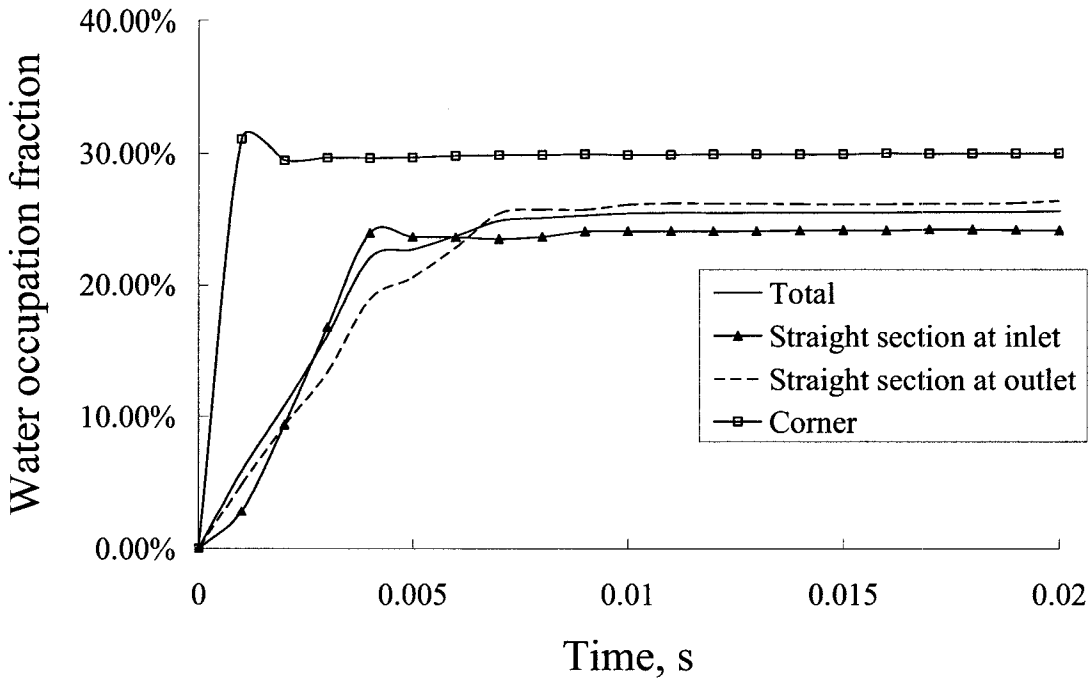

Fig. 69. Water occupation fraction inside the GDL for Case 3.

6.3.3 Comparison of different micro-structures of GDL

Figs. 70 and 71 show the comparison of the water amount variation inside the MEA and the catalyst layer for the three cases. From the figures, Case 3 showed increased water-removal ability than the other two cases. As mentioned, the only difference between the three cases was the micro-structures of the GDL. Because of its ability to enhance the air flow inside the catalyst layer, the trapeziform porous holes with the minimum area facing the gas flow channel could achieve the best water drainage. The worst condition was when the air flow inside the catalyst became weak i.e. when the trapeziform porous holes with the minimum area facing the catalyst layer. Therefore, the key factor to design the GDL is trying to enhance the air flow inside the catalyst layer. Even though Case 3 achieved the best water drainage, the amount of water inside the GDL in Case 3 was the

largest, seen from Fig. 72. As discussed above, liquid water was compressed by its surrounding air flows to flow through the porous holes into the gas flow channel. However, the main flow stream inside the gas flow channel was another external force exerted on the liquid water. Therefore, the balance between air and water could be achieved inside the porous holes and thus the water would stay inside the porous holes without going elsewhere as observed in Fig. 65. This could explain why Case 3 had the largest amount of water inside the GDL.

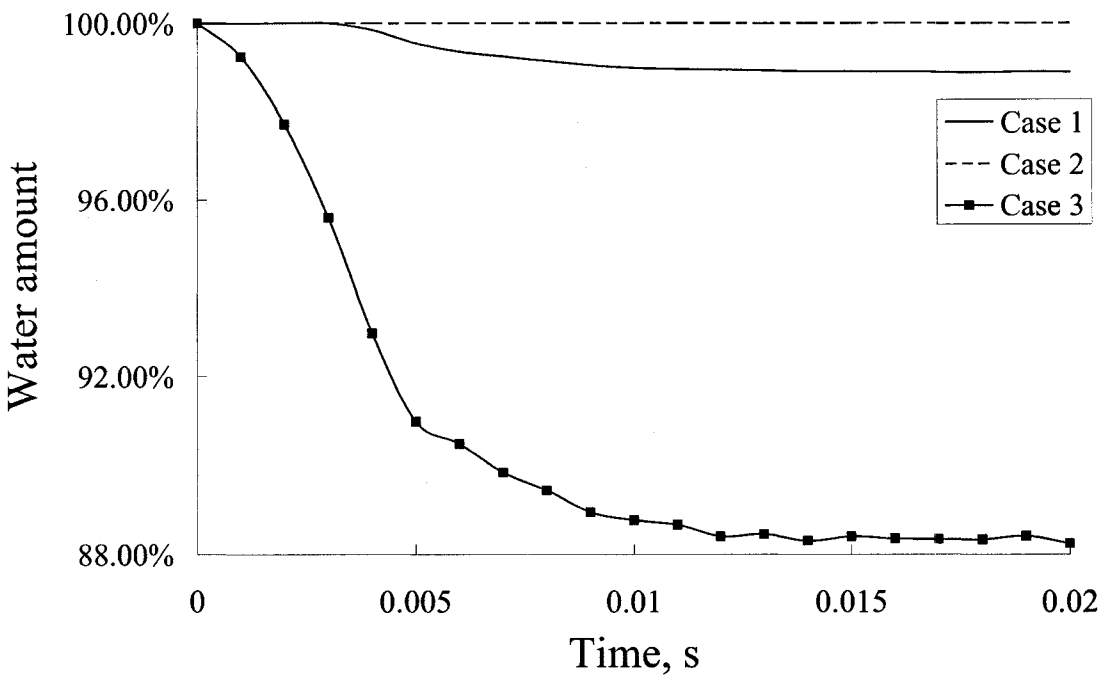

Fig. 70. Water amount variation inside the MEA for the three cases.

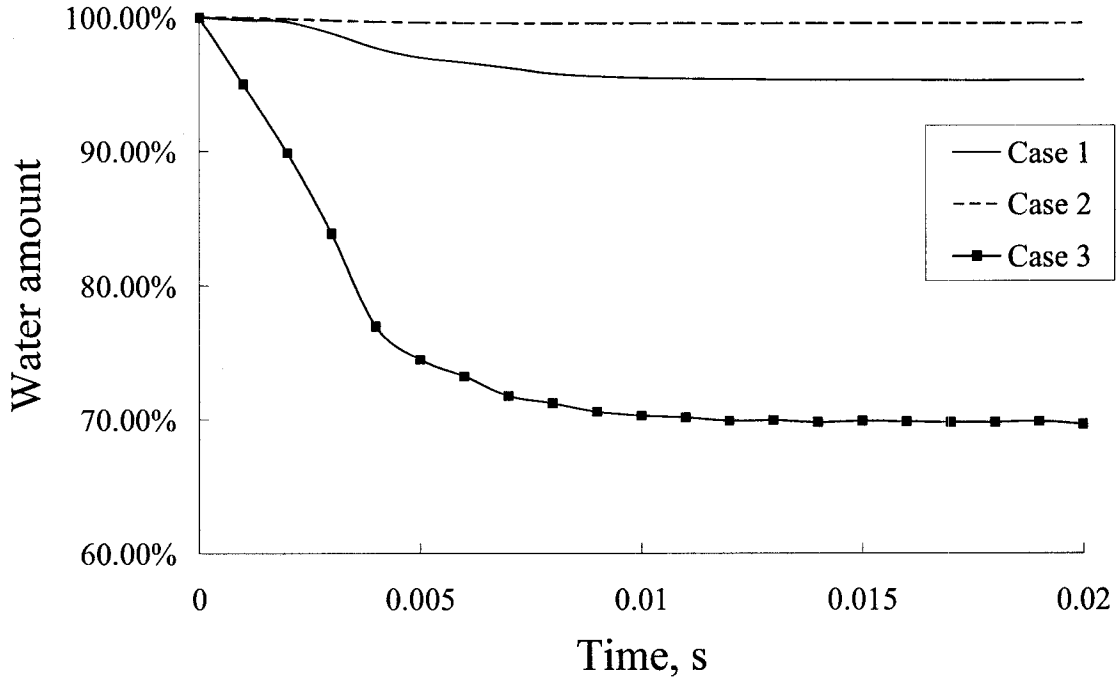

Fig. 71. Water amount variation inside the catalyst layer for the three cases.

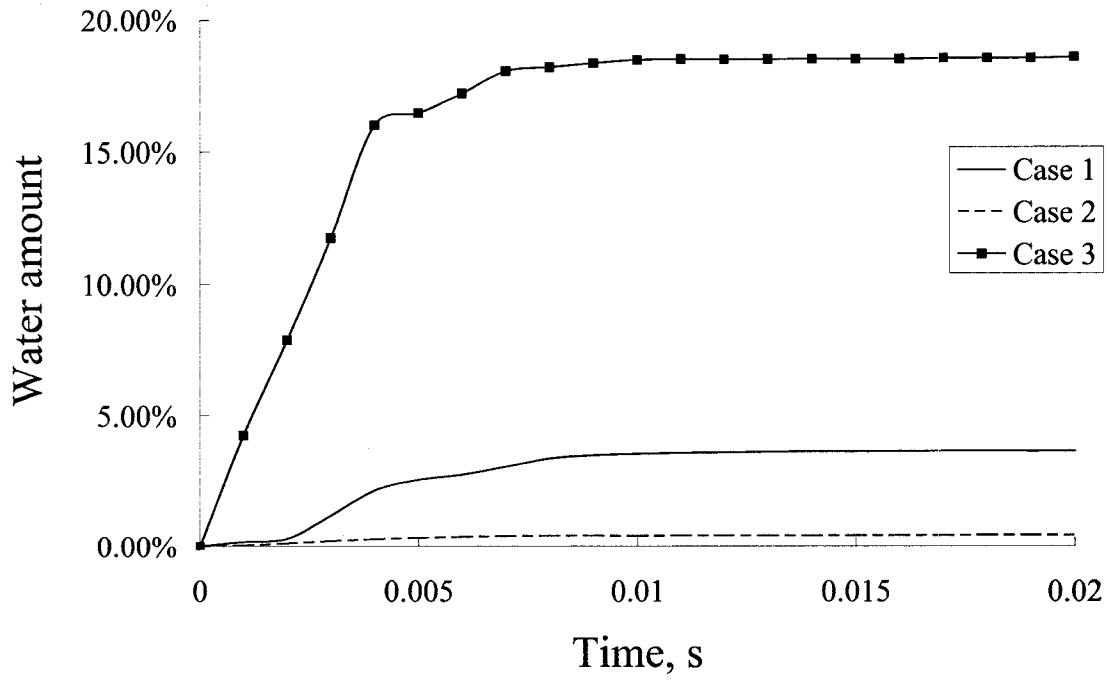

Fig. 72. Water amount variation inside the GDL for the three cases.

CHAPTER 7

ANALYSIS OF RESULTS – TOPIC 4

7.1 Case 1: Water films with a thickness of 0.03 mm placed on catalyst layer with hydrophilic GDL

The first case was simulated to investigate the effects of the hydrophilic GDL (computation domain 3 shown in Fig. 6d) on liquid water flow behaviour. As shown in Fig. 13, and listed in Table 4, water films with a thickness of 0.03 mm were placed on catalyst layer with hydrophilic GDL. The rupture of water films, and water transport across the GDL were studied.

7.1.1 Formation of liquid water "mesh"

Fig. 73 shows the liquid water distribution in 3-D view. At t = 0.0002s (Fig. 73a), water film started rupturing from the corner to the straight sections. Such water film rupture process is similar as mentioned in Topic 3 (Chapter 6), which has concluded that the process is due to the stronger secondary flow at the corner. It could also be noticed that, at t = 0.01 s (Fig. 73b), the initially attached liquid water film ruptured into liquid water "mesh". As time passed, more parts of the "mesh" ruptured (Figs. 73c and 73d). However, most of the liquid water "mesh" remained until t = 0.02 s (Fig. 73d). The reason that such liquid water "mesh" formed could be explained with help of Fig. 74, which shows the cross section at x = 0.00805 in the lower section (outlet) of the computation domain. At t = 0.001 s (Fig. 74a), the initially attached flat water films were in wave-form, and then, at t = 0.0015 s (Fig. 74b), the force balance between air and liquid water was broken, more air started flowing into the electrode and the water film was broken up. After a period of time, at t = 0.002 s (Fig. 74c), the water films were broken up into four parts – between

the holes of the GDL, and the two sides of the holes. Therefore, as shown in Figs. 73 and 74, the liquid water "mesh" had its void area under the holes, and its liquid water between the holes. Another force balance between air and liquid water was achieved at that time, and later these parts of water did not move to anywhere else (Fig. 74d). This is because these parts of water were sticking on both the surface of the catalyst layer and the bottom surface of the GDL. However, it has been concluded in Topic 3 (Chapter 6), this GDL has significant effect on breaking up liquid water between the holes. The reason that such effect was not observed in this case is due to the hydrophilic property of the GDL. As mentioned, these parts of water also stick on the surface of the GDL, which provided more significant wall adhesion effect. Therefore, these parts of liquid water become harder to be removed, and even the GDL could provide strong air flow between the holes, the force balance was still achieved. However, some parts of the liquid water "mesh" could still be broken up, as shown in Fig. 73. Figs. 75a and 75b show a clearer view on such process, it could be observed that some parts of the liquid water between the holes were flowed away. Based on the water flow behaviours that described in this section, it could be concluded that, hydrophilic GDL could provide more significant wall adhesion effect on liquid water in catalyst layer, thus preventing liquid water flowing out, which is not good for PEM fuel cell operation.

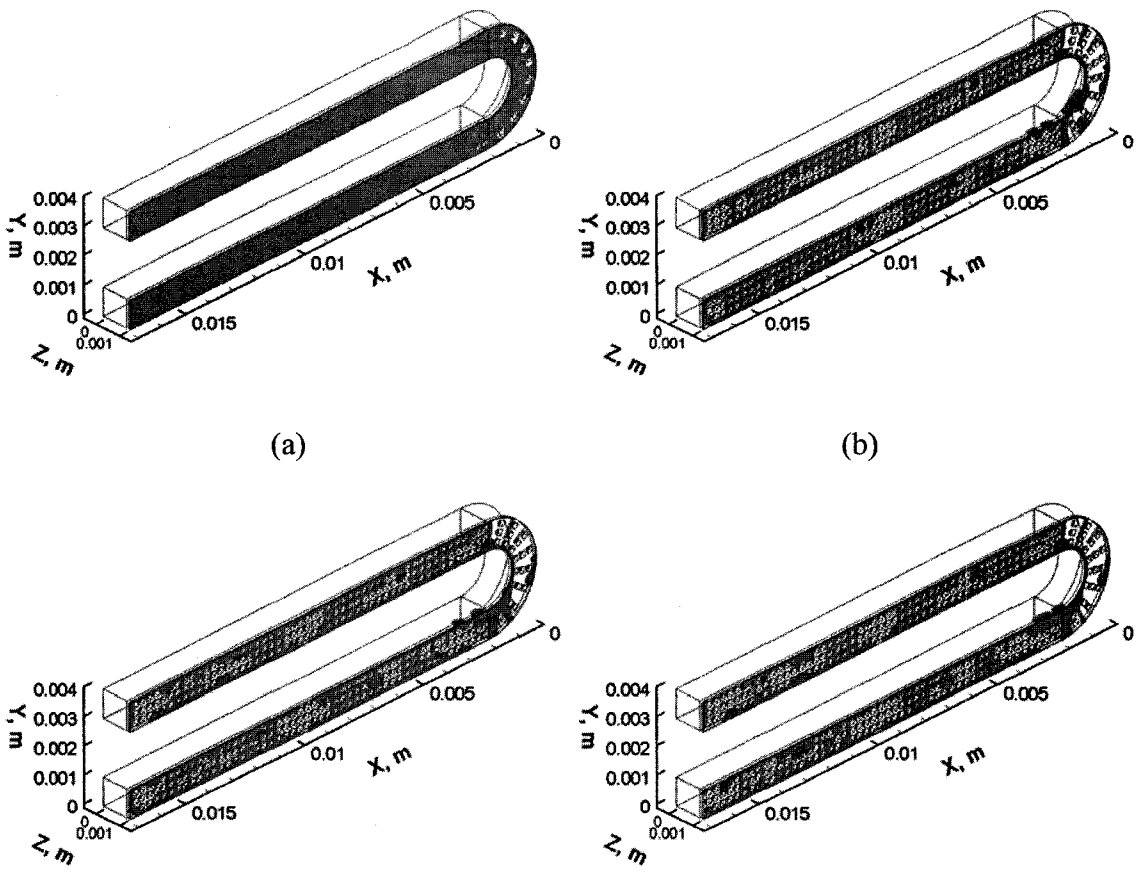

Fig. 73. Liquid water distribution in 3-D view for Case 1.

(a: t = 0.0002 s; b: t = 0.01 s; c: t = 0.015 s; d: t = 0.02 s)

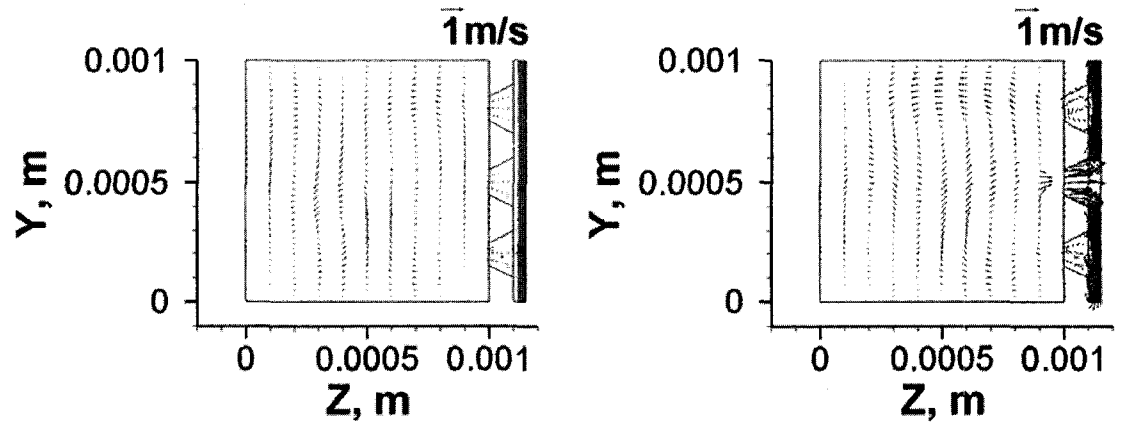

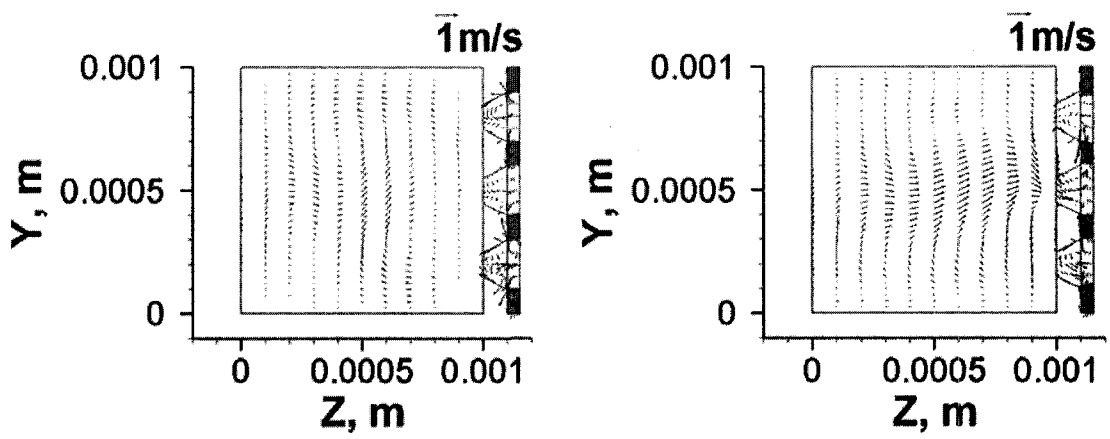

(c) (d)

Fig. 74. Water distribution and velocity field on the plane at x = 0.00805 m in outlet section for Case 1.

(a: t = 0.001 s; b: t = 0.0015 s; c: t = 0.002 s; d: t = 0.02 s)

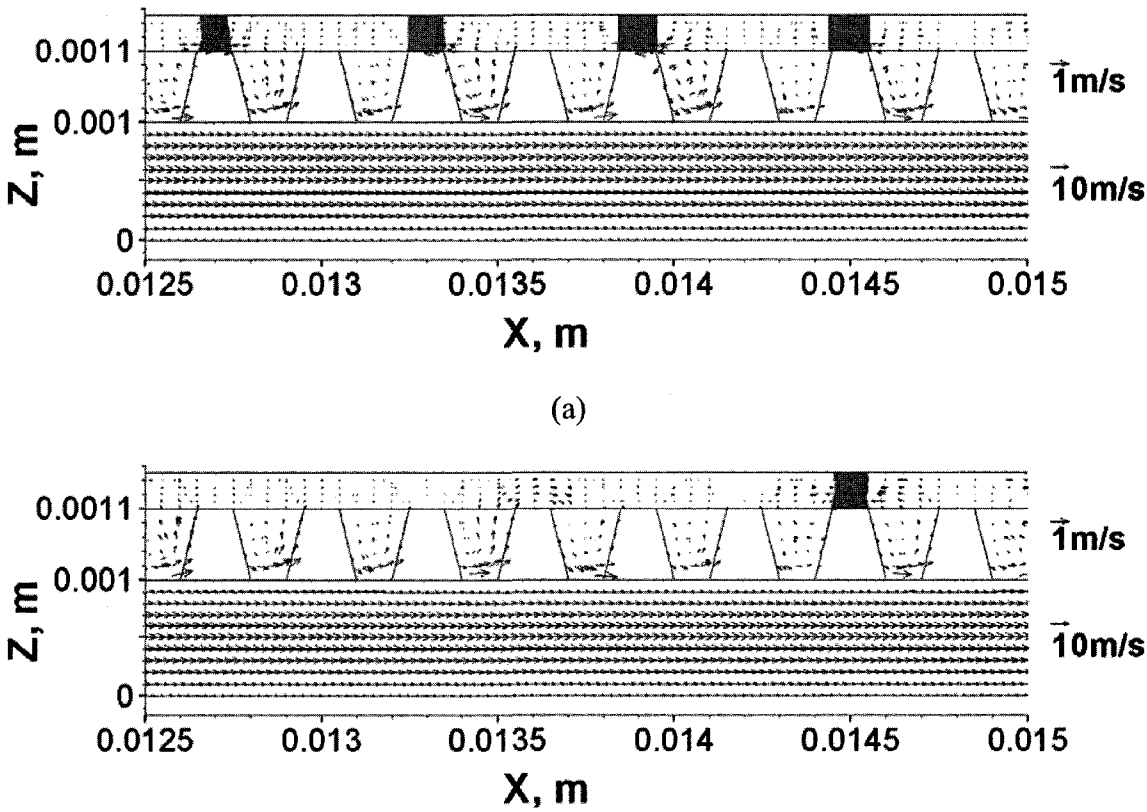

(b)

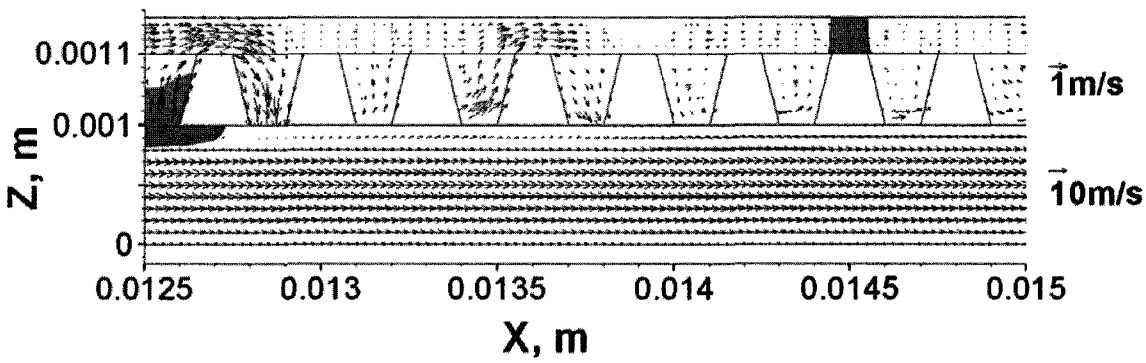

(c)

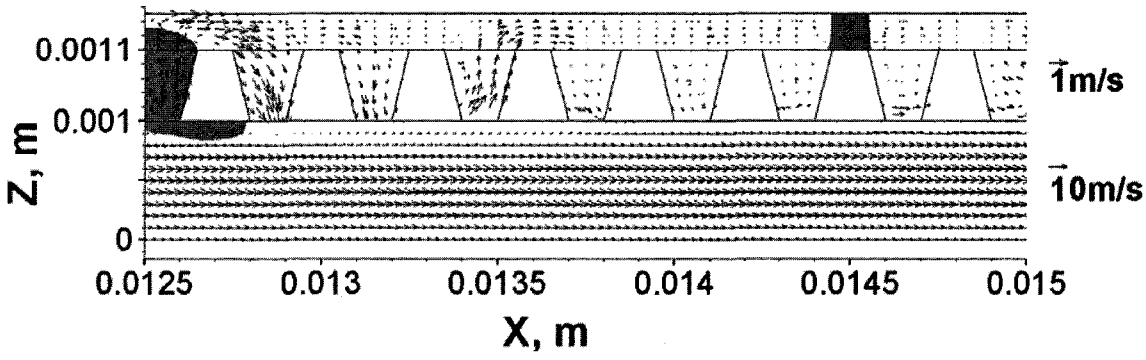

(d)

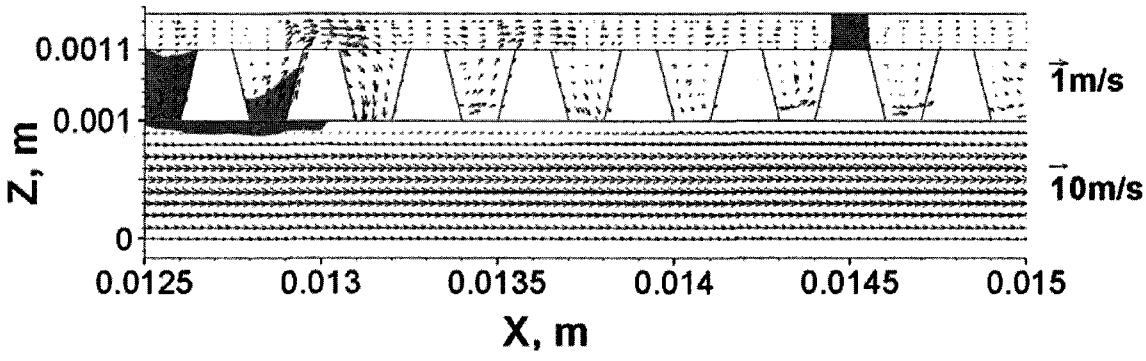

(e)

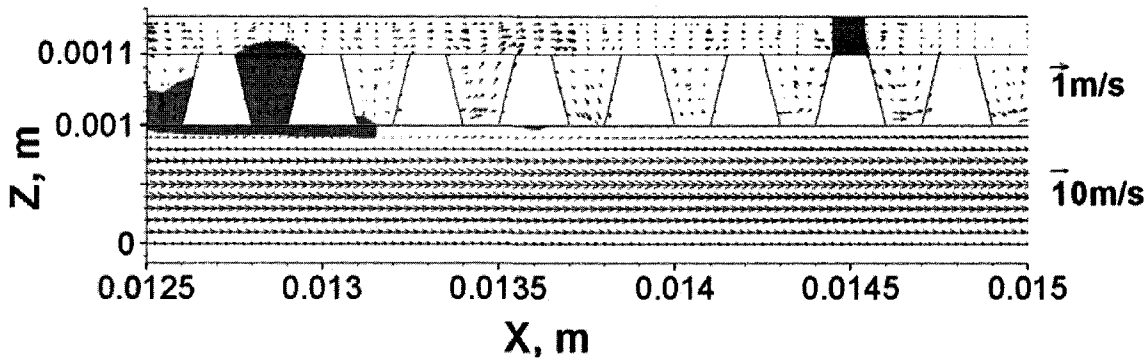

(f)

Fig. 75. Water distribution and velocity field on the center-plane (y = 0.0005 m) in outlet section for Case 1.

(×2 magnification along the z-direction for the electrode, ×3 minification along the z-direction for the flow channel) (a: t = 0.01 s; b: t = 0.016 s; c: t = 0.019 s; d: t = 0.0192 s; e: t = 0.0195 s; f: t = 0.02 s)

7.1.2 Back flow of liquid water

Even the liquid water "mesh" was formed in the catalyst layer, some parts of the water still flowed out of the electrode. Fig. 75 shows the center plane (y = 0.0005 m) of part of the lower straight section of the computation domain. At t = 0.019 s (Fig. 75c), some liquid water from the upstream could be observed. It should be noticed that, the coming water did not leave the surface of the GDL. This is because of the strong wall adhesion effect of the GDL surface, as discussed before. As the water flowed along the GDL surface, when it reached the holes of the GDL, due to the strong wall adhesion effect, some of the water still flowed along the surface of the GDL – some water flowed back into the holes, as shown in Fig. 75. When one of the holes was filled with some water (Fig. 75e), other parts of water could then "jump" that hole to the next, and similar liquid

water flow behaviours could be observed in the next hole – some water flowed in, some water "jumped". As shown in Figs. 75d, 75e and 75f, some of the water flowed across the GDL into the catalyst layer, and then flowed out again and into the next hole. As mentioned, the main reason that such flow was observed is due the hydrophilic property of the GDL (strong wall adhesion effect). Even some of the water could be removed into the gas flow channel, however, the water could not be removed from the surface of the GDL. Such process increased the chance for the liquid water flowing into the electrode, and such back flow of liquid water is not good for PEM fuel cell operation – it blocks the GDL and the catalyst layer.

7.2 Case 2: Water films with a thickness of 0.03 mm placed on catalyst layer with hydrophobic GDL

The second case was simulated to investigate the effects of the hydrophobic GDL (computation domain 3 in Fig. 6d) on liquid water flow behaviour. As shown in Fig. 13, and listed in Table 4, water films with a thickness of 0.03 mm were placed on catalyst layer with hydrophobic GDL. The rupture of water films, and water transport across the GDL were studied.

7.2.1 Rupture of liquid water film

As shown in Fig. 76, the liquid water film ruptured into different pieces. The void and flooding areas are clearly separated, and the liquid water occupied both the area under the holes and between the holes of the GDL, this is dissimilar to Case 1, which most water stayed between the holes and formed "mesh". Figs. 77 and 78 show the water distribution

and velocity field on the y-z planes for both the flooding area and void area, respectively. For the flooding area (Fig. 77), the flat water film became in wave-form first (Fig. 77a), and then, more water flowed into this flooding section from other void sections, the water filled the whole catalyst layer and touched the surface of the GDL (Fig. 77b). As time passed, at t = 0.005 s (Fig. 77c), the water already flowed through the GDL and into the gas flow channel. However, the water stopped moving after that, at t = 0.02 s (Fig. 77d), the water distribution still remained the same. This is because the force balance between air and liquid water was achieved. For the void area (Fig. 78), it could be observed that the water film first became in wave-form as well (Fig. 78a), and then broken up by the air flow from the holes of the GDL (Fig. 78b). Figs. 78a and 78b showed very similar water flow pattern as in Case 1, however, when the liquid water was split into small pieces, dissimilar to Case 1, these small pieces of water were flowed away. This is because of the hydrophobic property of the GDL – when the small pieces of liquid water touched the surface of the GDL, the wall adhesion effect was weak and could not hold the water. Therefore, these small pieces of liquid water were flowed into other sections and formed the flooding areas, as discussed with Fig. 77. Generally speaking, the whole process described with Figs. 77 and 78 produced those flooding and void areas.

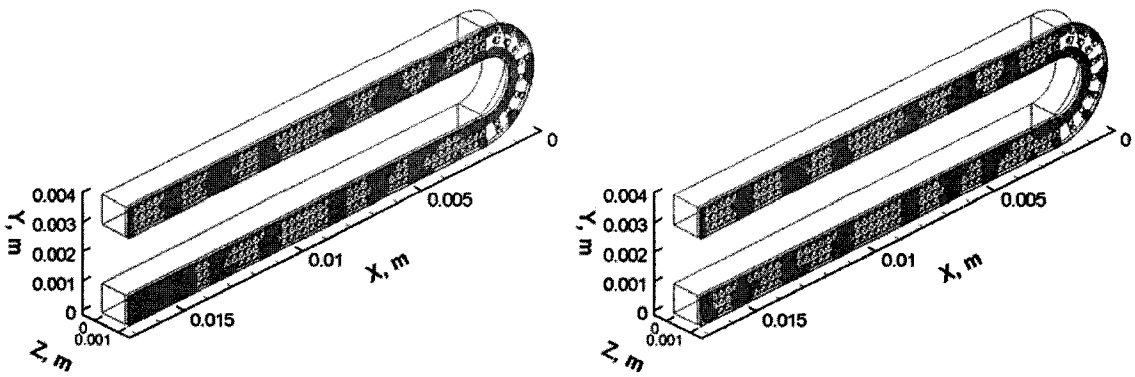

(a) (b)

Fig. 76. Liquid water distribution in 3-D view for Case 2.

(a: t = 0.005 s; b: t = 0.02 s)

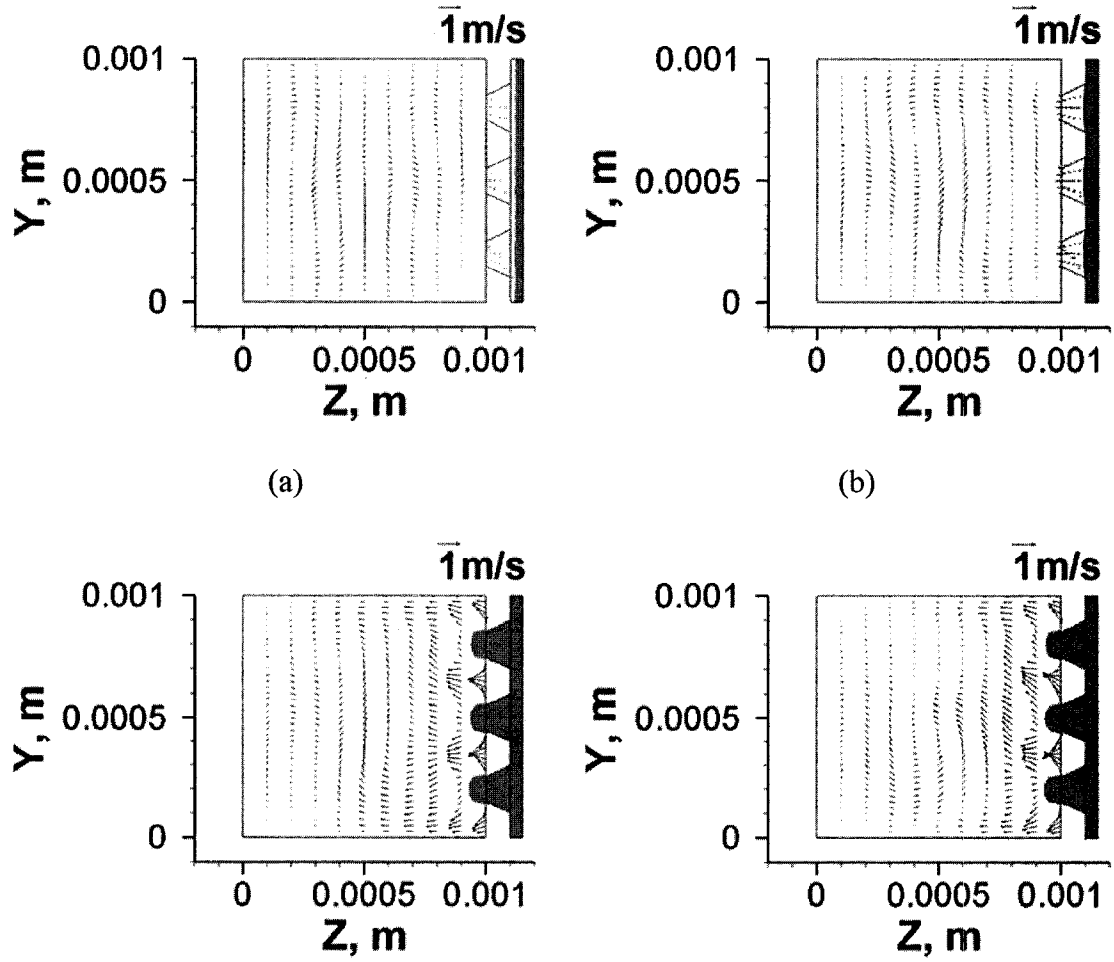

(a) (b)

(c) (d)

Fig. 77. Water distribution and velocity field on the plane at x = 0.00805 m in outlet section for Case 2.

(a: t = 0.001 s; b: t = 0.002 s; c: t = 0.005 s; d: t = 0.02 s)

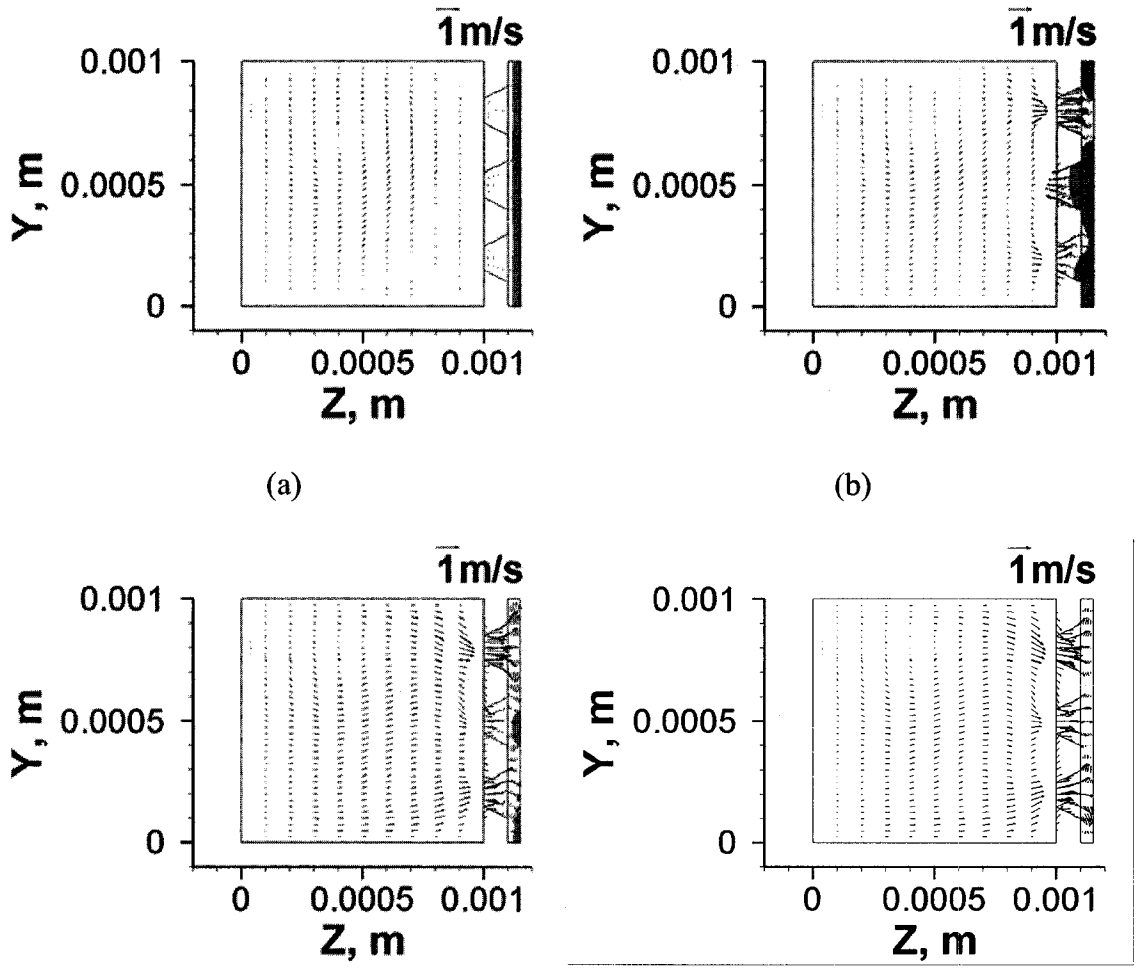

Fig. 78. Water distribution and velocity field on the plane at x = 0.01405 m in outlet section for Case 2.

(a: t = 0.004 s; b: t = 0.0047 s; c: t = 0.0049 s; d: t = 0.005 s)

7.2.2 Force balance across the GDL

As discussed in Case 1, there were small pieces of the liquid water staying between the holes of the GDL, but such water flow behaviour was not observed in Case 2 due to the weak wall adhesion effect of the GDL. However, the weak wall adhesion effect could be enhanced by increasing the contact area between the wall and the liquid water. As shown in Fig. 79, which shows the water distribution and velocity field on the center-plane (y = 0.0005 m) in the lower section of the computation domain. It could be observed that the initially attached water film was broken up, and both the void and flooding areas were formed. As discussed before, after these flooding areas were formed, the water stopped moving. This is because as the flooding area increased, the contact area between the water and the walls also increased, so the wall adhesion effect increased. When the flooding area was large enough, the wall adhesion became strong enough to overcome the air flow, so the flooding water stopped moving. Unfortunately, based on the water flow behaviours described in this section, even the GDL was changed to hydrophobic, the water removal was not apparently improved, a significantly amount of water could still be observed in the catalyst layer, and even more amount of water could be observed in the GDL. Therefore, it could be concluded that, even a hydrophobic GDL could facilitate flowing away some of the water inside the catalyst layer, however, in the meantime, some flooding areas could also be formed, and such flooding area with the increased contact area between water and wall could overcome the air flow and the weak wall adhesion effect, thus stopping the water movement, which is not good for PEM fuel cell operation.

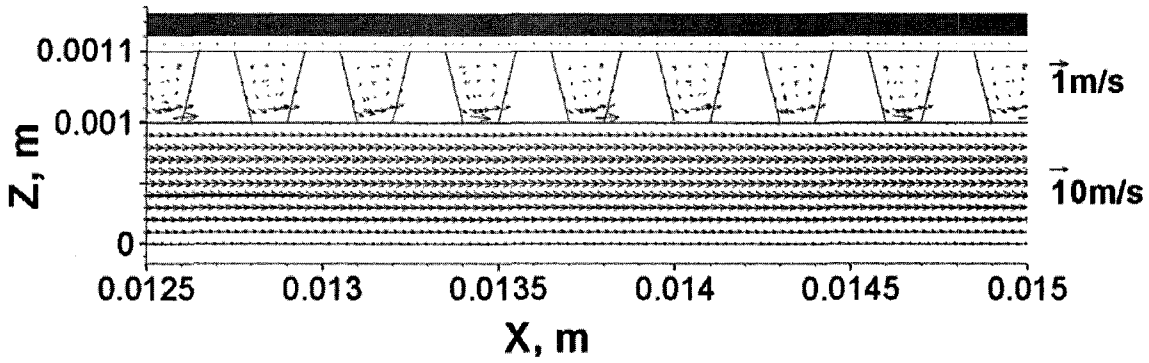

(a)

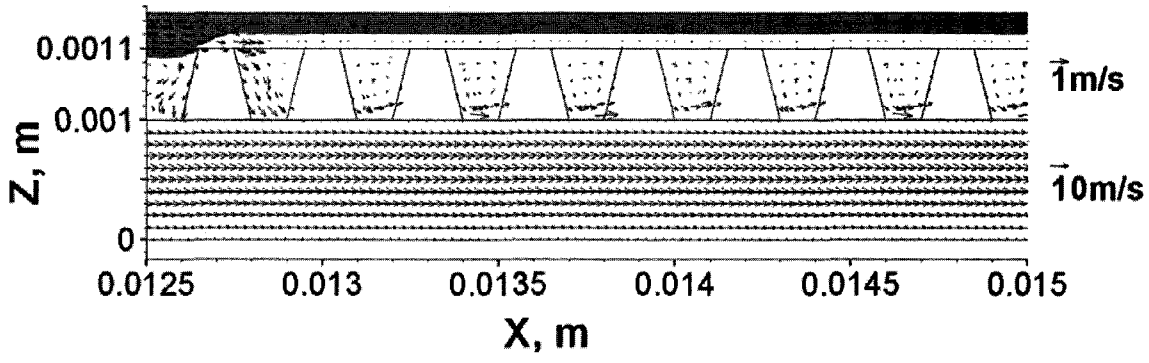

(b)

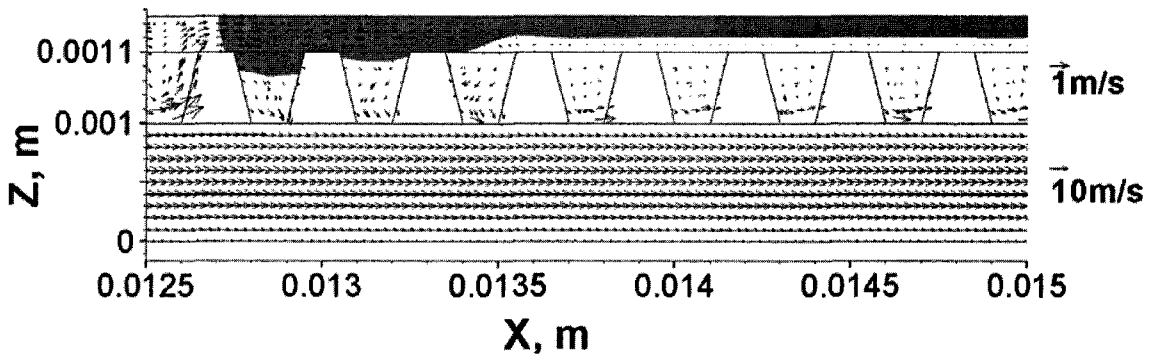

(c)

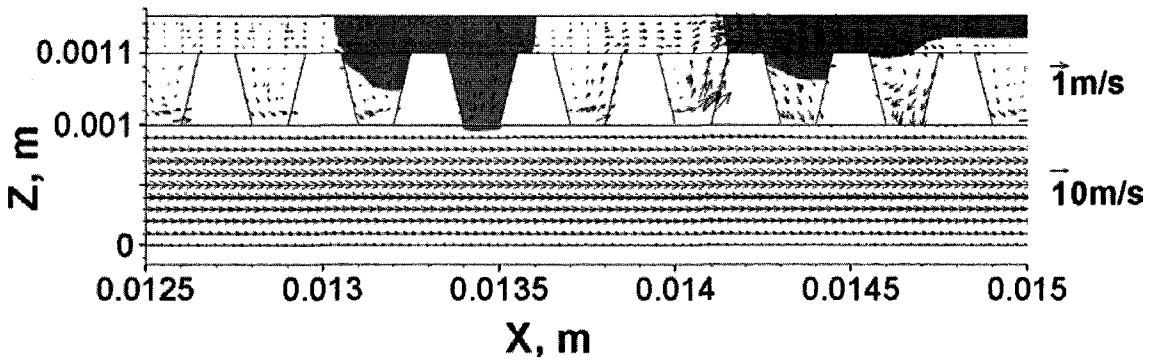

(d)

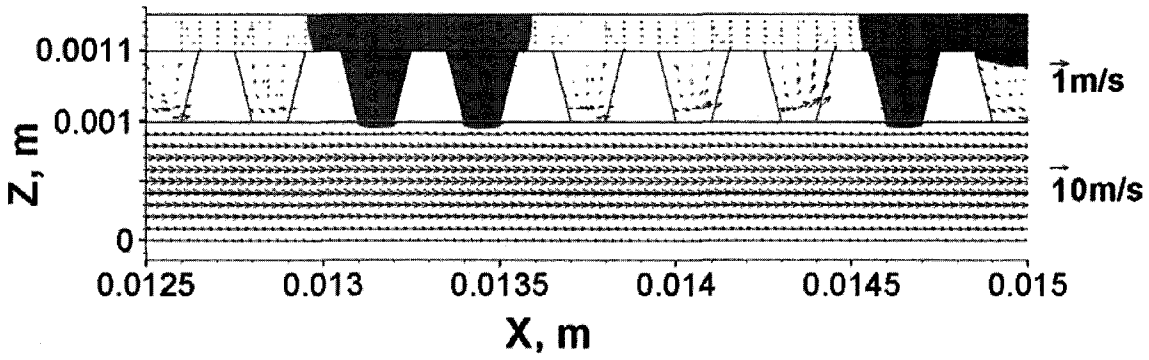

(e)

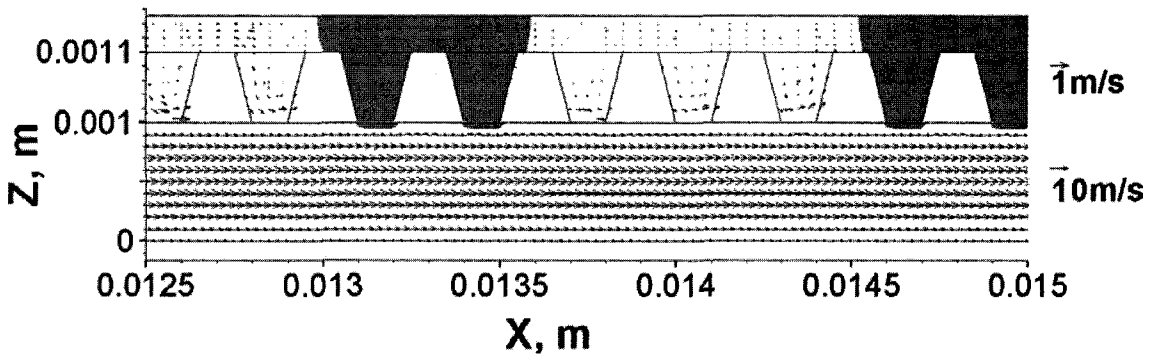

(f)

Fig. 79. Water distribution and velocity field on the center-plane (y = 0.0005 m) in outlet section for Case 2.

(×2 magnification along the z-direction for the electrode, ×3 minification along the z-direction for the flow channel) (a: t = 0.002 s; b: t = 0.003 s; c: t = 0.004 s; d: t = 0.005 s; e: t = 0.006 s; f: t = 0.02 s)

7.3 Case 3: Water films with a thickness of 0.03 mm placed on catalyst layer with hydrophobic electrode (GDL and catalyst layer)

The third case was simulated to investigate the effects of the combination of hydrophobic GDL and hydrophobic catalyst layer on liquid water flow behaviour (computation domain 3 in Fig. 6d). As shown in Fig. 13, and listed in Table 4, water films with a thickness of 0.03 mm were placed on catalyst layer. The rupture of water films, and water transport across the GDL were studied.

7.3.1 Formation of liquid water "string"

Fig. 80 shows the liquid water distribution in 3-D view for Case 3. It could be apparently observed that the water distribution was different from the previous cases. At t = 0.001 s (Fig. 80a), liquid water "strings" were formed along the center line of the main air flow. The water "strings" then started being flowed out of the computation domain, as shown in Fig. 80b, at t = 0.02 s, some parts of the water "strings" were already flowed out. The reason that the water "strings" were formed could be explained with help of Fig. 81, which shows the water distribution and velocity field on the plane at x = 0.00805 m in the

lower section of the computation domain. At t = 0.0003 s (Fig. 81a), different from the holes at the top and bottom, the hole in the middle suffered the strongest air flow (from the top and bottom holes), and due to the weak wall adhesion effect on all the surfaces of the electrode, water became easier to be moved by the air stream. Therefore, the liquid water followed the air stream and flowed from the top and bottom into the hole in the middle. At t = 0.002 s (Fig. 81c), the movement of water became slower, this is because once the "strings" being formed, the air flowing into the top and bottom holes could also flow out from other top and bottom holes, thus decreasing the driving force of the liquid water in the middle, however, as mentioned, water was still flowing out.

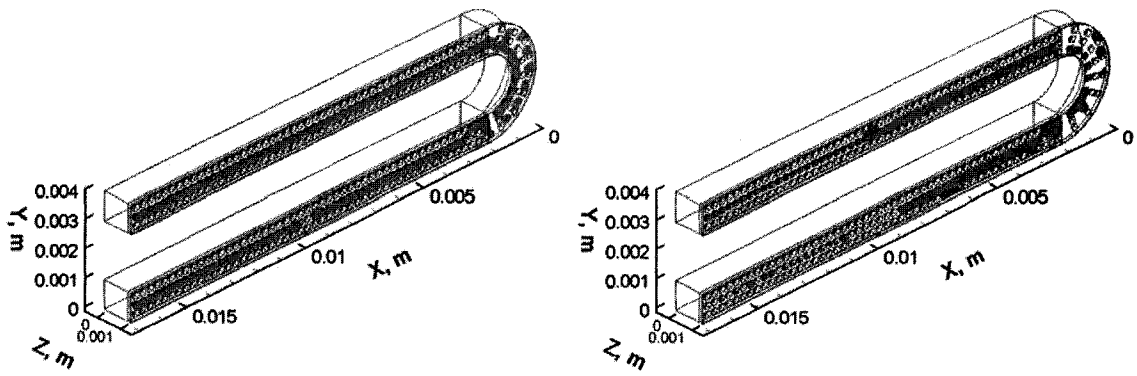

Fig. 80. Liquid water distribution in 3-D view for Case 3.

(a: t = 0.001 s; b: t = 0.02 s)

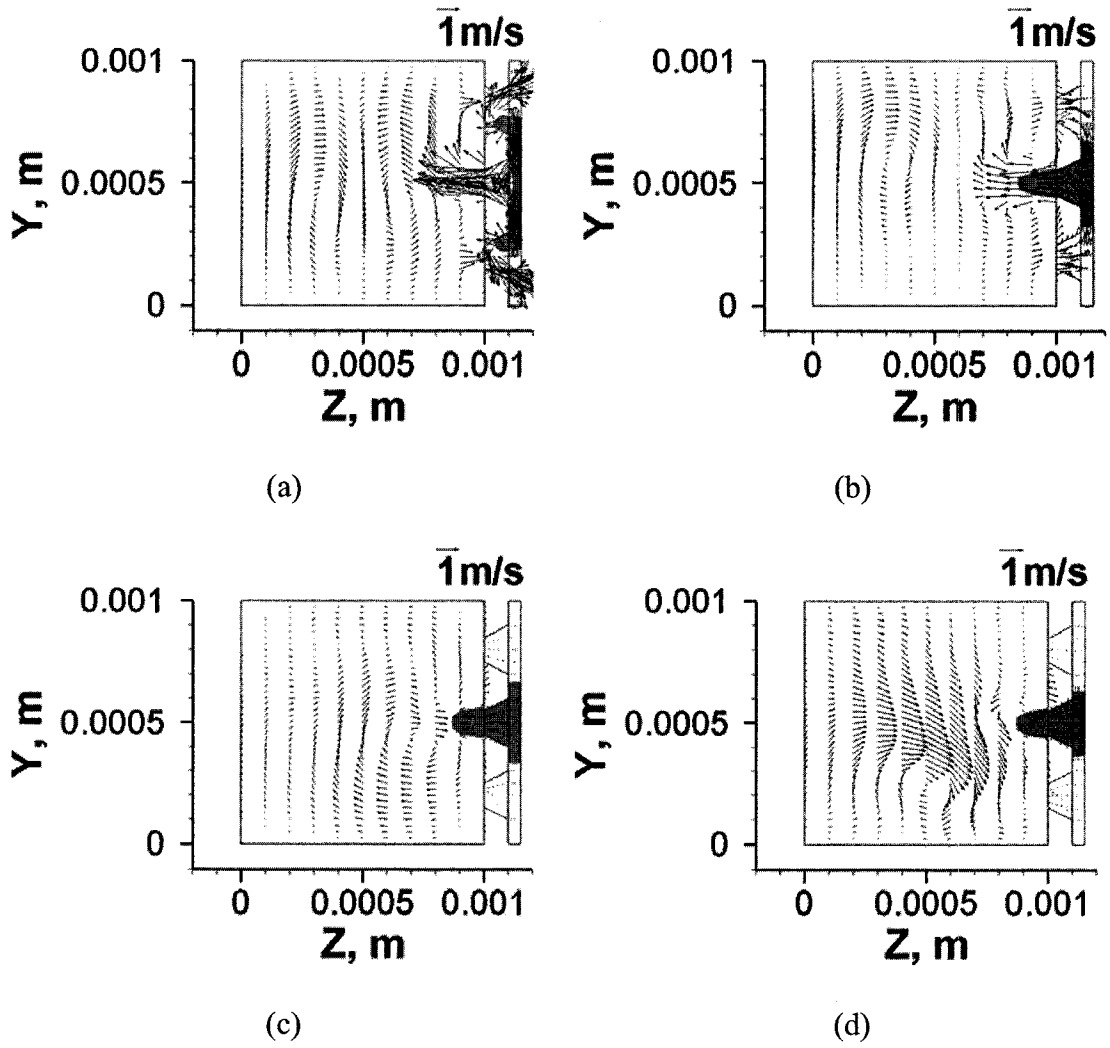

Fig. 81. Water distribution and velocity field on the plane at x = 0.00805 m in outlet section for Case 3.

(a: t = 0.0003 s; b: t = 0.0005 s; c: t = 0.002 s; d: t = 0.02 s)

7.3.2 "Struggle" between air and water

Fig. 82 shows the water distribution and velocity field on the center-plane of the lower section of the computation domain (y = 0.0005 m), the process of formation of the "string" could also be observed from this figure. At t = 0.0003 s (Fig. 82a), strong

streams flowing out of the holes could be observed, and later on, more water flowed onto this plane (as mentioned, from the top and bottom), at t = 0.0004 s (Fig. 82b), the whole electrode was filled with water and the water was still flowing into the gas flow channel. The stream became weaker at t = 0.0007 s (Fig. 82d), and at that time, more water could be observed in the gas flow channel. At t = 0.001 s (Fig. 82e), the streams flowing back into the electrode could be observed, and some water that previously moved into the gas flow channel then moved back into the electrode. As shown in Fig. 82f, at t = 0.002 s, less water could be observed in the gas flow channel, and the streams across the holes could be on longer apparently observed. The reason that some water flowed into the gas flow channel but then flowed back into the electrode is that, as mentioned, from the beginning the driving force to flow out the water was strong, however, after the "strings" were formed, the driving force was lost because the air stream could flow out from other holes, and part of the water that just flowed into the gas flow channel could be flowed back into the electrode due to the air stream in the gas flow channel.

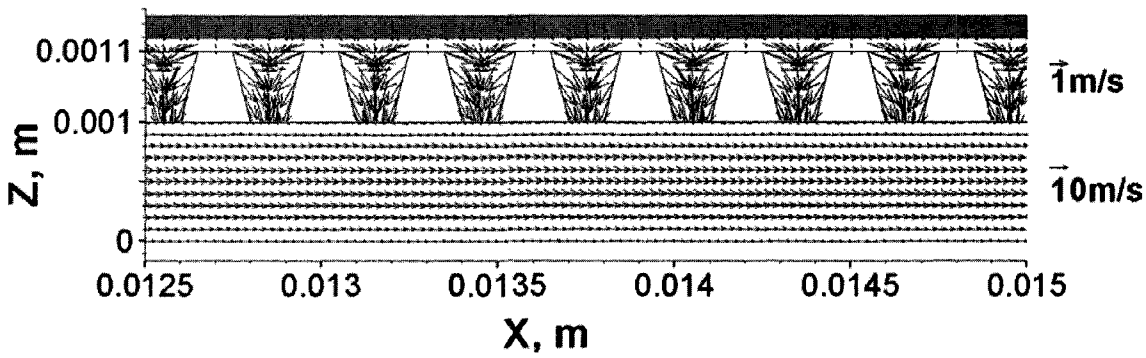

(a)

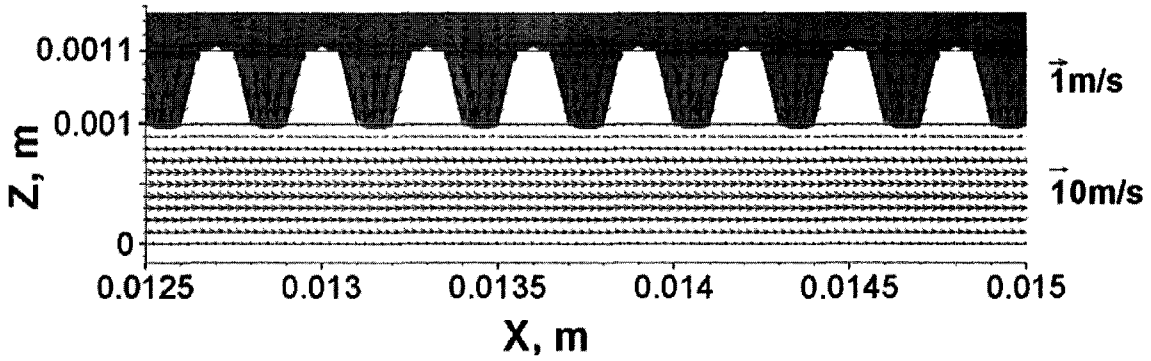

(b)

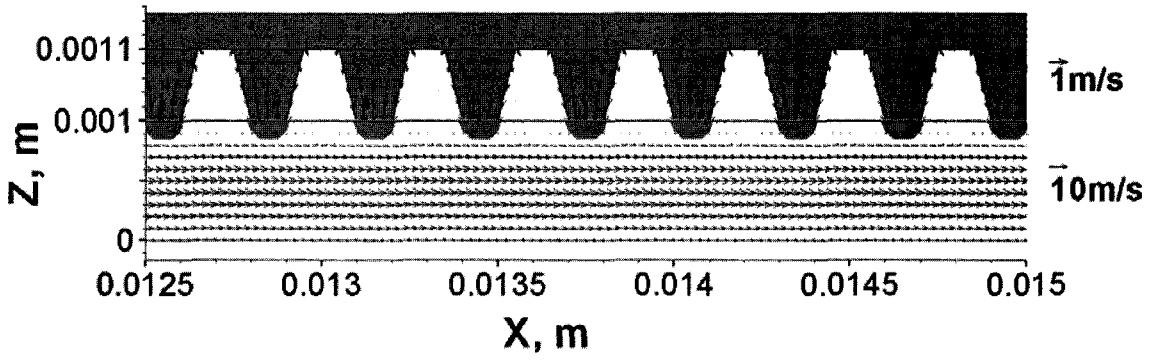

(c)

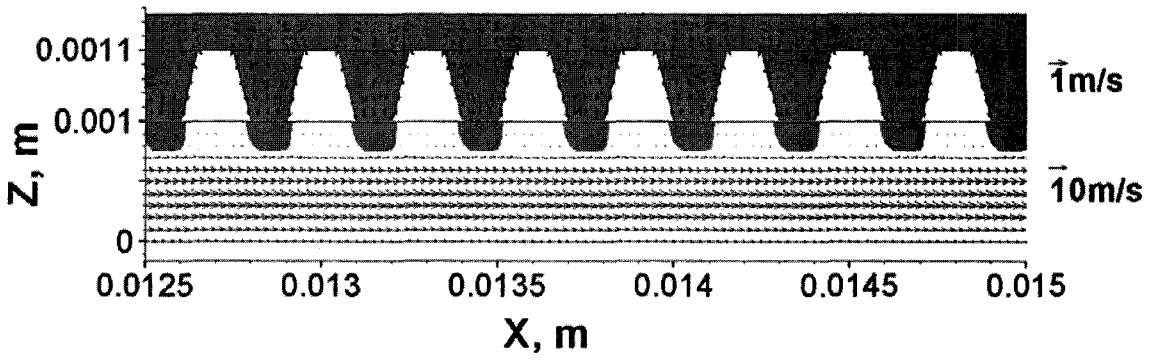

(d)

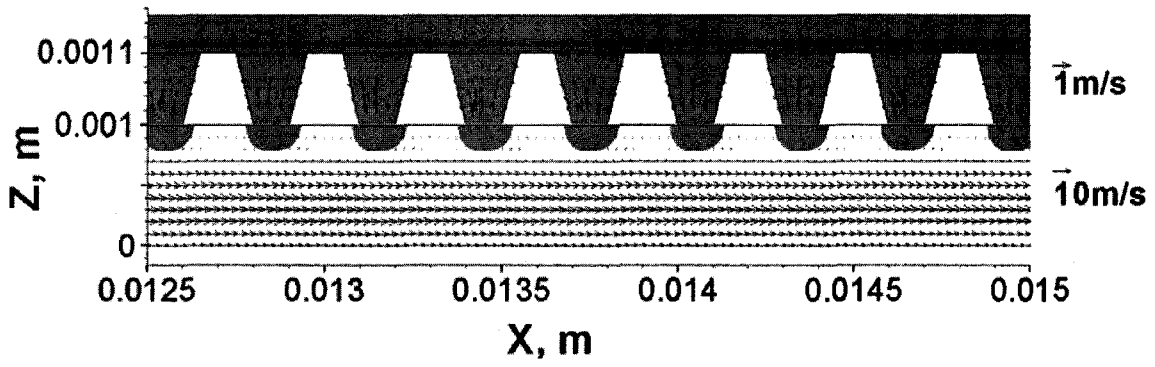

(e)

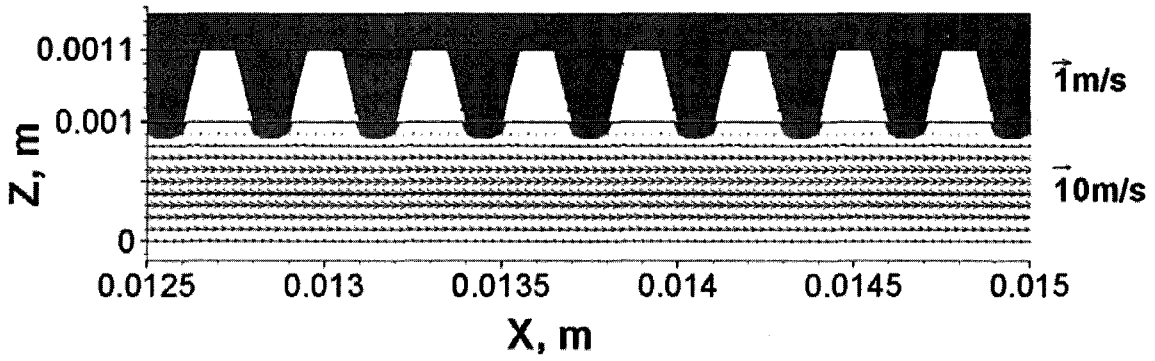

(f)

Fig. 82. Water distribution and velocity field on the center-plane (y = 0.0005 m) in outlet section for Case 3.

(×2 magnification along the z-direction for the electrode, ×3 minification along the z-direction for the flow channel) (a: t = 0.0003 s; b: t = 0.0004 s; c: t = 0.0005 s; d: t = 0.0007 s; e: t = 0.001 s; f: t = 0.002 s)

7.3.3 "Splashing" of liquid water in gas flow channel

Fig. 83 shows the water distribution and velocity field on the center-plane of the lower section of the computation domain (y = 0.0005 m) at a later time period. At t = 0.009 s, some water from the upstream could be observed, that part of water flowed along the air stream and splashed on to the holes at the downstream. Some water from the holes was

taken away by the liquid water "splashing" process. As shown in Fig. 83c (t = 0.012 s), as that part of water flowed away, significantly amount of water in the electrode was removed. Later on, another part of water from the upstream could be observed, and more water was taken away by it, as shown in Figs. 83d, 83e and 83f. As discussed in Case 1, dissimilar to this case, due to the hydrophilic property of the GDL, liquid water flowing from the upstream would always stick on the surface of the GDL and even flow back into the electrode. However, in this case, the wall adhesion effect became weaker due to the hydrophobic property of the whole electrode. Therefore, the liquid water on the GDL could be flowed away more easily, and the "splashing" of water could take some water away from the electrode, which is good for PEM fuel cell operation. Based on the flow behaviours that described in this section, it could be concluded that, if all the surfaces of the electrode are hydrophobic, the water removing ability could be significantly improved, thus improving the PEM fuel cell performance.

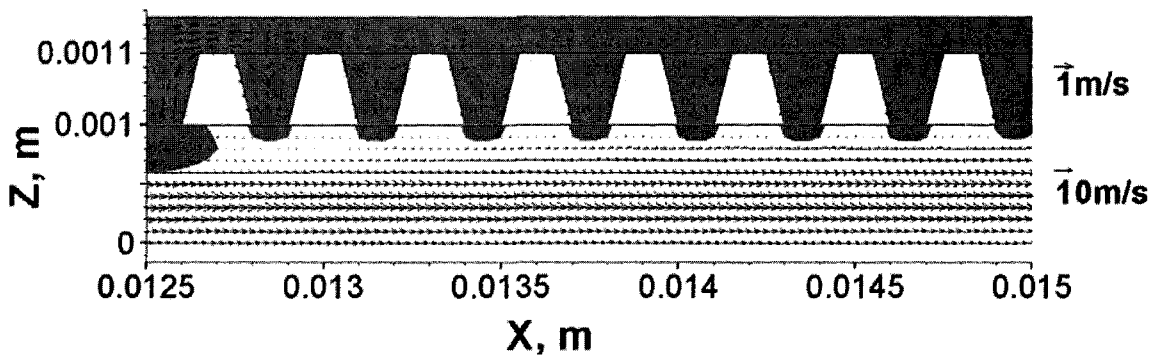

(a)

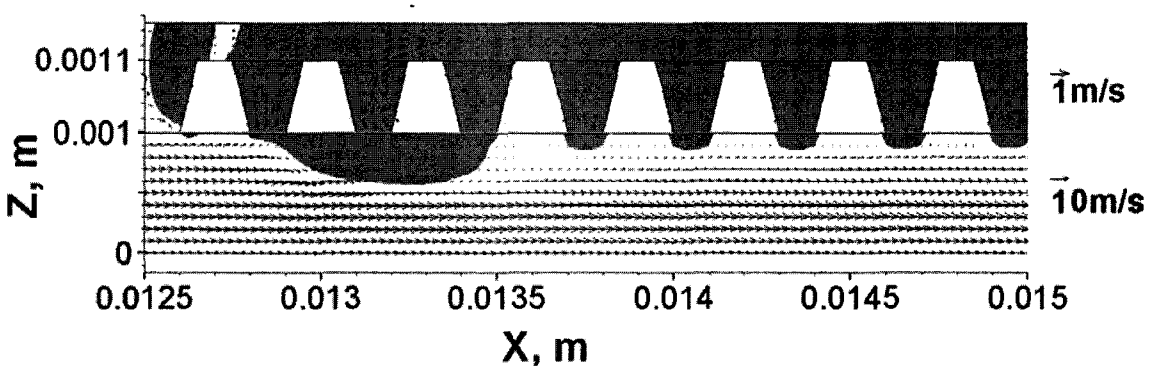

(b)

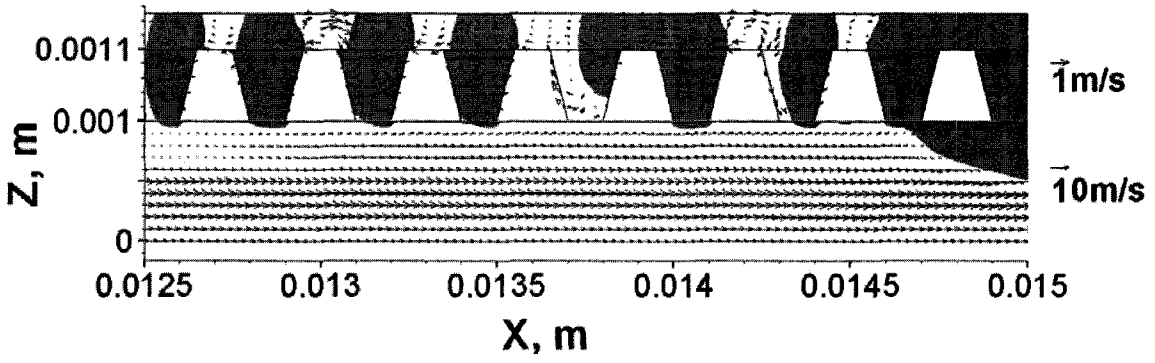

(c)

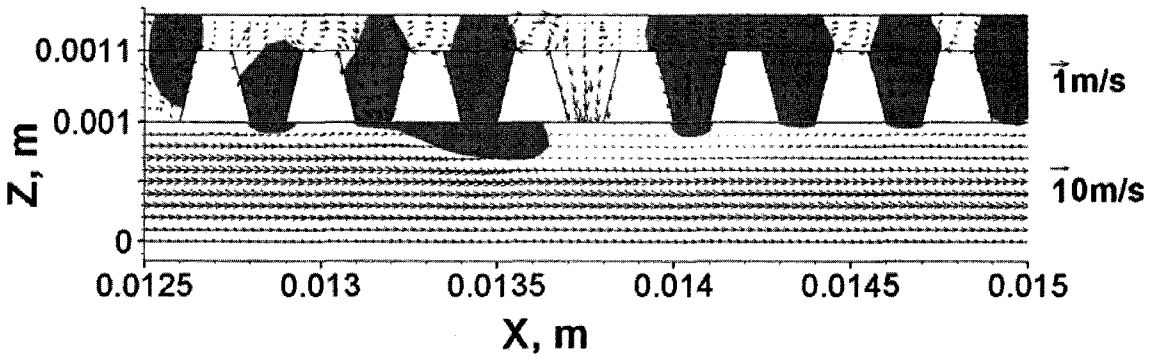

(d)

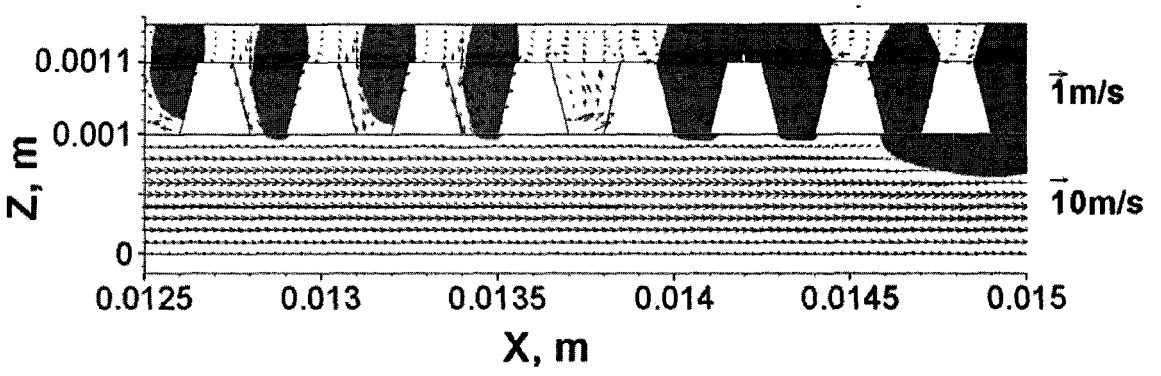

(e)

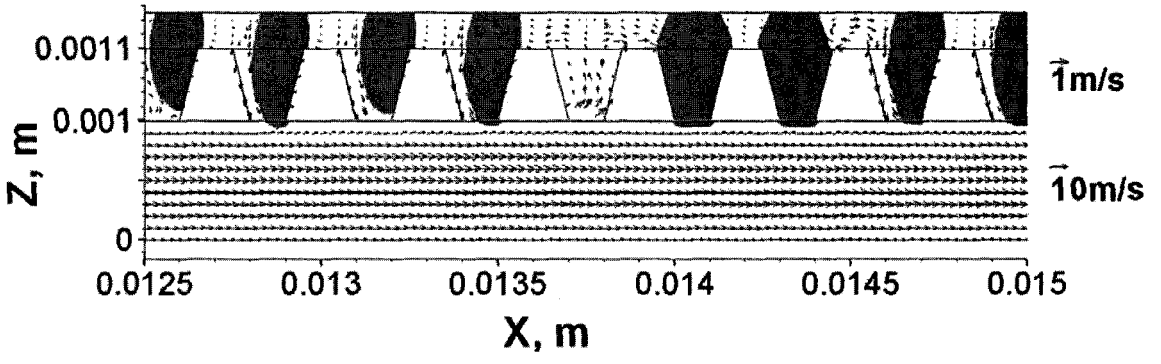

(f)

Fig. 83. Water distribution and velocity field on the center-plane (y = 0.0005 m) in outlet section for Case 3.

(×2 magnification along the z-direction for the electrode, ×3 minification along the z-direction for the flow channel) (a: t = 0.009 s; b: t = 0.01 s; c: t = 0.012 s; d: t = 0.013 s; e: t = 0.014 s; f: t = 0.015 s)

7.4 Comparison of water amount variations

Fig. 84 shows the comparison of water amount variations inside the electrode for the three cases. In Chapter 6, the same case with a contact angle of 90 degrees on all the surfaces was simulated, it showed that at t = 0.02 s, the water amount inside the electrode became 88%. For Case 1, surprisingly, a hydrophilic GDL even improved the water

removal ability (77% at t = 0.02s). This is because such GDL helped break up the water film into small pieces, and the small pieces of water could be more easily removed, such effect has overcome the strong wall adhesion on the GDL surfaces. For Case 2, a hydrophobic GDL did not provide any improvements on water removal (90% at t = 0.02 s), this is because such GDL provided more chances to form large pieces of water, therefore, the increased contact area between the walls and water increased the wall adhesion effect, and such effect has overcome the weak adhesion of the GDL surfaces. Case 3 showed significant advantage in water removal by comparing to the other two cases (54% at t = 0.02 s). The reason is that, the hydrophobic catalyst layer helped break up the liquid water film, and the hydrophobic GDL helped water flow out of the electrode. An increase of water amount could be observed following a sharp drop, the reason was discussed in section 3.3 – it was due the struggling process between the air and water. Fig. 85 shows the comparison of water amount variation inside the catalyst layer for the three cases. Case 3 still provided a much better result than the other two cases. However, Case 2 showed less water amount by comparing to Case 1, as mentioned in section 3.2, this is because the large pieces of liquid water in Case 2 occupied both the GDL and the electrode. Fig. 86 shows the comparison of water amount variation inside the GDL, without any surprise, Case 2 showed more water amount than Case 1. Base on the comparison of water amount variation of the three cases, it could be concluded that, if all the surfaces of the electrode are hydrophobic, water removal could be significantly improved, and only changing the wettability of the GDL might not provide any significant improvement on water removal. In order to improve the water removing ability of the electrode, the wettability of the GDL and the catalyst layer must be

carefully controlled, if the only GDL is hydrophobic, it could propel liquid water flowing to both sides (the gas flow channel and the catalyst layer). Therefore, the catalyst layer must have stronger or equal propelling effects on liquid water by comparing to the GDL (the static contact angle of the catalyst layer must be greater than or equal to the static contact angle of the GDL) to improve the water drainage.

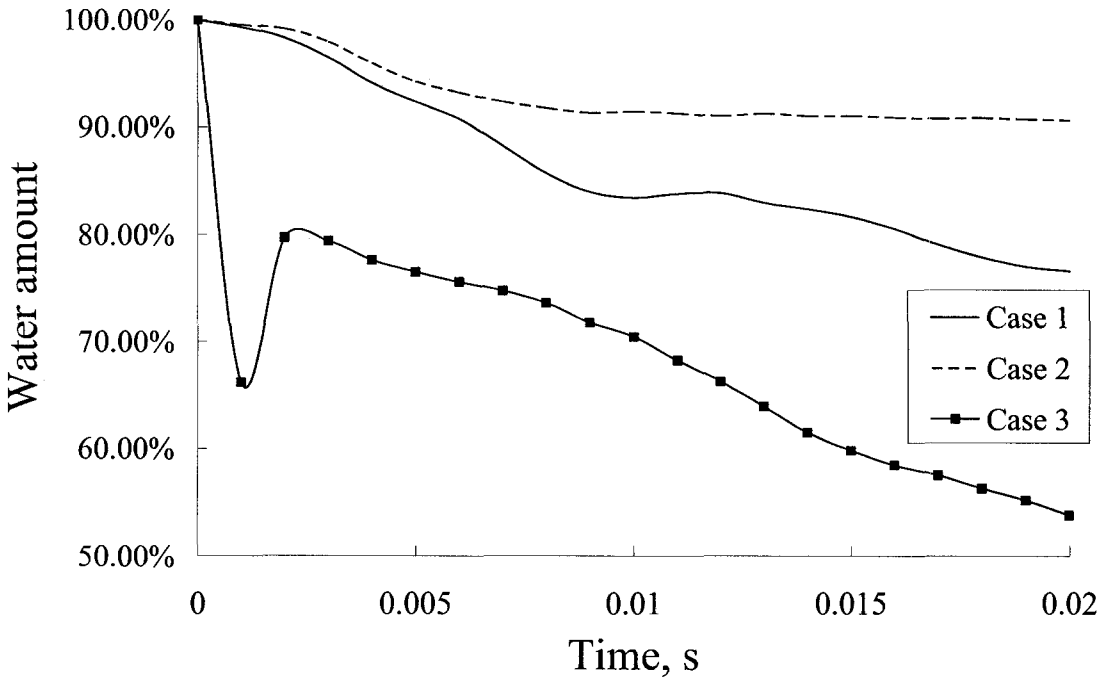

Fig. 84. Water amount variation inside the electrode for the three cases.

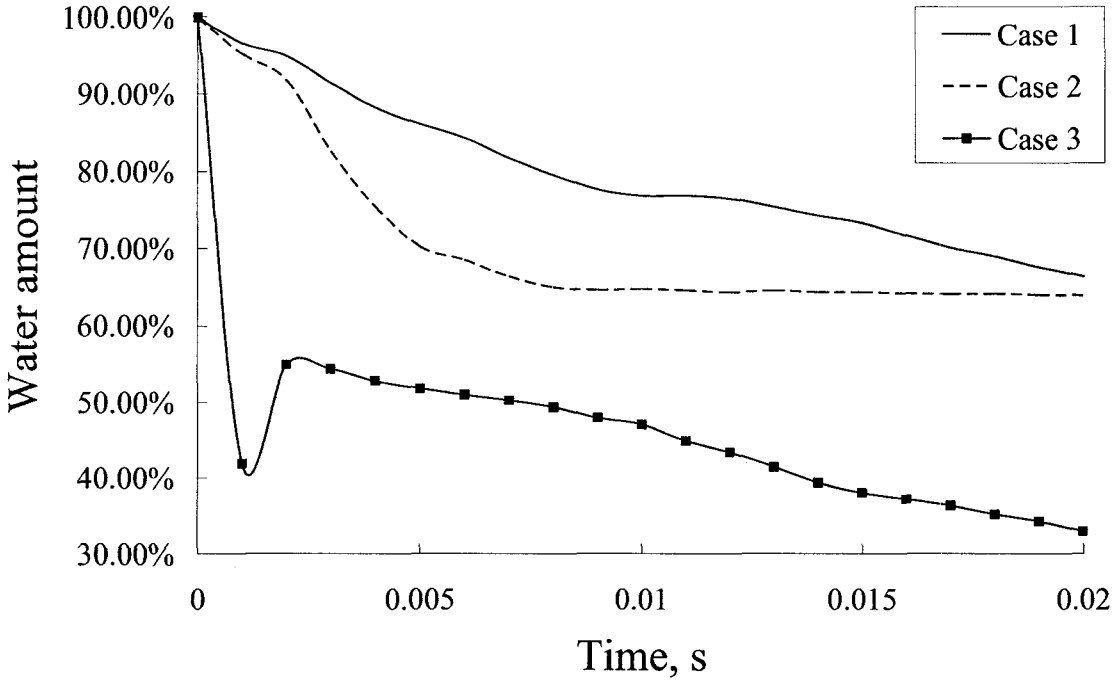

Fig. 85. Water amount variation inside the catalyst layer for the three cases.

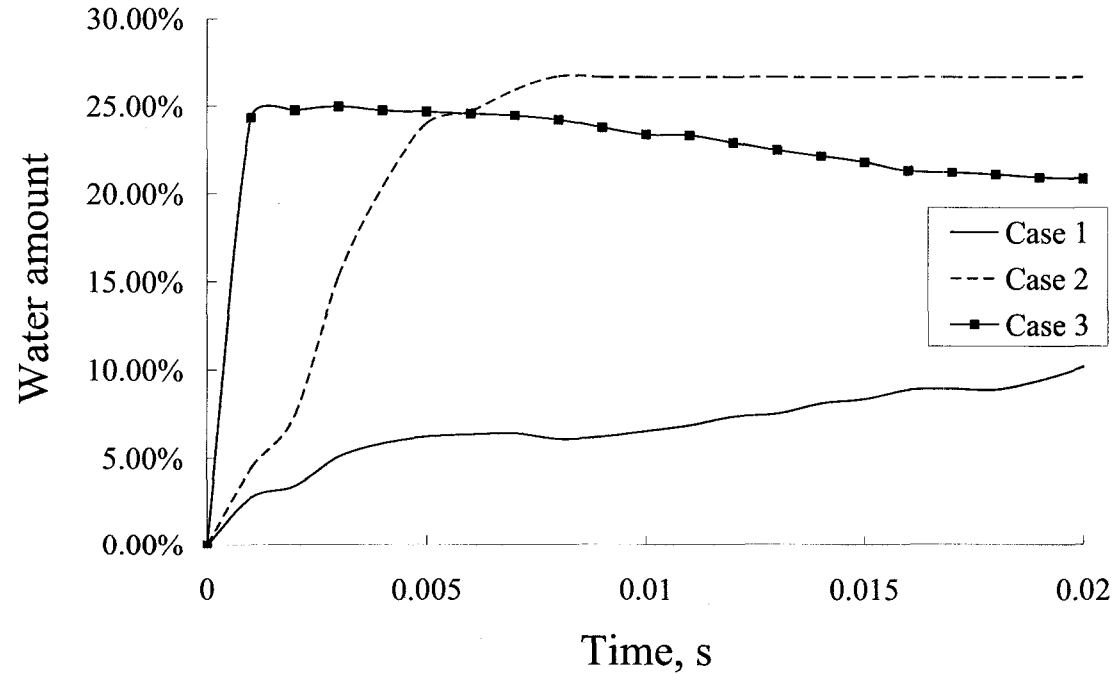

Fig. 86. Water amount variation inside the GDL for the three cases.

CHAPTER 8

CONCLUSIONS AND RECOMMENDATIONS

8.1 Conclusions

Overall the liquid water behaviours in PEM fuel cell cathode were successfully studied and the following objectives were met:

1. A literature review was performed, it was identified that numerical studies on liquid water behaviours in PEM fuel cell was rarely performed by researchers.
2. A numerical study on liquid water behaviours in both the PEM fuel cell stacks and GDLs were performed to address this important issue.
3. 3-D, two-phase, unsteady numerical models were conducted with different initial water distributions for this study.

By investigating the flow behaviours of liquid water and airflow velocity fields, the following water management issues have been identified:

1. If liquid water is supplied from the inlet, it is almost impossible to have evenly distributed water in each gas flow channel for parallel fuel cell stack. The gas flow channel that is closer to the air outlet always has a greater pressure drop and water is most likely to flow through this channel. But unevenly distributed water is not good for achieving a stable fuel cell performance.
2. Water in the outflow manifold could be blocked by air streams from the gas flow channels, with water continuously flowing into the outflow manifold, the outflow manifold may be blocked, the pressure in the outflow manifold and the outlets of the unit cells could become very high. Therefore, the pressure drop and flow rate along

these unit cells could decrease. In this kind of condition, the pressure drop and flow rate along other cells would become very high, the air flow would become unevenly distributed.

3. Pressure drop along all the unit cells could never increase or decrease at the same pace, once pressure drop along some unit cells increase, others' pressure drop would decrease.
4. If water hits the wall that faces the air inlet, water could be moved towards the air inlet again. In this case, water could not be moved into the gas flow channels on time, and the inlet manifold may become blocked with continuously supplied water.
5. Water could adhere to the end wall of both the inlet and outlet manifolds and it is difficult to remove this part of water.
6. Wall adhesion effects could slow down the water draining process, thus reducing the fuel cell performance.
7. For the straight sections of the serpentine PEM fuel cells, there is improved water drainage at the downstream of the corner than the upstream. This is mainly attributable to stronger secondary flow at the downstream of the corner.
8. The flow direction inside the catalyst layer is mainly dominated by the water distribution and not the main flow direction inside the gas flow channel.
9. The disruption of liquid water films would start from the initial ruptures and spread to other areas.
10. Residual water inside the catalyst layer is unavoidable. This is because the water stops moving when the balance between all the forces (surface tension, wall adhesion etc.) is achieved.

11. For the catalyst layer, the areas under the lands of the bipolar plate and the areas close to the surrounding walls are the most possible places that liquid water would stay; other areas suffer from strong air flow and are not surrounded by any walls thus are relatively harder to maintain liquid water.
12. Liquid water inside the catalyst layer will tend to reach a force balance by touching both the top and bottom surfaces. This is the most stable condition for liquid water because the force due to the wall adhesion effects is the maximum while the effect of the surface tension between air and liquid water is the minimum.
13. The more water removed from the catalyst layer, the more possibility that the GDL contains more water.
14. The general water transport features may not be significantly affected by the micro-structures of the GDL. However, the water removal characteristics and ability could be affected by different shapes of the holes of the GDL.
15. For the three innovative micro-structures investigated in Topic 3, the best water removal is achieved with the trapeziform porous holes with the minimum area facing the gas flow channel due to its ability to enhance the air flow inside the catalyst layer. The worst condition was when the air flow inside the catalyst layer became the weakest i.e. when the trapeziform porous holes with the minimum area facing the catalyst layer. Therefore, the key factor to design the GDL is trying to enhance the air flow inside the catalyst layer.
16. A well designed GDL can result in better water drainage than conventional GDL.
17. Hydrophilic GDL could retain liquid water between the holes of the GDL in the catalyst layer, thus forming liquid water "mesh". This is because such GDL could

provide more significant wall adhesion effect on liquid water, thus preventing liquid water flowing out, which is not good for PEM fuel cell operation.

18. Hydrophilic GDL could increase the chance for the liquid water flowing into the electrode, which is not good for PEM fuel cell operation.
19. Even a hydrophobic GDL could facilitate flowing away liquid water, but the direction is to both sides (the gas flow channel and the catalyst layer), the water drainage could be even worse
20. Hydrophobic catalyst layer could significantly increase the speed of water film rupture and water drainage, and liquid water "strings" could be formed in the catalyst layer.
21. If liquid water from the electrode moved too fast into the gas flow channel, some water may be flowed back into the electrode.
22. For hydrophobic GDL, liquid water inside the gas flow channel could take away some liquid water inside the GDL, and such "splashing" of liquid water is good for PEM fuel cell operation.
23. If all the surfaces of the electrode are hydrophobic, water removal could be significantly improved, and only changing the wettability of the GDL might not provide any significant improvement on water removal.

8.2 Recommendations

Some recommendations could be made to manage liquid water in an efficient way as follows:

1. Keeping a unit cell that may have the largest amount of water close to the outlet of

the outflow manifold is good for water drainage, thus the performance could become more stable.

2. Keeping the MEA side of the gas flow channels close to the outlet of the outflow manifold is recommended for having faster water drainage.
3. The serpentine gas flow channel's "collecting-and-separating-effect" could facilitate water drainage.
4. Keeping the maximum area of the holes of GDL facing the catalyst layer may result in better water drainage, thus the performance could become more stable. On the hand, the minimum area of the porous holes must be avoided to face the catalyst layer.
5. A good combination of serpentine flow channels and well designed GDLs may result in better water drainage.
6. It is critical to have both the GDL and catalyst to be hydrophobic for the best water drainage.

REFERENCES

[1] R. O'Hayre, S. Cha, W. Colella and F. Prinz, Fuel Cell Fundamentals, First Edition, John Wiley & Sons, 2006.

[2] J. Larminie and A. Dicks, Fuel Cell System Explained, Second Edition, John Wiley & Sons, 2003.

[3] J. S. Yi, J. D. Yang, C. King, AIChE J., 50 (2004) 2594.

[4] http://www.fuelcells.org.au/Fuel-Cell-Education-NSW-Australia.htm

[5] S. Um, C.Y. Wang and K.S. Chen, J. Electrochem. Soc., 147 (2000), 4485.

[6] S. Dutta, S. Shimpalee, J. W. Van Zee, J. Appl. Electrochem., 30 (2000) 135.

[7] E. Hontanon, M.J. Escudero, C. Bautista, P.L. Garcia-Ybarra, L. Daza, J. Power Sources, 86 (2000) 363.

[8] S. W. Cha, R. O'Hayre, Y. Saito, F. B. Prinz, J. Power Sources, 134 (2004) 57.

[9] A.A. Kulikovsky, Electrochem. Commun., 3 (2001) 460.

[10] Z.H. Wang, C.Y. Wang and K.S. Chen, J. Power Sources, 94 (2001), 40.

[11] L. You and H. Liu, Int. J. Heat and Mass Transfer, 45 (2002) 2277.

[12] U. Pasaogullari and C.Y. Wang, J. Electrochem. Soc., 152 (2005), A380.

[13] H. Meng and C.Y. Wang, J Electrochem. Soc., 152 (2005), A1733.

[14] Y. Wang and C.Y. Wang, J. Electrochem. Soc., 153 (2006), A1193.

[15] H. Meng and C.Y. Wang, Chemical Engineering Science, 59 (2004), 3331.

[16] H. Ju and C.Y. Wang, J. Electrochem. Soc., 151 (2004), A1954.

[17] H. Ju, C.Y. Wang, S. Cleghorn and U. Beuscher, J. Electrochem. Soc., 153 (2006), A249.

[18] Y. Wang and C.Y. Wang, J. Power Sources, 153 (2006), 130.

[19] C.Y. Wang, Chemical Reviews, 104 (2004), 4727.

[20] X.G. Yang, F.Y. Zhang, A. Lubawy and C.Y. Wang, Electrochem. & Solid-State Lett., 7 (2004), A408.

[21] F.Y. Zhang, X.G. Yang and C.Y. Wang, J Electrochem. Soc., 153 (2006), A225.

[22] J. H. Nam and M. Kaviany, Int. J. Heat and Mass Transfer, 46 (2003), 4595.

[23] H. Dohle, R. Jung, N. Kimiaie, J. Mergel and M. Muller, J. Power Sources, 124 (2003), 371.

[24] U. Pasaogullari and C. Wang, Electrochem. Acta., 49 (2004), 4359.

[25] S. Freni, G. Maggio and E. Passalacqua, Materials Chemistry and Physics, 48 (1997), 199.

[26] P. Quan, B. Zhou, A. Sobiesiak and Z. Liu, J. Power Sources, 152 (2006) 131.

[27] K. Jiao, B. Zhou and P. Quan, J. Power Sources, 154 (2006) 124.

[28] K. Jiao, B. Zhou and P. Quan, J. Power Sources, 157 (2006) 226.

[29] K. Jiao and B. Zhou, J. Power Sources, 169 (2007), 296.

[30] Fluent 6.2 User's Guide, Fluent Inc., 2005.

[31] B. R. Munson, D. F. Young and T. H. Okiishi, Fundamentals of Fluid Mechanics, Forth Edition, John Wiley & Sons, New York, 2002.

VITA AUCTORIS

Kui Jiao grew up in Shangqiu, Henan, China. He came to Canada alone in September 2000 when he was 16 years old. He finished all the English courses and six OAC courses within one year. From there he went on to study at the University of Windsor where he attained a B.A,Sc. in Mechanical Engineering in 2005. He is currently a candidate for the Master's degree in Mechanical Engineering at the University of Windsor and hopes to graduate in 2007.